remote sensing

Review

Spatial Validation of Spectral Unmixing Results: A Systematic Review

Rosa Maria Cavalli

Research Institute for Geo-Hydrological Protection (IRPI), National Research Council (CNR), 06128 Perugia, Italy; rosa.maria.cavalli@irpi.cnr.it; Tel.: +39-075-501-422

Abstract: The pixels of remote images often contain more than one distinct material (mixed pixels), and so their spectra are characterized by a mixture of spectral signals. Since 1971, a shared effort has enabled the development of techniques for retrieving information from mixed pixels. The most analyzed, implemented, and employed procedure is spectral unmixing. Among the extensive literature on the spectral unmixing, nineteen reviews were identified, and each highlighted the many shortcomings of spatial validation. Although an overview of the approaches used to spatially validate could be very helpful in overcoming its shortcomings, a review of them was never provided. Therefore, this systematic review provides an updated overview of the approaches used, analyzing the papers that were published in 2022, 2021, and 2020, and a dated overview, analyzing the papers that were published not only in 2011 and 2010, but also in 1996 and 1995. The key criterion is that the results of the spectral unmixing were spatially validated. The Web of Science and Scopus databases were searched, using all the names that were assigned to spectral unmixing as keywords. A total of 454 eligible papers were included in this systematic review. Their analysis revealed that six key issues in spatial validation were considered and differently addressed: the number of validated endmembers; sample sizes and sampling designs of the reference data; sources of the reference data; the creation of reference fractional abundance maps; the validation of the reference data with other reference data; the minimization and evaluation of the errors in co-localization and spatial resampling. Since addressing these key issues enabled the authors to overcome some of the shortcomings of spatial validation, it is recommended that all these key issues be addressed together. However, few authors addressed all the key issues together, and many authors did not specify the spatial validation approach used or did not adequately explain the methods employed.

Keywords: mixed pixels; spectral unmixing; spatial validation; accuracy

check for updates

Citation: Cavalli, R.M. Spatial Validation of Spectral Unmixing Results: A Systematic Review. *Remote Sens.* **2023**, *15*, 2822. https://doi.org/10.3390/rs15112822

Academic Editors: Jorge Delgado García, Fayez Tarsha Kurdi and Tarig Ali

Received: 30 March 2023
Revised: 22 May 2023
Accepted: 24 May 2023
Published: 29 May 2023

1. Introduction

1.1. Background

A pixel that contains more than one "land-cover type" is defined as a mixed pixel, and its spectrum is formed by combining the spectral signatures of these "land-cover types" [1]. The presence of mixed pixels in the image constrains the techniques that can be carried out to analyze, characterize, and classify the remote sensing images [2,3]. To retrieve mixed-pixel information from remote sensing images, a shared research effort allowed developing several methods (e.g., spectral unmixing, probabilistic, geometric-optical, stochastic geometric, and fuzzy models [1]). However, the literature shows that, for over 40 years, spectral unmixing has been the most commonly used method for discrimination, detection, and classification of superficial materials [4–6].

The spectral unmixing was defined as the "procedure by which the measured spectrum of a mixed pixel is decomposed into a collection of constituent spectra, or endmembers, and a set of corresponding fractions, or abundances, that indicate the proportion of each endmember present in the pixel" [6]. It is important to point out that many names were given to the spectral unmixing procedure: hyperspectral unmixing [7,8], linear mixing [9], nonlinear spectral mixing models [10,11], semi-empirical mixing model [12], spectral mixing models [13–15], spectral mixture analysis [16–22], spectral mixture modeling [23,24], and spectral unmixing [19,25,26]. In this paper, the term spectral unmixing was chosen.

The first studies that introduced the spectral unmixing procedure were carried out about 40 years ago (Table 1). In order to study Moon minerals, Adams & McCord [27] observed nonlinear behavior of the spectra of Apollo 11 and 12 samples that were measured in the laboratory. In order to analyze the spectra of Mars, Singer & McCord [28] assumed that the spectrum of the mixed pixel was a bilinear combination of the spectra of its two constituent materials, and it was weighted by their abundances in the mixed pixel; their model required two constraints: the sum of the weighing factors must be one, and their values must not be negative. Hapke [29] proposed a nonlinear mixing model that was called "isotropic multiple scattering approximation" by Heylen et al. [8]. Johnson et al. [12] and Smith et al. [13] combined "spectral mixing model" with the modified Kubelka–Munk model and principal component analysis, respectively. In order to analyze the spectra of Mars, Adams & Smith [23] improved the "bilinear model", which was proposed by Singer & McCord [28], considering more than two constituent materials of the mixed pixel and adding the residual error.

Table 1. Studies that introduced spectral unmixing procedure.

Paper	Publication Year	Study Area	Spectral Range	Name Given to Spectral Unmixing Procedure	Citations in Google Scholar
Adams & McCord [27]	1971	Lunar	0.35–2.5 µm	-	136
Singer & McCord [28]	1979	Mars	0.35–2.5 µm	-	347
Hapke [29]	1981	Planets		-	2200
Johnson et al. [12]	1983	Minerals	0.35–2.5 µm	Semi-empirical mixing model	288
Smith et al. [13]	1985	Minerals	0.60–2.20 µm	Spectral mixing model	454
Adams et al. [23]	1986	Mars	0.35–2.5 µm	Spectral mixture modeling	1634
Adams et al. [16]	1989	-	1.2–2.4 µm	Spectral mixture analysis	131

Adams et al. [16] decomposed the "spectral mixture analysis" in two consecutive steps: the first step decomposes the spectrum of each mixed pixel into a collection of constituent spectra (called endmembers), and the second step determines the proportion of every endmember present in the pixel. The literature highlighted two main models for performing the first step: linear and nonlinear mixture models. To estimate the proportion of every endmember (called fractional abundances), many solutions were proposed (e.g., Gram–Schmidt Orthogonalization [30], Least Square Methods [31], Minimum Variance Methods [6], Singular Value Decomposition [32], Variable Endmember Methods [6]).

1.2. Reviews on the Spectral Unmixing Procedure

In order to more effectively understand the importance of spectral unmixing, a quantification of the works that have studied, implemented, and applied this procedure since 1971 were provided. For this purpose, all names that were given to the spectral unmixing procedure were exploited as terms in the search strategy. A total of 5768 and 5852 papers were identified using Web of Science and Scopus search engines, respectively (accessed on 19 May 2023). Among these papers, 19 reviews offered the status of spectral unmixing (Table 2).

An interesting overview of the "linear models" developed up to 1996 was offered by Ichoku & Karneili [1], who compared this method with four other unmixing models: probabilistic, geometric-optical, stochastic geometric, and fuzzy models. The authors summarized that evaluated spatial accuracies were not representative of the real accuracies at the level of individual pixels because the spatial validation was performed for a few test pixels.

Table 2. Reviews on the spectral unmixing procedure.

Paper	Publication Year	Publication Title	Number of References Cited in the Review	Citations in Google Scholar [1]
Ichoku & Karneili [1]	1996	A review of mixture modelling techniques for subpixel land cover estimation	57	281
Heinz & Chein-I-Chang [33]	2001	Fully Constrained Least Squares Linear Spectral Mixture Analysis Method for Material Quantification in Hyperspectral Imagery	39	1955
Keshava & Mustard [6]	2002	Spectral unmixing	40	2761
Keshava [34]	2003	A Survey of Spectral Unmixing Algorithms	3	641
Martinez et al. [35]	2006	Endmember extraction algorithms from hyperspectral images	16	67
Veganzones & Grana [36]	2008	Endmember Extraction Methods: A Short Review	23	82
Bioucas-Dias & Plaza [7]	2010	Hyperspectral unmixing: Geometrical, statistical, and sparse regression-based approaches	97	77
Parente & Plaza [37]	2010	Survey of geometric and statistical unmixing algorithms for hyperspectral images	53	124
Bioucas-Dias & Plaza [38]	2011	An overview on hyperspectral unmixing: geometrical, statistical, and sparse regression based approaches	51	78
Somer et al. [39]	2011	Endmember variability in Spectral Mixture Analysis: A review	179	660
Bioucas-Dias et al. [40]	2012	Hyperspectral Unmixing Overview: Geometrical, Statistical, and Sparse Regression-Based Approaches	96	2597
Quintano et al. [41]	2012	Spectral unmixing: a review	163	141
Ismail & Bchir [42]	2014	Survey on Number of Endmembers Estimation Techniques for Hyperspectral Data Unmixing	22	1
Heylen et al. [8]	2014	A Review of Nonlinear Hyperspectral Unmixing Methods	201	452
Shi & Wang [43]	2014	Incorporating spatial information in spectral unmixing: A review	106	197
Drumetz et al. [44]	2016	Variability of the endmembers in spectral unmixing: recent advances	26	34
Wang et al. [45]	2016	A survey of methods incorporating spatial information in image classification and spectral unmixing	280	75
Wei & Wang [5]	2020	An Overview on Linear Unmixing of Hyperspectral Data	74	17
Borsoi et al. [4]	2021	Spectral Variability in Hyperspectral Data Unmixing	317	63

[1] Accessed on 31 January 2023.

Heinz & Chein-I-Chang [33] focused on the second constraint of linear spectral mixture analysis (i.e., the fractional abundances of each mixed pixel must be positive), which is very difficult to implement in practice. Reviewing the literature, the authors pointed out that because most research did not know in detail the spectra present in the image scene, their results did not necessarily reflect the true abundance fractions of the materials [33].

Keshava [42] exploited the hierarchical taxonomies to facilitate comparison of the wide variety of methods used for spectral unmixing and revealed their similarities and differences. Furthermore, the author restated that most of the methods developed to solve problems were due to lack of detailed knowledge of ground truth. In their extensive description of spectral unmixing methodology, Keshava and Mustard [6] focused on the processing chain of linear unmixing methods applied to hyperspectral data. The authors highlighted that the shortcomings in spatial validation were due to the lack of detailed ground-truth knowledge; for this reason, the main focus of the research was on determining endmembers, rather than recovering fractional abundance maps [6].

Bioucas-Dias et al. [36] aimed to update the previous review, which was proposed by Keshava and Mustard [6] 10 years earlier. Therefore, the authors extensively described the methods that were proposed from 2002 to 2012 to improve the mathematical validity of the spectral unmixing. Bioucas-Dias & Plaza [7,38], Parente & Palza [37], Veganzones & Grana [40], and Martinez et al. [41] provided brief, but comprehensive reviews of methods for statistical and geometric extraction of endmembers. Somers et al. [39] provided a comprehensive and extensive review of the methods to address the temporal and spatial variability of the endmembers in the spectral unmixing.

An introduction to nonlinear unmixing methods and an overview of the most commonly used approaches were provided by Heylen et al. [8]. These authors also pointed out the lack of detailed ground truths for accurate validation of the spectral unmixing procedures [8]. After performing a general review of spectral unmixing, Quintano et al. [41] provided an interesting summary of its applications. Moreover, the authors pointed out the difficulty in spatially validating the results of spectral unmixing results and identified two main reasons: "(1) it is difficult to collect ground truth as scale directly corresponding to remotely sensed data resolution; (2) traditional classification accuracy analysis measurement tools may not be suitable for mixed pixel analysis" [41].

Wei & Wang [5] presented an overview of four aspects of the spectral unmixing (i.e., geometric method, nonnegative matrix factorization (NMF), Bayesian method, and sparse unmixing), whereas an overview of the methods that estimated the number of endmembers was provided by Ismail & Bchir [39]. Shi & Wang [43] provided a comprehensive review of the methods that combined spatial and spectral information for the spectral unmixing; the authors called them "spatial spectral unmixing" [43]. To extract endmembers, select endmember combinations, and estimate endmember fraction abundances, these methods exploited the correlation between neighboring pixels [43]. Wang et al. [45] provided an overview of the methods that incorporated the spatial information not only in spectral unmixing, but also in the all image classifiers. The authors underlined that most of the spatial accuracy was based on "the idea of area-weighted accuracy" because it was derived from some validation samples.

The most recent review was offered by Borsoi et al. [4], who provided a comprehensive review of the methods to solve the spectral variability problem in hyperspectral data. The spectral variability is mainly due to atmospheric, illumination, and environmental conditions [46,47]. Starting from the availability or non-availability of spectral libraries, the authors organized the "Spectral Unmixing algorithms" "according to a practitioner's point of view, based on the necessary amount of supervision and the computational cost" and highlighted that the algorithms with less supervision (i.e., Fuzzy Unmixing, MESMA—Multiple Endmember Spectral Mixture Analysis—and variants, Bayesian models) are the methods with high computational cost [4]. Moreover, the authors pointed out the difficulty of assessing the accuracy of these methods due to the lack of detailed ground truths [4]. A review of four of these methods, which address the spectral variability problem, was also provided by Drumetz et al. [44].

It is important to mention that the spatial accuracy of spectral unmixing results can be evaluated using images and/or in situ data and/or maps, and the spectral accuracy of spectral unmixing results can be evaluated using spectral signatures that were acquired in situ and/or in the laboratory and/or obtained from images [4,6,8,33,45]. However, an independent validation dataset is required (i.e., the spectral library and/or the reference maps) [48].

1.3. Objectvives

In conclusion, since 1971 many methods have been introduced to improve the mathematical validity of the spectral unmixing procedure, but the validation of the results still needs much improvement, especially the spatial validation. In particular, the lack of detailed ground-truth knowledge is the main reason of the many shortcomings in the spatial validation of the spectral unmixing results. However, no author provided an overview focusing on the spatial validation of the spectral unmixing results.

Therefore, this systematic review aims to provide readers with (a) an overview of how the previous authors approached spatial validation of spectral unmixing results and (b) recommendations for overcoming the many shortcomings of spatial validation and minimizing its errors. The systematic review was carried out in accordance with the Preferred Reporting Items for Systematic reviews and Meta-Analysis (PRISMA) statement [49,50]. The methodological approach employed in this systematic literature review is explained in Section 2, whereas the results, discussion, and conclusions are presented in Sections 3 and 4.

2. Materials and Methods

2.1. Identification Criteria

This systematic literature review aims to provide readers with an overview of the approaches applied for spatial validation of spectral unmixing results and does not claim to be exhaustive since too many works have studied, implemented, and applied this technique since 1971. Therefore, the papers published in 2022, 2021, and 2020 were chosen to analyze the current status, whereas those published not only in 2011 and 2010, but also in 1996 and 1995 were selected to assess the progress over time. The year 1995 was chosen as the initial time for the systematic review, because in this year, spectral unmixing and other "mixture modeling techniques" were well implemented and, thus, commonly employed [1,6,51–54]. The Web of Science (WoS) and Scopus search engines were used to identify the papers that spatially validated the spectral unmixing results and were published in 2022, 2021, 2020, 2011, 2010, 1996, and 1995.

Initially, the papers that named the spectral unmixing in the titles, abstracts, and keywords were identified. For this purpose, all the names assigned to spectral unmixing (i.e., hyperspectral unmixing, linear mixing, nonlinear spectral mixing models, semi-empirical mixing model, spectral mixing models, spectral mixture analysis, spectral mixture modeling, spectral unmixing) were employed as unique query strings (first yellow box in Figure 1).

The total records identified from these databases was 2999. The subject areas of the search engines were checked to refine the identification of the papers. Therefore, "4.169 Remote Sensing", "4.174 Digital Signal Processing", "4.17 Computer Vision & Graphics", "5.250 Imaging &Tomography", "5.20 Astronomy & Astrophysics", "5.191 Space Sciences", "8.8 Geochemistry, Geophysics & Geology", "8.93 Archaelogy", "8.19 Oceanography, Meteorology & Atmospheric", "8.140 Water Resources", "8.124 Environmental Sciences", "3.40 Forestry", and "3.45 Soil Science" were "Citation Topics" selected in the WoS database, whereas "Earth and Planetary Sciences", "Physics and Astronomy", and "Environmental Science" were the subject areas selected in the Scopus database. After refining the subject areas, the identified papers became 2034 (second yellow box in Figure 1): 1396 were the papers published in 2022, 2021, and 2020; 538 were the papers published in 2011 and 2010; 100 were the papers published in 1996 and 1995.

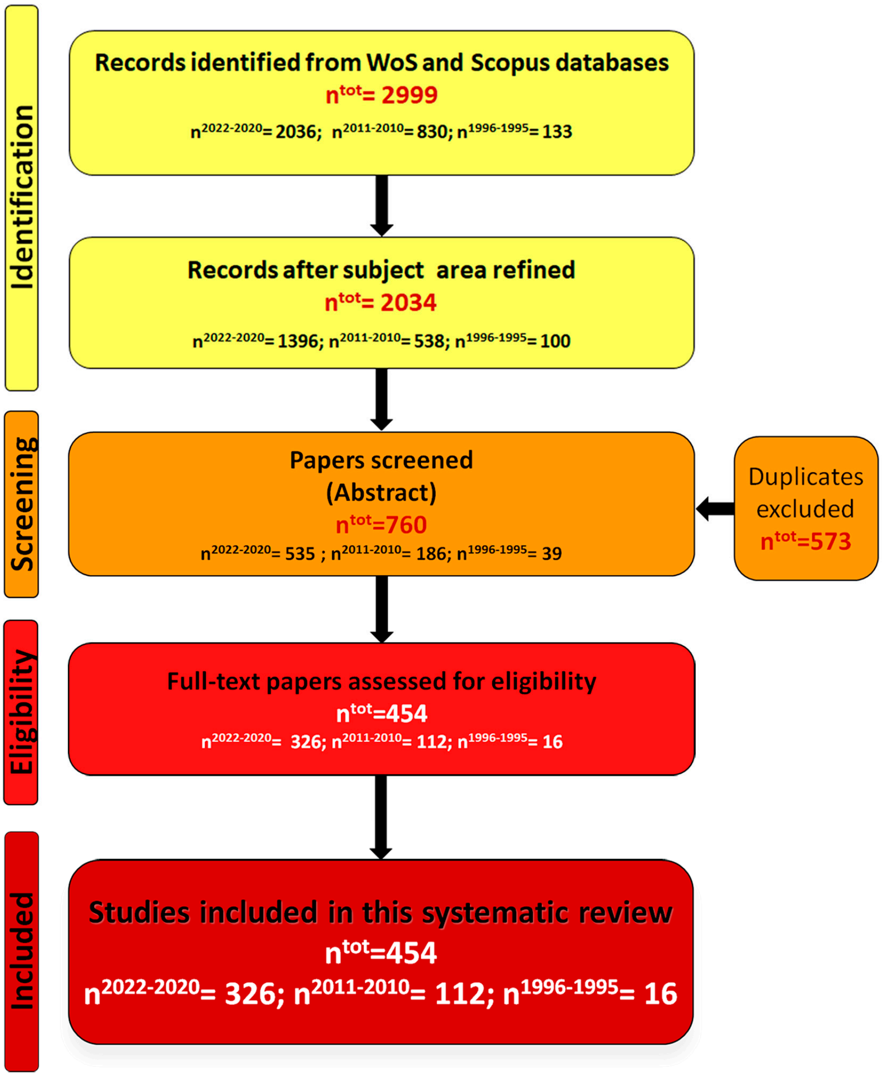

Figure 1. PRISMA flow chart showing the different steps of the dataset creation, where n^{tot} was the total number of papers; $n^{2022–2020}$ was the number of papers that were published in 2022, 2021, and 2020; $n^{2011–2010}$ was the number of papers that were published in 2011 and 2010; $n^{1996–1995}$ was the number of papers that were published in 1996 and 1995.

2.2. Screening and Eligible Criteria

Reading the abstracts of the identified papers was conducted to select only those that applied spectral unmixing to remote images. Excluding the duplicates, 760 papers were selected with the first screening (orange box in Figure 1): 535 were the papers published in 2022, 2021, and 2020; 186 were the papers published in 2011 and 2010; 100 were the papers published in 1996 and 1995.

Reading the full text of the screened papers was conducted to identify only those that spatially validated the spectral unmixing results (bright red box in Figure 1). The last analysis identified the eligible papers: 326 were the papers published in 2022, 2021, and 2020; 112 were the papers published in 2011 and 2010; 16 were the papers published in 1996 and 1995.

In conclusion, 454 eligible papers were included in this systematic review. In Appendix A, the Tables A1–A7 summarize the characteristics of the eligible papers that were published in 2022, 2021, 2020, 2011, 2010, 1996, and 1995, respectively.

3. Results

3.1. Spatial Validation of Spectral Unmixing Results

The screening carried out showed that the number of studies that spatially validated the results of spectral unmixing has significantly increased over the selected years (bright red box in Figure 1): about 100 research papers per year were published in the past 3 years; about 50 research papers per year were published in 2011 and 2010; about 10 research papers per year were published in 1996 and 1995. The screening carried out showed also that the number of studies that applied spectral unmixing has significantly increased over the selected years (orange box in Figure 1): about 180 research papers per year were published in the past 3 years; about 90 research papers per year were published in 2011 and 2010; about 20 research papers per year were published in 1996 and 1995. In order to assess the importance of spatial validation in the spectral unmixing procedure, the papers that applied spectral unmixing to remote imaging were analyzed (orange box in Figure 1). Figure 2 shows the percentage of these papers that were not validated (the percentage in grey wedges), spectrally validated (the percentage in yellow wedges), spatially validated (the percentage in blue wedges), and spatially and spectrally validated (the percentage in green wedges) the spectral unmixing results. Therefore, spatial validation was carried out alone (blue wedges in Figure 2) or together with spectral validation (green wedges in Figure 2).

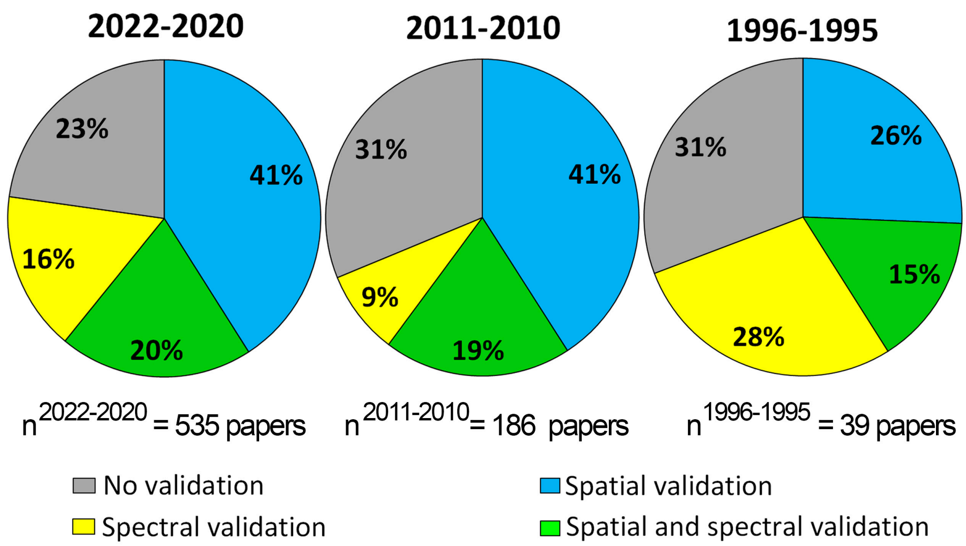

Figure 2. Distribution of the papers that applied the spectral unmixing to remote images (orange box in the Figure 1) according to different ways in which their results were validated, where $n^{2022–2020}$ was the number of papers that were published in 2022, 2021, and 2020; $n^{2011–2010}$ was the number of papers that were published in 2011 and 2010; $n^{1996–1995}$ was the number of papers that were published in 1996 and 1995.

Considering all papers that performed spatial validation (blue and green wedges in Figure 2), the percentage of these research published in 2022, 2021, and 2020 (61% of a total of 326 papers) was comparable to that of the papers that were published in 2011 and 2010 (60% of a total of 112 papers), whereas these percentages were greater than those of the papers that were published in 1996 and 1995 (41% of a total of 16 papers). Moreover, the percentage of the research published in 2022, 2021, and 2020 that did not validate the results (23%) was smaller than those of the papers that were published in the other 2 groups of years (31%). In conclusion, these values highlighted not only the increasing application of spectral unmixing over these years, but also the high priority given to the spatial validation.

3.2. Remote Images

The eligible papers published in 2022, 2021, 2020, 2011, 2010, 1996, and 1995 are summarized in Tables 3–9, according to the remote images to which spectral unmixing was applied. Authors who applied only spatial validation were cited in the fourth columns of Tables 3–9, whereas those who applied both spatial and spectral validation were cited in the fifth columns.

Table 3. Eligible papers published in 2022.

Remote Image Analyzed	Time Series	Study Area Scale	Spatial Validation Carried Out	Spatial and Spectral Validation Carried Out
AMMIS * (0.5 m) [55]	No	Local	[56,57]	
Apex * (2.5 m) [58]	No	Local	[59]	
ASTER (15–30–90 m) [60]	No	Regional [1]	[61]	
ASTER (15–30 m)	Yes [2]	Local		[62]
AVHRR (1–5 km) [63]	Yes [1]	Regional [1]	[64]	[65,66]
AVIRIS * (10/20 m) [67]	No	Local	[57,68–87]	[88–98]
AVIRIS-NG * (5 m) [99]	No	Local	[100]	
CASI * (2.5 m) [101]	No	Local	[59,78]	
DESIS * (30 m) [102]	Yes [1]	Regional [1]		[103]
DESIS * (30 m)	No	Local		[104]
EnMap * (30 m) [105]	No	Local	[69]	
GaoFen-6 (2–8–16 m) [106]	No	Regional [1]		[107]
GaoFen-2 (3.2 m)	Yes [1]	Regional [1]	[108]	
GaoFen-1 (2–8–16 m)	No	Local	[109]	
HYDICE * (10 m) [110]	No	Local	[59,68,76,77,79,81,82,85,86,90,111]	[89,96,97]
Hyperion * (30 m) [112]	Yes [1]	Local	[75]	
Hyperion * (30 m)	No	Local	[113]	[114–116]
HySpex * (0.6–1.2 m) [104]	No	Local	[104,117]	
Landsat (15–30 m) [118]	Yes [1]	Continental [1]	[119]	
Landsat (15–30 m)	Yes [1]	Regional [1]	[108,120–133]	[134,135]
Landsat (15–30 m)	No	Regional [1]		[107,136,137]
Landsat (15–30 m)	Yes [1]	Local	[138,139]	[62]
Landsat (15–30 m)	No	Local [2]	[140,141]	
Landsat (15–30 m)	No	Local	[109,142]	
M3 hyperspectral image * [143]	No	Moon		[143]
MIVIS * (8 m) [144]	No	Local		[145]
MERIS (300 m) [146]	Yes [1]	Local		[147]
MODIS (0.5–1 km) [148]	Yes [1]	Continental [1]		[149]
MODIS (0.5 km)	Yes [1]	Regional [1]	[108,150–152]	[137]
MODIS (0.5 km)	No	Local	[153]	
NEON * (1 m) [154]	No	Local	[154]	
PRISMA * (30 m) [155]	No	Local		[114,156–158]
ROSIS * (4 m) [159]	No	Local	[56,57,78,81,85]	
Samson * (3.2 m) [59]	No	Local	[59,72]	[89,97]
Sentinel-2 (10–20–60 m) [160]	Yes [1]	Regional [1]	[108,133,161–163]	
Sentinel-2 (10–20–60 m)	No	Regional [1]	[136]	[107,164,165]
Sentinel-2 (10–20–60 m)	Yes [1]	Local	[166,167]	[168]
Sentinel-2 (10–20–60 m)	No	Local [2]		[104]
Sentinel-2 (10–20–60 m)	No	Local		[169]
Specim IQ * [170]	Yes [1]	Laboratory	[170]	
SPOT (10–20 m) [171]	No	Local [2]	[140]	
WorldView-2 (0.46–1.8 m) [172]	No	Local	[166]	
WorldView-3 (0.31–1.24–3.7 m)	No	Local	[166]	

* Hyperspectral sensor; [1] Multiple images acquired from same sensor; [2] Multiple images acquired from different sensors.

Table 4. Eligible papers published in 2021.

Remote Image Analyzed	Time Series	Study Area Scale	Spatial Validation Carried Out	Spatial and Spectral Validation Carried Out
ASTER (15–30–90 m)	No	Regional [1]		[173]
AVIRIS *	No	Local	[174–201]	[202–225]
AVIRIS-NG * (5 m)	No	Local		[226]
CASI *	No	Local	[174,227]	
Simulated EnMAP *	Yes [1]	Regional [1]	[228]	
GaoFen-5 * (30 m)	No	Local		[229]
HYDICE * (10 m)	No	Local	[192,230–232]	[204,212,214,216,218]
HyMap * (4.5 m)	Yes	Local	[233]	
Hyperion * (30 m)	No	Local		[212,234,235]
Hyperion * (30 m)	Yes [1]	Local	[236,237]	
HySpex	No	Local		[238]
Landsat (30 m)	Yes [1]	Regional [1]	[239–244]	
Landsat (30 m)	Yes [1]	Local [2]	[245–253]	
Landsat (30 m)	No	Local	[227,254–259]	
Landsat (30 m)	No	Regional [1]	[260]	
MODIS (0.5–1 km)	No	Local	[254,261]	
MODIS (0.5–1 km)	Yes [1]	Regional [1]	[262–264]	
PRISMA * (30 m)	No	Local		[265]
ROSIS * (4 m)	No	Local	[191,200,266]	[217,267]
Samson * (3.2 m)	No	Local	[188,232,268]	[207,210,211,214,224,225,267]
Sentinel-2 (10–20–60 m)	No	Local	[255,258]	[226,269]
Sentinel-2 (10–20–60 m)	Yes [1]	Local	[243,253,270]	[229,271,272]
Sentinel-2 (10–20–60 m)	No	Regional [1]		[273]
Sentinel-2 (10–20–60 m)	Yes [1]	Regional [1]	[244]	
UAV multispectral image [274]	No	Local	[274]	
WorldView-2 (0.46–1.8 m)	Yes [1]	Local		[275]
WorldView-3 (0.31–1.24–3.7 m)	No	Local [2]	[276]	
ZY-1-02D * (30 m) [228]	No	Local		[228]

* Hyperspectral sensor; [1] Multiple images acquired from same sensor; [2] Multiple images acquired from different sensors.

Table 5. Eligible papers published in 2020.

Remote Image Analyzed	Time Series	Study Area Scale	Spatial Validation Carried Out	Spatial and Spectral Validation Carried Out
AISA Eagle II airborne hyperspectral scanner * [277]	No	Local	[277]	
ASTER (15–30–90 m)	No	Regional [1]	[278]	
ASTER (15–30–90 m)	Yes [1]	Local [2]		[279,280]
AVIRIS *	No	Local	[281–298]	[299–327]
AVIRIS NG *	No	Local	[291]	
AWiFS [328]	Yes [1]	Local [2]	[328]	
CASI *	No	Local	[329]	
Simulated EnMAP * (30 m)	No	Regional [1]	[330]	
GaoFen-1 WFV	Yes [1]	Local	[331]	
GaoFen-1 WFV	Yes [1]	Local [2]	[332]	[333]
GaoFen-2	No	Local [2]	[332]	
HYDICE * (10 m)	No	Local	[292,293,298,334,335]	[299,307,309,310,316,318,321,322,324]
HyMAP *	No	Local [2]		[280]
HyMAP *	No	Local	[336]	
HySpex * (0.7 m)	No	Local	[337]	
Hyperion * (30 m)	No	Local	[336]	[338]
Landsat (30 m)	Yes [1]	Local [2]	[332]	[280,339]
Landsat (30 m)	Yes [1]	Local	[252,340–347]	
Landsat (30 m)	Yes [1]	Continental [1]	[348]	
Landsat (30 m)	Yes [1]	Regional [1]	[349–355]	[356]
Landsat (30 m)	No	Regional [1]	[357]	
MODIS (0.5–1 km)	Yes [1]	Local	[340,358–361]	[333]
MODIS (0.5–1 km)	Yes [1]	Regional [1]	[362,363]	
MODIS (0.5–1 km)	Yes [1]	Local [2]	[364,365]	[279]
PlanetScope (3 m) [366]	Yes [1]	Local [2]	[366]	
PROBA-V (100 m) [367]	Yes [1]	Regional [1]	[353,368–371]	
ROSIS * (4 m)	No	Local	[285,372]	[373]

Table 5. *Cont.*

Remote Image Analyzed	Time Series	Study Area Scale	Spatial Validation Carried Out	Spatial and Spectral Validation Carried Out
Samson * (3.2 m)	No	Local	[284,374,375]	[301,303,305,315,320,323,324]
Sentinel-2 (10–20–60 m)	No	Local [2]	[332,376]	[280,339]
Sentinel-2 (10–20–60 m)	Yes [1]	Local	[328,340,377–382]	[333,383]
Suomi NPP-VIIRS [354]	Yes [1]	Regional [1]	[353]	
UAV hyperspectral data * [384]	Yes [1]	Local		[384]
WorldView-2	Yes [1]	Local	[342]	
WorldView-2	Yes [1]	Local [2]		[385]
WorldView-3	Yes [1]	Local [2]		[385]

* Hyperspectral sensor; [1] Multiple images acquired from same sensor; [2] Multiple images acquired from different sensors.

Table 6. Eligible papers published in 2011.

Remote Image Analyzed	Time Series	Study Area Scale	Spatial Validation Carried Out	Spatial and Spectral Validation Carried Out
AHS * [386]	No	Local		[386]
ASTER	No	Local		[387–389]
ASTER	Yes [1]	Local	[390,391]	
AVIRIS *	No	Local	[307,392–403]	[387,404–417]
CASI *	No	Local		[418]
MERIS (300 m)	No	Local	[419]	
MODIS (0.5–1 km)	Yes [1]	Local	[420–423]	
HYDICE *	No	Local	[392,424]	[414,415,425]
HyMAP *	No	Local	[392,426]	[427]
Hyperion * (30 m)	No	Local		[387,428]
HJ-1 * (30 m) [429]	No	Local	[429,430]	
Landsat (30 m)	Yes [1]	Local	[431–433]	[387]
Landsat (30 m)	No	Local	[434,435]	
Landsat (30 m)	Yes [1]	Local [2]	[436–438]	
Landsat (30 m)	No	Local [2]	[423,439]	
QuickBird (0.6–2.4 m) [440]	No	Local	[441,442]	
SPOT (10–20 m)	No	Local [2]	[439,441]	

* Hyperspectral sensor; [1] Multiple images acquired from same sensor; [2] Multiple images acquired from different sensors.

Table 7. Eligible papers published in 2010.

Remote Image Analyzed	Time Series	Study Area Scale	Spatial Validation Carried Out	Spatial and Spectral Validation Carried Out
Airborne hyper-spectral image * (about 1.5 m) [443]	No	Regional [1]		[443]
AHS * (2.4 m)	No	Local	[444]	
ASTER (15–30–90 m)	Yes [1]	Local	[445,446]	
ASTER (15–30–90 m)	Yes [1]	Regional [1]	[447]	
ATM (2 m) [101]	No	Local [2]		[101]
AVHRR (1 km)	Yes [1]	Regional [1]	[448]	
AVIRIS * (20 m)	No	Local	[449–457]	[458–463]
CASI * (2 m)	No	Local		[101]
CASI *	No	Laboratory		[464,465]
CHRIS * (17 m) [466]	No	Local	[467]	
DAIS * (6 m) [464]	No	Local	[465]	
DESIS *	No	Local		[468,469]
HYDICE *	No	Local	[455,470,471]	[458,463]
HyMAP *	No	Local	[471]	
Hyperion * (30 m)	No	Local	[472–474]	
HJ-1 * (30 m)	No	Local	[475,476]	

Table 7. *Cont.*

Remote Image Analyzed	Time Series	Study Area Scale	Spatial Validation Carried Out	Spatial and Spectral Validation Carried Out
Landsat (30 m)	Yes [1]	Regional [1]	[477–483]	
Landsat (30 m)	No	Regional [1]	[484–489]	[490]
Landsat (30 m)	No	Local [2]	[491,492]	
Landsat (30 m)	No	Local	[493]	
MIVIS * (3 m)	No	Regional [1]	[494]	
MODIS (0.5–1 km)	Yes [1]	Regional [1]	[495]	
MODIS (0.5–1 km)	Yes [1]	Continental [1]	[496]	
QuickBird (2.4 m)	No	Local [2]	[491]	
QuickBird (2.4 m)	No	Local	[497,498]	
SPOT (10–20 m)	Yes [1]	Regional [1]	[480]	
SPOT (2.5–10–20 m)	No	Local [2]	[486,491,492]	
SPOT (2.5–10–20 m)	No	Local	[499]	[500]

* Hyperspectral sensor; [1] Multiple images acquired from same sensor; [2] Multiple images acquired from different sensors.

Table 8. Eligible papers published in 1996.

Remote Image Analyzed	Time Series	Study Area Scale	Spatial Validation Carried Out	Spatial and Spectral Validation Carried Out
AVIRIS *	No	Local	[501,502]	[503]
GERIS * [504]	No	Local	[504]	
Landsat (30 m)	No	Local	[14,505]	[506]
SPOT (2.5–10–20 m)	No	Local	[507]	

* Hyperspectral sensor.

Table 9. Eligible papers published in 1995.

Remote Image Analyzed	Time Series	Study Area Scale	Spatial Validation Carried Out	Spatial and Spectral Validation Carried Out
AVHRR (1–5 km)	Yes [1]	Regional [1]		[508]
AVIRIS * (20 m)	No	Local	[509]	[510,511]
Landsat (30 m)	No	Local	[512]	[513]
MIVIS * (4 m)	No	Local	[514]	
MMR * [515]	Yes [1]	Local	[515]	

* Hyperspectral sensor; [1] Multiple images acquired from same sensor.

The first columns of Tables 3–9 and the second columns of Tables A1–A7 show the sensor name and the spatial resolution of the images. Considering all eligible papers, 27 hyperspectral sensors and 16 multispectral sensors were employed. Hyperspectral sensors were highlighted in the first columns of Tables 3–9 with an asterisk. The literature often combined spectral unmixing with hyperspectral data because the number of bands must be greater than the number of endmembers [4,5,42,44]. However, the percentage of papers that employed hyperspectral data (57% of a total of 458 papers) is slightly higher than the percentage of papers that employed multispectral data (43% of a total of 458 papers). The second columns of Tables 3–9 show the papers that performed the time series studies, whereas the third columns of these tables show the papers that performed the local, regional, or continental studies.

The analysis of these data showed that most studies that analyzed hyperspectral images were performed at the local scale and did not carry out the multitemporal studies, whereas most studies that analyzed multispectral images were performed at the regional or continental scale and carried out the multitemporal studies (more than one image was analyzed). Therefore, the spectral unmixing is widely applied to multispectral images, despite their smaller number of bands than hyperspectral images, because these data are characterized by greater spatial and temporal availability than those of the hyperspectral data.

Moreover, the spectral unmixing was also applied to some hyperspectral and multispectral images that were characterized with high spatial resolutions (e.g., AMMIS image with spatial resolution equal to 0.5 m [56] and WorldView-3 image with spatial resolution of 0.31 m [166]). These papers confirm that, no matter how high the spatial resolution might be, no image pixel results were completely homogeneous in spectral characteristics [9,516,517].

3.3. Accuracy Metrics

Accuracy, which is defined as "the degree of correctness of the map", is usually assessed by comparing the "ground truth" with the map retrieved from remote images [518,519]. Because no map can fully and completely map the territory [520], ground truth is more correctly called reference data [521]. To assess the differences between the reference data and results of the spectral unmixing, the eligible papers exploited different metrics. Figure 3 shows the pie chart of the distribution of the metrics that were adopted by eligible papers.

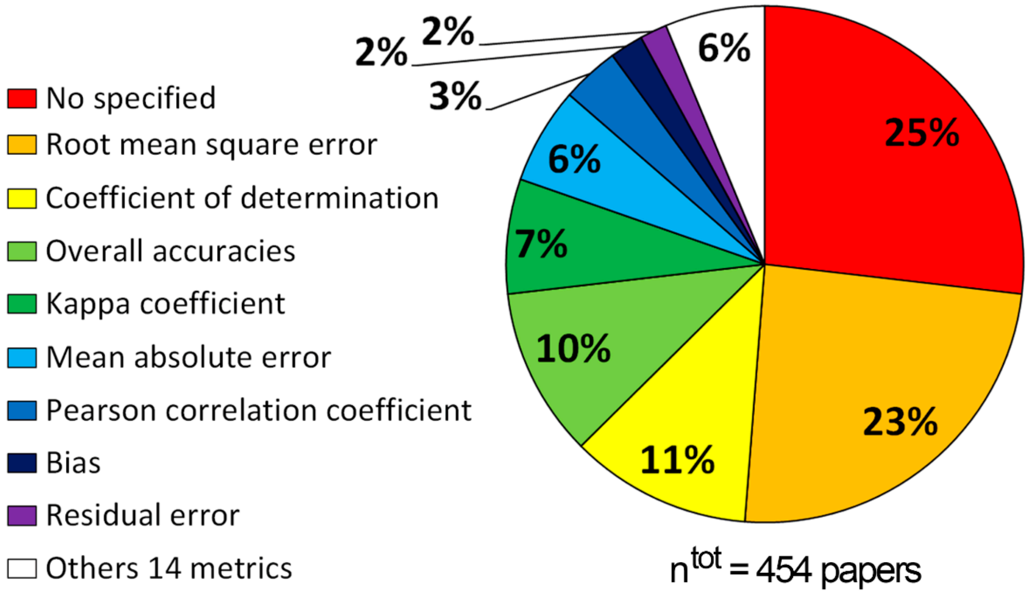

Figure 3. Distribution of the eligible papers according to the metrics employed to evaluate the spatial accuracy.

The other 14 metrics were average accuracy [522], correct labeling percentage for the unchanged pixels [141], correlation coefficient [150], Kling–Gupta efficiency [523], mean abundance error [117], mean error [169], mean relative error [169], normalized average of spectral similarity measures [524], producer's accuracy [153], Receiver Operating characteristic Curves (ROC) method [525], relative mean bias [165], separability spectral index [526], signal-to-reconstruction error [56], and systematic error [109].

In conclusion, the authors of 454 eligible papers employed 22 different metrics, and most authors employed more than 1 metric. Overall, 25% of the eligible papers did not specify the accuracy metrics used. It is very important to note that some standard accuracy assessments, such as the kappa coefficient, "assume implicitly that each of the testing samples is pure"; therefore, some of these metrics were inappropriate for evaluating the accuracy of the fractional abundance maps [41,518].

3.4. Key Issues in the Spatial Validation

Since the literature highlighted many sources of error in accuracy assessment of retrieved maps [518,519,521], the authors identified and carried out several "key issues" to address and minimize these errors. Figure 4 and Tables A1–A7 summarize the key issues that were identified.

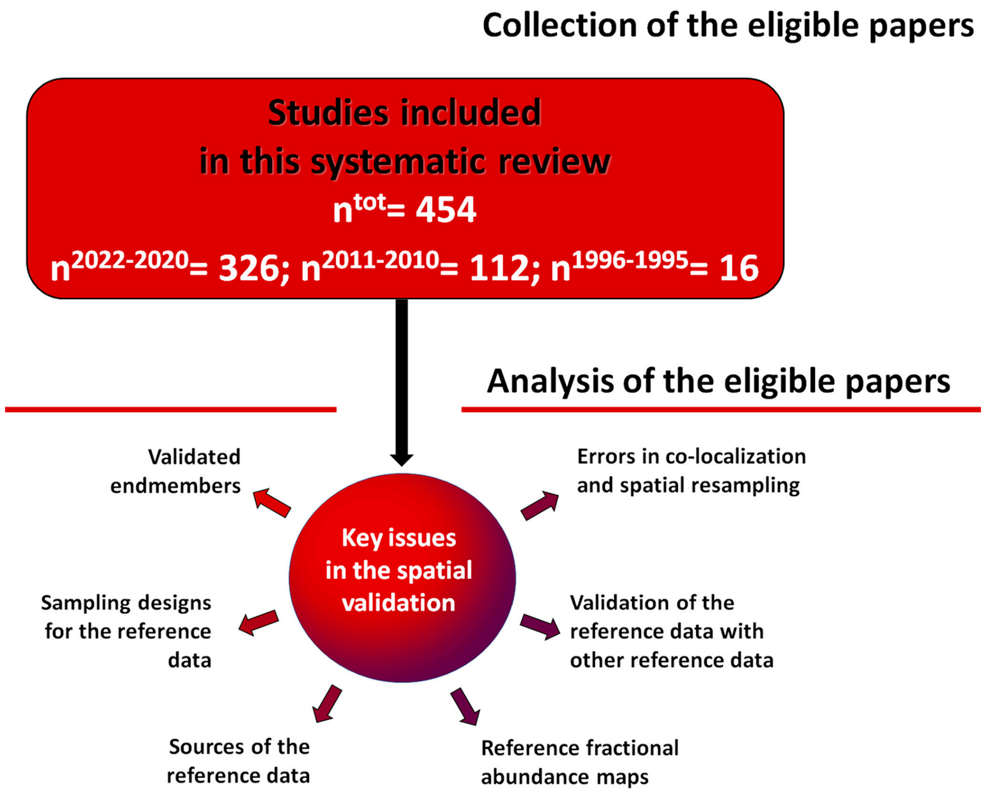

Figure 4. Key issues in the spatial validation that were addressed by the eligible papers.

3.4.1. Validated Endmembers

Before analyzing the endmembers that were validated, it is necessary to remember that the number of endmembers that were determined with the images must be less than the number of sensor bands; therefore, the number of endmembers that were determined with the multispectral data is less than the number of endmembers that were determined with the hyperspectral data [6,23,527]. Therefore, the authors who elaborated the multispectral images employed smaller levels of model complexity than authors who elaborated the hyperspectral images [528,529]. For example, the VIS model was used to map only three endmembers (Vegetation, Impervious surfaces, and Soil) in many urban areas that were retrieved from multispectral data (e.g., [109,152,477,493]).

The third columns of Tables A1–A7 list the endmembers that were determined using spectral unmixing; the fourth columns of these showed the number of these endmembers that were validated. It is interesting to note that some authors validated smaller number of endmembers than the number of the endmembers that were determined (i.e., 40 eligible papers). Dividing the works that analyzed hyperspectral images from those that analyzed multispectral data, Figure 5 shows the percentage of studies that validated the total or partial number of endmembers. It is important to highlight that, since 4 eligible papers analyzed both hyperspectral and multispectral data [104,227,231,281], the sum of papers that analyzed hyperspectral data and papers that analyzed multispectral data (i.e., 458) is greater than the number of eligible papers (i.e., 454).

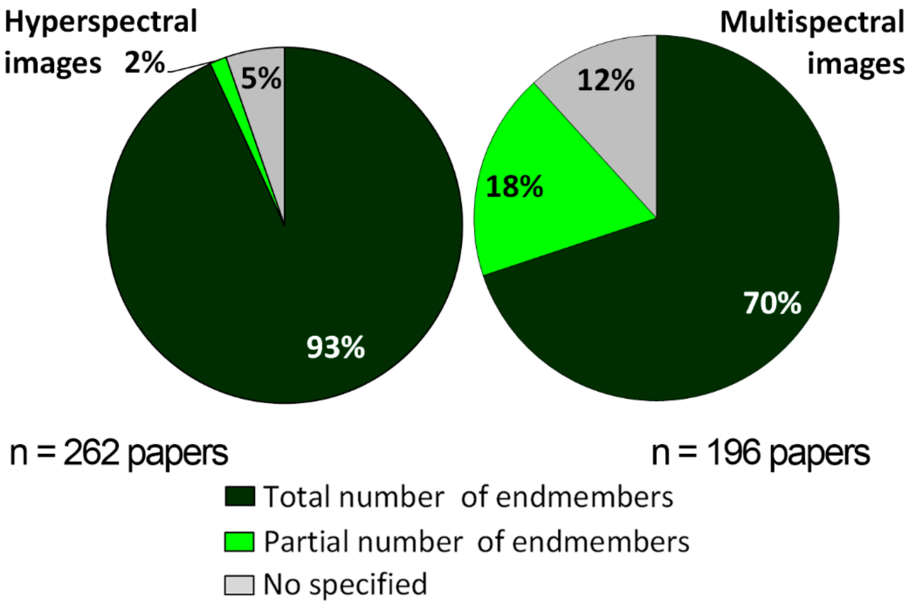

Figure 5. Distribution of the eligible papers that fully or partially validated endmembers determined with hyperspectral images (**right**) or multispectral images (**left**), where n was the number of papers considered in each pie chart.

Therefore, only 2% of the studies that elaborated hyperspectral images partially validated the determined endmembers, whereas 18% of the studies that elaborated multispectral images partially validated the determined endmembers. As mentioned above, hyperspectral images were used to carry out non-repeated surveys over time and at local-scale studies (252 papers of a total of 262), whereas most multispectral images were used to carry out regional- or continental-scale studies that were or were not repeated over time (180 papers of a total of 196). Therefore, some of these authors, who analyzed more than one image, chose to spatially validate only the materials or groups of materials on which they focused their study. For example, Hu et al. [149] spatially validated only blue ice fractional abundance maps that were retrieved from MODIS images covering the period 2000–2021 in order to present a FABIAN (Fractional Austral-summer Blue Ice over Antarctica) product. It should be noted that 5 and 12% of the papers that analyzed hyperspectral or multispectral data, respectively, did not specify which endmembers were validated.

3.4.2. Sampling Designs for the Reference Data

The literature demonstrated that a possible source of error in spatial validation is due to the choice of the sampling design for the reference data [518,519,521,530]. The sampling design mainly includes the definition of the sample size and the sampling design of the reference data [518]. Authors of eligible papers chose three kinds of sample sizes: the whole study area; the representative area; small sample sizes (pixels, plots, and polygons samples). The eighth columns of Tables A1–A7 show the different sample sizes that were adopted by every eligible paper, and Table 10 shows the number of papers that adopted the different sample sizes.

Table 10. Sample sizes of the reference data that were employed by the eligible papers.

Sample Sizes of the Reference Data	Papers Published in 2022, 2021, and 2020	Papers Published in 2011 and 2010	Papers Published in 1996 and 1995
Whole study area	172	55	10
Small sample sizes	78	38	1
Representative area	21	7	0
Not specified	59	12	5

Most authors of the eligible papers chose to validate the whole study areas, followed, in descending order, by the choice to employ the different number of small sample sizes and then the representative areas. It is also important to note the high percentages of the papers that did not specify the sample size of the reference data: 18, 11, and 31%, respectively.

The literature also pointed out that the sampling designs for spatially validating maps at local scale cannot be the same as the designs for spatially validating maps at regional or continental scale [518,530]. As mentioned above, most of the studies that analyzed the hyperspectral data were performed at local scale (252 papers of a total of 262), whereas the studies that analyzed the multispectral images performed at regional or continental scale (180 papers of a total of 196). Therefore, the eligible papers that analyzed hyperspectral images were analyzed separately from those that analyzed multispectral images (Figure 6 on the right and left, respectively), not only to analyze the different sampling designs adopted from the hyperspectral and multispectral data, but also to highlight the different sampling designs chosen for local or regional/continental scale studies. Figure 6 shows the percentage of the eligible papers that employed the different sample sizes and the percentage of the eligible papers that employed a different number of small sample sizes.

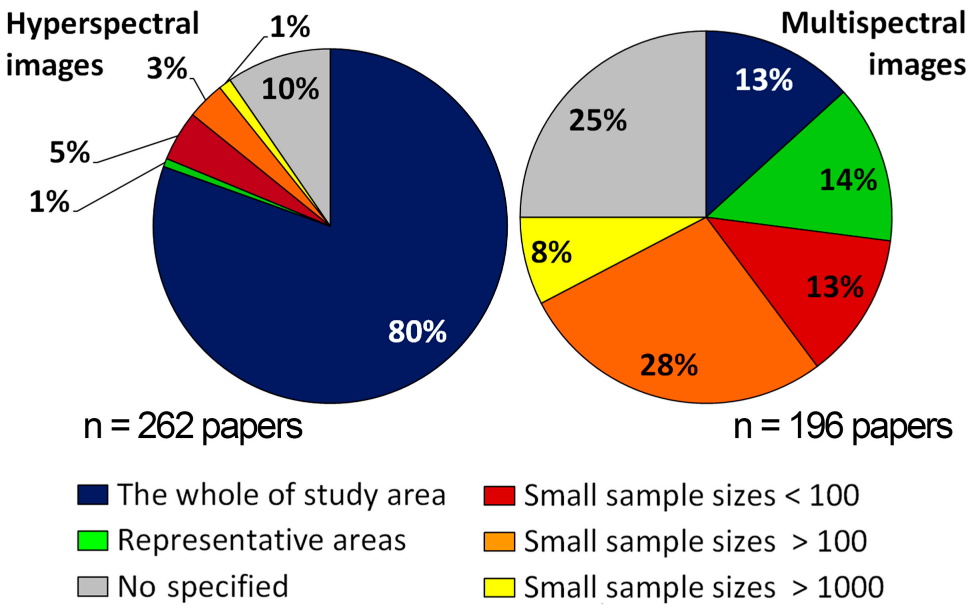

Figure 6. Distribution of the eligible papers according to the sample sizes and the number of the small sample sizes that were chosen to analyze hyperspectral (**right**) or multispectral (**left**) images, where n was the number of papers considered in each pie chart.

Most papers that processed hyperspectral images validated the whole study area (212 papers), whereas most papers that processed multispectral images employed small sample sizes (94 papers).

The authors of eligible papers that employed small sample sizes adopted three different sampling designs of reference data: partial, random, and uniform. The ninth columns of Tables A1–A7 show the sampling designs of every eligible paper. Most authors who published in 2022, 2021, and 2020 and published in 2011 and 2010 chose the random distribution of reference data (78% for a total of 326 papers and 76% for a total of 110 papers, respectively), whereas the authors who published in 1996 and 1995 did not specify the sampling designs employed. Stehman and Foody [519] highlighted that "the most commonly used designs" that were chosen to assess the land cover products were "simple random, stratified random, systematic, and cluster" designs. Therefore, these results confirmed that random designs were the most commonly used approaches.

3.4.3. Sources of the Reference Data

Eligible papers employed four different sources of reference data to spatially validate spectral unmixing results: images, in situ data, maps, and previous reference maps. Table 11 shows the number of the eligible papers that employed these reference data sources, whereas the fifth columns of Tables A1–A7 detail the sources of the reference data.

Table 11. Reference data sources employed by the eligible papers.

Sources of Reference Data	Papers Published in 2022, 2021, and 2020	Papers Published in 2011 and 2010	Papers Published in 1996 and 1995
Maps	13	2	8
In situ data	55	35	2
Images	106	31	6
Previous reference maps	156	44	0

The number of authors who chose to utilize geological, land use, or land cover maps as reference maps is the smallest (5% of the total eligible papers), followed, in ascending order, by the number who chose to create the reference maps using in situ data (20% of the total eligible papers), and then by the number of authors who chose to create the reference maps using other images (31% of the total eligible papers). Firstly, the number of authors who chose to use the previous reference maps is the largest (44% of the total eligible papers).

As regards the authors who chose to create the reference maps using other images, most of them employed images at higher spatial resolutions than those of the remote images analyzed (95% of a total of 143 papers). To create the reference maps from the images, 47% of the eligible papers did not specify the method used to map the endmembers, 29% employed the photo-interpretation, 21% classified the images, 2% used the vegetation indexes, and 2% used the mixed approach by classifying and/or photo-interpreting and/or applying vegetation indexes (e.g., [114,145,531]). As regards the classification methods, there are four works that applied the same classification procedure to analyze the remote images and to create the reference maps [65,66,149,261]. Among these, the authors of 3 papers compared the fractional abundance maps that were retrieved from the multispectral images at moderate spatial resolutions (10, 30, and 60 m) with the fractional abundance maps that were retrieved from the multispectral data at coarse spatial resolutions (0.5 and 1 km) [65,66,149].

Moreover, the reference data sources that were chosen to validate the results of the hyperspectral images were analyzed separately from those that were chosen to validate the results of the multispectral images. Figure 7 shows the percentage of the papers that adopted the different sources of the reference data to validate the results of hyperspectral (right) and multispectral data (left).

As regards the papers that analyzed the multispectral data, most of the authors chose to create the reference maps from the other images, whereas most of the authors that analyzed the hyperspectral data chose to employ the previous reference maps. It is important to emphasize that 97% of these reference maps are available online together with hyperspectral images and/or reference spectral libraries (e.g., [532–535] Figure 8). Therefore, these images were well known: Cuprite (NV, USA, e.g., [70,458]), Indian Pines (IN, USA, e.g., [78,458]), Jasper Ridge (CA, USA, e.g., [68,97]), Salinas Valley (CA, USA, e.g., [75,78]) datasets that were acquired with AVIRIS sensors; Pavia (Italy, e.g., [81,85]) datasets that were acquired with the ROSIS sensor; Samson (FL, USA, e.g., [59,89]) dataset that was acquired with the Samson sensor; University of Houston (TX, USA, e.g., [59,78]) dataset that was acquired with the CASI-1500 sensor; Urban (TX, USA, e.g., [59,68]) and Washington DC Mall (Washington, DC, USA, e.g., [81,90]) datasets that were acquired with the HYDICE sensor.

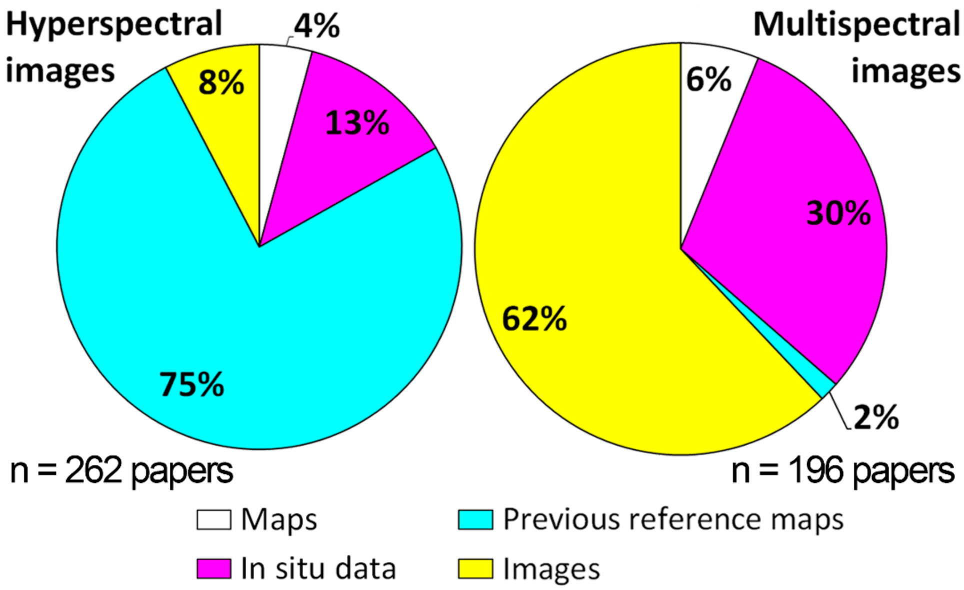

Figure 7. Distribution of the eligible papers according to the reference data sources that were chosen to analyze hyperspectral (**right**) or multispectral (**left**) images, where n was the total number of papers considered in each pie chart.

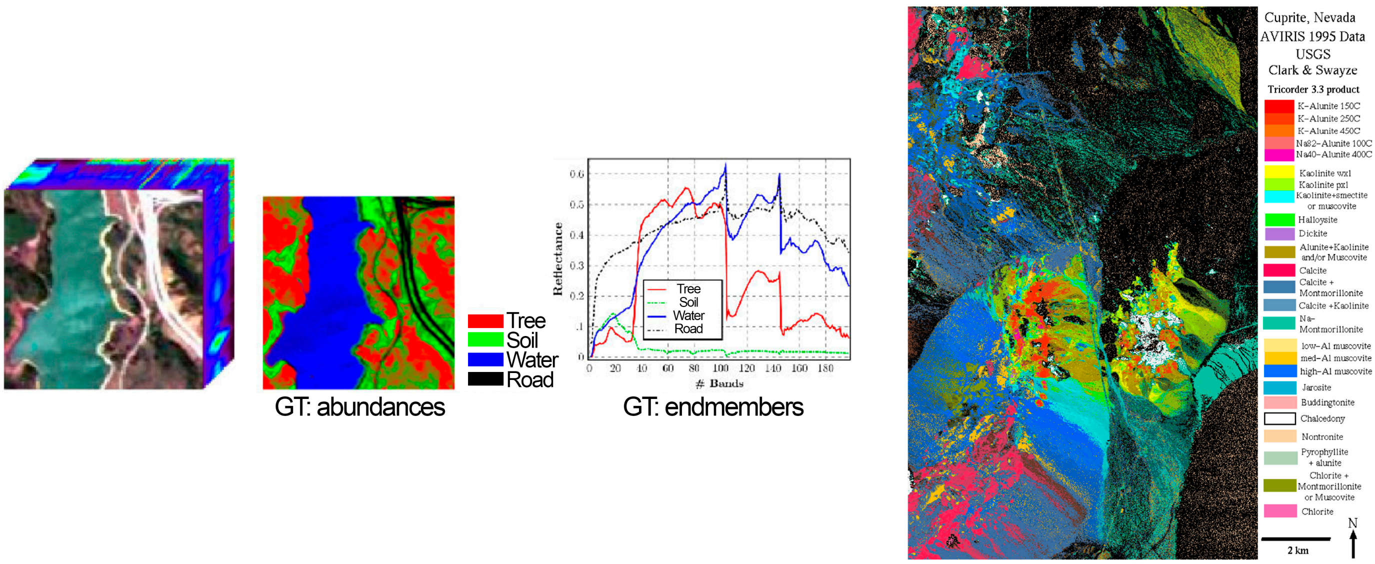

(**a**) (**b**)

Figure 8. *Cont.*

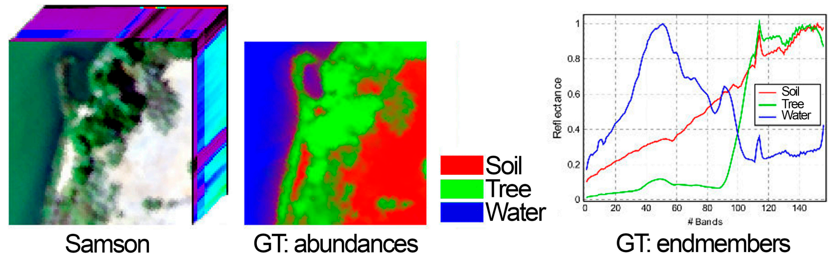

(**c**)

Pines scene and their respective samples number

#	Class	Samples
1	Alfalfa	46
2	Corn-notill	1428
3	Corn-mintill	830
4	Corn	237
5	Grass-pasture	483
6	Grass-trees	730
7	Grass-pasture-mowed	28
8	Hay-windrowed	478
9	Oats	20
10	Soybean-notill	972
11	Soybean-mintill	2455
12	Soybean-clean	593
13	Wheat	205
14	Woods	1265
15	Buildings-Grass-Trees-Drives	386
16	Stone-Steel-Towers	93

Sample band of Indian Pines dataset

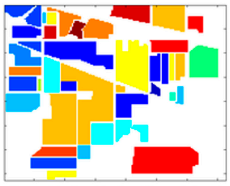

Ground truth of Indian Pines dataset

(**d**)

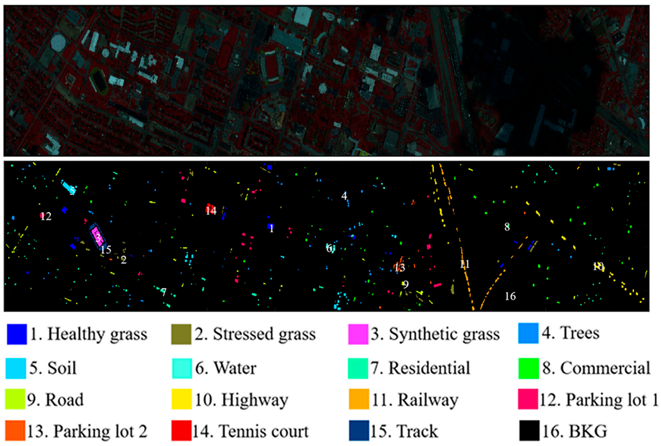

(**e**)

Ground truth classes for the Salinas scene and their respective samples number

#	Class	Samples
1	Brocoli_green_weeds_1	2009
2	Brocoli_green_weeds_2	3726
3	Fallow	1976
4	Fallow_rough_plow	1394
5	Fallow_smooth	2678
6	Stubble	3959
7	Celery	3579
8	Grapes_untrained	11271
9	Soil_vinyard_develop	6203
10	Corn_senesced_green_weeds	3278
11	Lettuce_romaine_4wk	1068
12	Lettuce_romaine_5wk	1927
13	Lettuce_romaine_6wk	916
14	Lettuce_romaine_7wk	1070
15	Vinyard_untrained	7268
16	Vinyard_vertical_trellis	1807

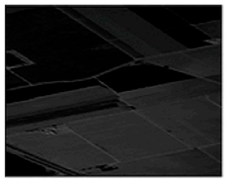

Sample band of Salinas dataset

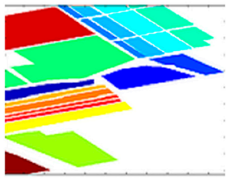

Ground truth of Salinas dataset

(**f**)

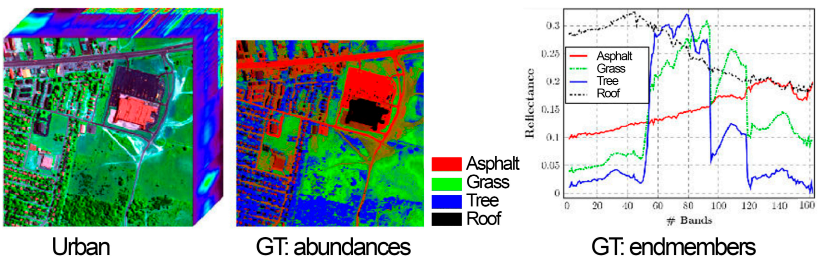

(**g**)

Ground truth classes for the Pavia University scene and their respective samples number

#	Class	Samples
1	Asphalt	6631
2	Meadows	18649
3	Gravel	2099
4	Trees	3064
5	Painted metal sheets	1345
6	Bare Soil	5029
7	Bitumen	1330
8	Self-Blocking Bricks	3682
9	Shadows	947

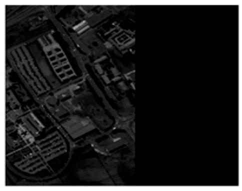

Sample band of Pavia University dataset

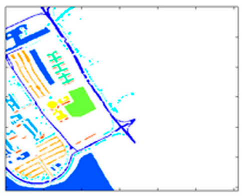

Ground truth of Pavia University dataset

(**h**)

Figure 8. *Cont.*

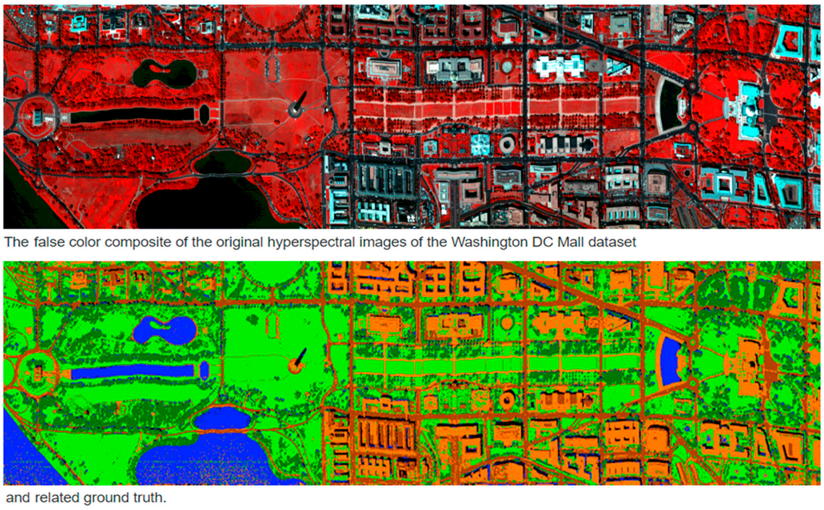

(**i**)

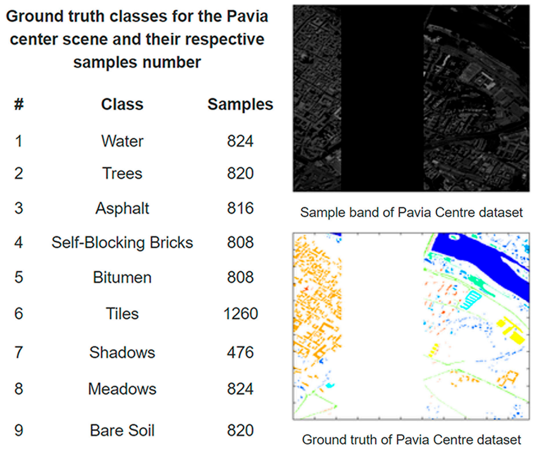

(**j**)

Figure 8. Reference data available online together with hyperspectral images: (**a**) Jasper Ridge reference map and spectral library [535]; (**b**) Cuprite reference map [536]; (**c**) Samson reference map and spectral library [535]; (**d**) Indian Pines reference map [535]; (**e**) University of Houston reference map [535]; (**f**) Salinas Valley reference map [535]; (**g**) Urban reference map [535]; (**h**) Pavia University reference map [535]; (**i**) Washington DC reference map [535]; (**j**) Pavia center reference map [535].

Moreover, 93% of these papers proposed a method and tested it not only on these "real" hyperspectral data, but also on created synthetic images. Borsoi et al. [4] highlighted that in order to overcome "the difficulty in collecting ground truth data", some authors generated synthetic images. However, the authors complained because "there is not a clearly agreed-upon protocol to generate realistic synthetic data" [4].

3.4.4. Reference Fractional Abundance Maps

"Misclassifications" of the reference data or "misallocations of the reference data" are another possible source of error in spatial validation, defined as "imperfect reference data" by [519] or "error magnitude" by [518]. The authors highlighted that these errors can be caused also by the use of "standard" reference maps to validate the spectral unmixing results (i.e., the fractional abundance maps) [41,518,519]. The difference between standard reference maps and reference fractional abundance maps is that each pixel of the standard reference map is assigned to a corresponding land cover class, whereas each pixel of the reference fractional abundance map is labeled with the fractional abundances of each endmember that is present in that pixel. Therefore, the values of the standard reference map are equal to 0 or 1, whereas the values of the reference fractional abundance map are greater than 2 and vary between 0 and 1 (100 values are able to fully validate the fractional abundance of endmembers [114]).

The reference fractional abundance maps were employed by 133 eligible papers that were published in 2022, 2021, and 2020; by 62 eligible papers that were published in 2011 and 2010; and by 13 eligible papers that were published in 1996 and 1995 (45% of the total eligible papers). Moreover, among these works, 87, 47, and 8 papers estimated the full range of abundances using 100 values (31% of the total eligible papers), whereas 41, 10, and 5 works partially estimated the fractional abundances using less than 100 values (12% of the total eligible papers). It is important to note that 7% of the total eligible papers did not specify if they used the standard reference maps or the reference fractional abundance maps.

The eligible papers were separately analyzed according to reference data sources that were adopted in order to find out how fractional abundances were estimated. In the four parts of Figure 9, the eligible papers that were clustered according to the reference data sources are shown, and each part of Figure 9 shows the percentage of the papers that did not specify the reference maps used and the number of the papers that fully or partially estimated the reference fractional abundance maps.

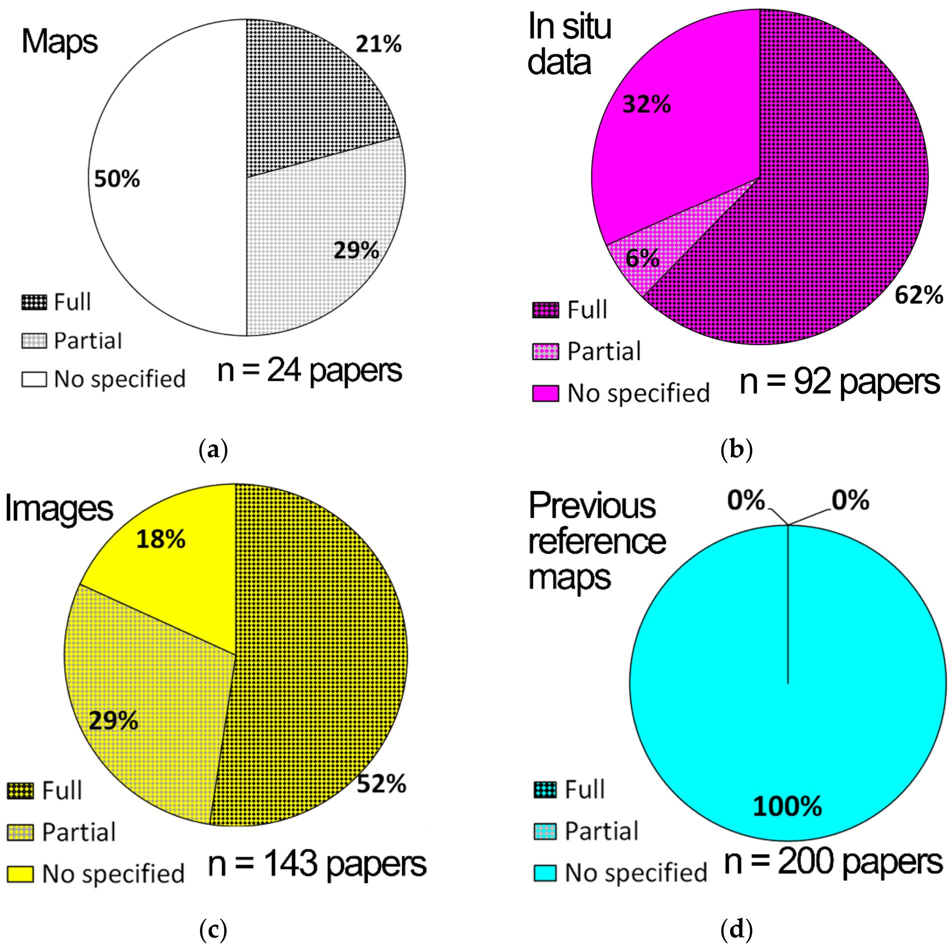

Figure 9. Distribution of the eligible papers that did not specify the reference maps used, fully and partially estimated fractional abundances according to the reference data sources, where n was the total number of papers that were clustered according to the reference data sources and included in the pie charts: (**a**) The papers that employed the maps; (**b**) The papers that employed in situ data; (**c**) The papers that employed the images; (**d**) The papers that employed the previous reference maps.

High-spatial-resolution images were the most widely employed to make the reference fractional abundance maps (81% of the total papers that employed the images), followed by in situ data (68% of the total papers that employed in situ data), and then the maps (50% of the total papers that employed maps). Moreover, in situ data were the most widely employed to estimate the full range of fractional abundances (62% of the total papers that employed in situ data), followed by high-spatial-resolution images (52% of the total papers that employed the images), and then the maps (21% of the total papers that employed the images). The previous reference maps were not employed to make the reference fractional abundance maps.

Many authors highlighted that it is not easy to create the reference fractional abundances maps (e.g., [4,6,518,519]). Cavalli [145] implemented a method that was proposed by [537] in order to create the reference fractional abundance maps. This method is able to create the reference fractional abundance maps by varying the spatial resolution of the high-resolution reference maps several times, and the range of fractional abundances can be fully estimated according to the spatial resolution of the reference maps [114].

3.4.5. Validation of the Reference Data with Other Reference Data

In order to further minimize the errors due to "misclassifications" or "misallocations of the reference data" [518,519], some authors validated the reference data using other reference data: 61 eligible papers published in 2022, 2021, and 2020; 21 eligible papers published in 2011 and 2010; 4 eligible papers published in 1996 and 1995. Therefore, 81% of the total eligible papers did not take into consideration that the reference map may not be "ground truth" and may be "imperfect" [519,520].

It is very important to point out that some authors took advantage of the online availability of reference data to validate reference data (e.g., [114,123,127,140,145,152,231,448,496]). Many efforts are being made to create the networks of accurate validation data [48,538–540]. For example, Zhao et al. [140] exploited in situ measurements of the Leaf Area Index (LAI) that were provided by the VALERI project [540], whereas Halbgewachs et al. [123], Lu et al. [423], Shimabukuro et al. [353], and Tarazona Coronel [127] utilized validation data that were provided by the Program for Monitoring Deforestation in the Brazilian Amazon (PRODES) [541].

3.4.6. Error in Co-Localization and Spatial Resampling

The key issues described above addressed only the errors in the thematic accuracy of the spectral unmixing results [518,519], whereas this key issue aimed to address the geometric errors due to the comparison of remote images with reference data [542]. The impact of co-localization and spatial resampling errors was minimized and/or evaluated by 6% of the eligible papers: 20 eligible papers published in 2022, 2021, and 2020; 8 eligible papers published in 2011 and 2010; 1 eligible paper published in 1996. In order to minimized the errors, Arai et al. [368], Cao et al. [164], Li et al. [107], Soenen et al. [500], and Zurita-Milla et al. [419] carefully chose the size of the reference maps; Bair et al. [254], Cavalli [114,145], Ding et al. [152], Fernandez-Garcia et al. [256], Hamada et al. [441], Hajnal et al. [169], Lu et al. [435], Ma & Chan [78], Rittger et al. [262], Sun et al. [263], Yang et al. [488], and Yin et al. [151] spatially resampled the reference fractional abundance maps; Estes et al. [447] compared different windows of pixels (i.e., 3×3, 7×7, 11×11, 15×15, and 21×21); Pacheco & McNairn [480] selected the size and the spatial resolution of the reference maps; Ben-dor et al. [507], Fernandez-Guisuraga et al. [342], Kompella et al. [328], Laamarani et al. [343], and Plaza & Plaza [465] carefully co-localized the reference fractional abundance maps on the reference maps; Wang et al. [366] expanded the windows of the field sample size; Zhu et al. [64] resampled at "four kinds of grids" (i.e., 1100×1100 m, 2200×2200 m, 4400×4400 m, and 8800×8800 m) the reference fractional abundance map and compared the results. Bair et al. [254], Binh et al. [341], Cavalli [114,145], Cheng et al. [543], and Ruescas et al. [448] evaluated the errors in co-localization and spatial-resampling due to the comparison of different data at different spatial resolutions. Moreover, Cavalli [145] proposed a method to minimize the errors: the comparison of the histograms of the reference fractional abundance values with the histograms of the retrieved fractional abundance values.

It is important to point out that 94% of the total papers did not address the geometric errors due to the comparison of remote images with reference data.

4. Conclusions

The term validation is defined as "the process of assessing, by independent means, the quality of the data products derived from the system outputs" by the Working Group on Calibration and Validation (WGCV) of the Committee on Earth Observing Satellites (CEOS) [48]. Since 1969, research has been involved to establish shared key issues to validate the land cover products that were retrieved from the remote images [518,519,539,544]. These products can be obtained by applying classifications called "hard", because they extract information only from "pure pixels," and classifications called "soft", because they also extract information from "mixed pixels" [519,544]. However, not only the literature related to the spatial validation, but also every review on the spectral unmixing procedure (i.e., a soft classification) highlighted that the key issues in the spatial validation of soft classification results have yet to be clearly established and shared (e.g., [4,6,518,519]).

Since no review was performed on this fundamental topic, this systematic review aims (a) to identify and analyze how the authors addressed the spatial validation of spectral unmixing results and (b) to provide readers with recommendations for overcoming the many shortcomings of spatial validation and minimizing its errors. The papers published in 2022, 2021, and 2020 were considered to analyze the current status of spatial validation, and the papers published not only in 2011 and 2010, but also in 1996 and 1995, were considered to analyze its progress over time. Since the literature on spectral unmixing is extensive, only papers published in these seven years were considered. A total of 454 eligible papers were included in this systematic review and showed that the authors addressed 6 key issues in the spatial validation. In this text, the order in which the key issues were presented is not an order of importance.

1. The first key issue concerned the number of the endmembers validated. Some authors chose to focus on only one or two endmembers, and only these were spatially validated. This key issue was designed to facilitate the conduct of regional- or continental-scale studies and/or multitemporal analysis. It is important to note that 8% of the eligible papers did not specify which endmembers were validated.
2. The second key issue concerned the sampling designs for the reference data. The authors who analyzed hyperspectral images preferred to validate the whole study area, whereas those who analyzed multispectral images preferred to validate small sample sizes that were randomly distributed. It is important to point out that 16% of the eligible papers did not specify the sampling designs for the reference data.
3. The third key issue concerned the reference data sources. The authors who analyzed hyperspectral images primarily used the previously referenced maps and secondarily created reference maps using in situ data, whereas the authors who analyzed multispectral images chose to create reference maps primarily using high-spatial-resolution images and secondarily using in situ data.
4. The fourth key issue was, perhaps, the one most closely related to the spectral unmixing procedure; it concerned the creation of the reference fractional abundance maps. Only 45% of the eligible papers created the reference fractional abundance maps to spatially validate the fractional abundance maps retrieved. These mainly employed high-resolution images and secondarily in situ data. Therefore, 55% of the eligible papers did not specify the employment of the reference fractional abundance maps.
5. The fifth key issue concerned the validation of the reference data with other reference data; it was addressed only by 19% of the eligible papers. Therefore, 81% of the eligible papers did not validate the reference data.
6. The sixth key issue concerned the error in co-localization and spatial resampling data, which was minimized and/or evaluated only by 6% of the eligible papers. Therefore, 94% of the eligible papers did not address the error in co-localization and spatial resampling data.

In conclusion, to spatially validate the spectral unmixing results and minimize and/or evaluate its errors, six key issues were considered not only from the eligible papers published in 2022, 2021 and 2020, but also from those published in 2010, 2011, 1996, and 1995. In addition, the results obtained from both hyperspectral and multispectral data were spatially validated considering all key issues, but these were addressed in different ways. All six key issues addressed together enabled rigorous spatial validation to be performed. Therefore, this systematic review provided readers with the most suitable tool to rigorously address spatial validation of the spectral unmixing results and minimize its errors.

The key difference between reference data suitable for hard and soft classifications is that the latter reference maps must have higher spatial resolution than the resolutions of the image pixels [6,114,518]. The optimal scale would be that 100 times larger than the image pixel resolution [114]. However, many hyperspectral data were validated using the previous reference maps at the same spatial resolution as the remote image, so these standard reference maps can only create reference fractional abundance maps with the help of other reference data. The employment of the standard reference maps instead of the reference fractional abundance maps was also evidenced by the employment of metrics to assess spatial accuracy that "assume implicitly that each of the testing samples is pure" [37,217].

However, only 4% of eligible papers addressed every key issue, and many authors did not specify which approach they employed to spatially validate the spectral unmixing results. Moreover, most of the authors who specified the approach employed did not adequately explain the methods used and the reasons for their choices. Six "good practice criteria to guide accuracy assessment methods and reporting" were identified by [519]. Therefore, these papers did not fully meet three good practice criteria: "reliable", "transparent", and "reproducible" [519].

Funding: This research received no external funding.

Data Availability Statement: Not applicable.

Conflicts of Interest: The authors declare no conflict of interest.

Appendix A

In accordance with the PRISMA statement [49,50], 454 eligible papers were identified, screened, and included in this systematic review: 326 eligible papers were published in 2022, 2021, and 2020; 112 eligible papers were published in 2011 and 2010; 16 eligible papers were published in 1996 and 1995. The eligible criterion was that the results of the spectral unmixing were spatially validated. Analyzing these papers, six key issues were identified that were differently addressed to spatially validate the spectral unmixing results. The different ways in which the key issues were addressed by the eligible papers published in 2022, 2021, 2020, 2011, 2010, 1996, and 1995 are summarized in Tables A1–A7, respectively.

Table A1. Main characteristics of the eligible papers that were published in 2022.

Paper	Remote Image	Determined Endmembers	Validated Endmembers	Sources of Reference Data	Method for Mapping the Endmembers	Validation of Reference Data with Other Reference Data	Sample Sizes and Number of Small Sample Sizes	Sampling Designs	Reference Data	Estimation of Fractional Abundances	Error in Co-Localization and Spatial Resampling
Abay et al. [62]	ASTER (15–30 m) Landsat OLI (30 m)	Goethite, hematite	All	Geological map	-	In situ observations	-	-	Reference map	-	-
Ambarwulan et al. [147]	MERIS (300 m)	Several total suspended matter concentrations	All	In situ data	-	-	171 samples	-	-	-	-
Benhalouche et al. [156]	PRISMA (30 m)	Hematite, magnetite, limonite, goethite, apatite	All	In situ data	-	-	-	-	-	-	-
Bera et al. [120]	Landsat TM, ETM+, OLI (30 m)	Vegetation, impervious surface, soil	All	Google Earth images	Photointerpretation	Soil map	101 polygons	Uniform	Reference fractional abundance maps	Partial	-
Brice et al. [121]	Landsat TM, OLI (30 m)	Water, wetland vegetation, trees, grassland	1	Planet images (4 m)	Photointerpretation	In situ observations	427 wetlands	-	Reference fractional abundance map	Partial	-
Cao et al. [164]	Sentinel-2 (10–20–60 m)	Vegetation, high albedo impervious surface, low albedo impervious surface, soil	All	GaoFen-2(0.8–3.8 m)	Photointerpretation	In situ observations	300 squares (100 × 100 m)	Stratified random	Reference fractional abundance maps	Partial	Polygon size
Cavalli [114]	Hyperion (30 m) PRISMA (30 m)	Lateritic tiles, lead plates, asphalt, limestone, trachyte rock, grass, trees, lagoon water	All All	Panchromatic IKONOS image (1 m) Synthetic Hyperion and PRISMA images (0.30 m)	Photointerpretation The same spectral unmixing procedure performed to real images	In situ observations and shape files provided by the city and lagoon portal of Venice (Italy)	The whole study area	The whole study area	Reference fractional abundance maps	Full	Spatial resampling the reference maps and evaluation of the errors Evaluation of the errors in co-localization and spatial-resampling
Cavalli [145]	MIVIS (8m)	Lateritic tiles, lead plates, vegetation, asphalt, limestone, trachyte rock	All All	Panchromatic IKONOS image (1 m) Synthetic MIVIS image (0.30 m)	Photointerpretation The same spectral unmixing procedure performed to real image	In situ observations and shape files provided by the city and lagoon portal of Venice (Italy)	The whole study area	The whole study area	Reference fractional abundance maps	Partial	Spatial resampling the reference maps and evaluation of the errors Evaluation of the errors in co-localization and spatial-resampling
Cerra et al. [104]	DESIS (30 m) HySpex (0.6–1.2 m) Sentinel-2 (10–20–60 m)	PV panels, 2 grass, 2 forest, 2 soil, 2impervious surfaces	1	Reference map	-	-	The whole study area	The whole study area	-	-	-
Cipta et al. [137]	Landsat OLI (30 m) MODIS (500 m)	Rice, non-rice	All	In situ data	-	-	10 samples	-	-	-	-
Compains Iso et al. [134]	Landsat TM, OLI (30 m)	Forest, shrubland, grassland, water, rock, bare soil	All	Orthophoto (≤0.5 m)	Photointerpretation	-	50 squares (30 × 30 m)	Random	Reference fractional abundance maps	Partial	-
Damarjati et al. [157]	PRISMA (30 m)	A. obtusifolia, sand, wetland vegetations	All	In situ data	-	-	-	-	Reference maps	-	-
Dhaini et al. [70]	AVIRIS (20 m)	Andradite, chalcedony, kaolinite, jarosite, montmorillonite, nontronite Road, trees, water, soil Asphalt, dirt, tree, roof	All	Reference map	-	-	The whole study area	The whole study area	Reference maps	-	-
Ding et al. [122]	Landsat TM, OLI (30 m)	Vegetation, impervious surface, soil	All	Google satellite images (1 m)	Photointerpretation	-	100 points	Random	Reference maps	-	-
Ding et al. [152]	MODIS (250–500 m)	Vegetation, non-vegetation	All	Landsat (30 m)	K-means unsupervised classified method	Google map	5 Landsat images	Representative areas	Reference fractional abundance maps	Partial	Spatial resampling the reference maps
Fang et al. [71]	AVIRIS (20 m)	Road, 2building, trees, grass, soil Road, trees, water, soil	All	Reference map	-	-	The whole study area	The whole study area	Reference maps	-	-
Fernández-Guisuraga et al. [161]	Sentinel-2 (10–20 m)	Soil, green vegetation, non-photosynthetic vegetation	1	Photos	-	-	60 situ plots (20 × 20 m)	Stratified random	Reference fractional abundance map	Full	-
Gu et al. [98]	AVIRIS (20 m)	Vegetation, soil, road, river soil, water, vegetation	All	Reference map	-	-	The whole study area	The whole study area	Reference maps	-	-
Guan et al. [86]	AVIRIS (20 m) HYDICE (10 m)	Trees, water, dirt, road Asphalt, grass, trees, roofs	All All	Reference map Reference map	- -	- -	The whole study area The whole study area	The whole study area The whole study area	Reference maps Reference maps	- -	- -
Hadi et al. [68]	AVIRIS (20 m) HYDICE (10 m)	Trees, water, dirt, road Asphalt, grass, trees, roofs	All All	Reference map Reference map	- -	- -	The whole study area The whole study area	The whole study area The whole study area	Reference maps Reference maps	- -	- -
Hajnal et al. [169]	Sentinel-2 (10–20–60 m)	Vegetation, impervious surface, soil	All	APEX image (2 m), High-resolution land cover map	Support vector classification	-	APEX image	Representative areas	Reference fractional abundance maps	Full	Spatial resampling the reference maps
Halbgewachs et al. [123]	Landsat TM, OLI (30 m), TIRS (60 m)	Forest, non-Forest (non-photosynthetic vegetation, soil, shade)	2	Annual classifications of the Program for Monitoring Deforestation in the Brazilian Amazon (PRODES)	-	Official truth-terrain data from deforested and non-deforested areas prepared by PRODES	494 samples	Stratified random	Reference maps	-	-

Table A1. *Cont.*

Paper	Remote Image	Determined Endmembers	Validated Endmembers	Sources of Reference Data	Method for Mapping the Endmembers	Validation of Reference Data with Other Reference Data	Sample Sizes and Number of Small Sample Sizes	Sampling Designs	Reference Data	Estimation of Fractional Abundances	Error in Co-Localization and Spatial Resampling
He et al. [56]	AMMIS (0.5 m)	Urban surface materials	All	Reference map	-	-	The whole study area	The whole study area	Reference maps	-	-
	ROSIS (4 m)	Urban surface materials	All	Reference map	-	-	The whole study area	The whole study area	Reference maps	-	-
Hong et al. [69]	AVIRIS (20 m)	Trees, water, dirt, road, roofs	All	Reference map	-	-	The whole study area	The whole study area	Reference maps	-	-
	EnMAP (30 m)	Asphalt, soil, water, vegetation	All	Reference map	-	-	The whole study area	The whole study area	Reference maps	-	-
Hu et al. [149]	MODIS (0.5–1 km)	Blue ice, coarse-grained snow, fresh snow, bare rock, deep water, slush, wet snow	1	Sentinel-2 images	The same spectral unmixing procedure performed to MODIS images	Five auxiliary datasets	Six test areas identified as blue ice areas in the Landsat-based LIMA product	Representative areas	Reference fractional abundance maps	Full	-
Hua et al. [72]	AVIRIS (10 m)	Dirt, road	All	Reference map	-	-	The whole study area	The whole study area	Reference maps	-	-
	Samson (3.2 m)	-	All	Reference map			The whole study area	The whole study area	Reference maps		
Jamshid Moghadam et al. [115]	Hyperion (30 m)	Kaolinite/smeetite, sepiolite, lizardite, chorite	All	Geological map	-	-	The whole study area	The whole study area	Reference maps	-	-
Jin et al. [143]	M3 hyperspectral image	Lunar surface materials	All	Lunar Soil Characterization Consortium dataset	-	-	-	-	Reference fractional abundance maps	Full	-
Jin et al. [73]	AVIRIS (10 m)	Road, soil, tree, water	All	Reference map	-	-	The whole study area	The whole study area	Reference maps	-	-
	Samson (3.2 m)	Water, tree, soil	All	Reference map			The whole study area	The whole study area	Reference maps		
Kremezi et al. [166]	Sentinel-2 (10–20–60 m) WorldView-2 (0.46–1.8 m) WorldView-3 (0.31–1.24–3.7 m)	PET-1.5 l bottles, LDPE bags, fishing nets	All	In situ data	-	-	3 squares (10 × 10 m)	-	Reference map	-	-
Kuester et al. [111]	HYDICE (10 m)	Urban surface materials	All	Reference map	-	-	The whole study area	The whole study area	Reference maps	-	-
Kumar et al. [113]	Hyperion (30 m)	Sal-forest, teak-plantation, scrub, grassland, water, cropland, mixed forest, urban, dry riverbed	All	Google Earth images	-	-	Same squares (30 × 30 m)	-	Reference fractional abundance maps	Partial	-
Lathrop et al. [124]	Landsat 8 OLI (15–30 m)	Mud, sandy mud, muddy sand, sand	All	In situ data	-	-	805 circles (250 m radius)	Uniform	Reference fractional abundance map	Partial	-
Legleiter et al. [103]	DESIS (30 m)	12 cyanobacteria genera, water	All	In situ data	-	-	-	-	-	-	-
Li et al. [75]	AVIRIS (10 m)	Vegetation, bare soil, vineyard, etc.	All	Field reference data	-	-	The whole study area	The whole study area	Reference maps	-	-
	Hyperion (30 m)	-	All	Hyperion (30 m) image	-	-	The whole study area	The whole study area	Reference map	-	-
Li et al. [74]	AVIRIS (10 m)	Tree, water, dirt, road	All	Reference map	-	-	The whole study area	The whole study area	Reference maps	-	-
Li et al. [107]	GaoFen-6 (2–8–16 m) Landsat 8 OLI (15–30 m) Sentinel-2 (10–20–60 m)	Green vegetation, bare rock, bare soil, non-photosynthetic vegetation	All	Photo acquired with drones	Classification	In situ measurements of fractional vegetation cover and bare rock	285 polygons	Random	Reference fractional abundance maps	Full	Polygon size
Li et al. [76]	AVIRIS (10 m)	Andradite, chalcedony, kaolinite, jarosite, montmorillonite, nontronite	All	Reference map	-	-	The whole study area	The whole study area	Reference maps	-	-
	HYDICE (10 m)	Asphalt, grass, trees, roofs	All	Reference map	-	-	The whole study area	The whole study area	Reference maps	-	-
Luo et al. [77]	AVIRIS (10 m)	Andradite, chalcedony, kaolinite, jarosite, montmorillonite, nontronite	All	Reference map	-	-	The whole study area	The whole study area	Reference maps	-	-
	HYDICE (10 m)	Asphalt, grass, trees, roofs	All	Reference map	-	-	The whole study area	The whole study area	Reference maps	-	-
Lyngdoh et al. [100]	AVIRIS (20 m) AVIRIS-NG (5 m)	Trees, water, dirt, road Red soil, black soil, crop residue, built-up areas, bituminous roads, water	All	Reference map	-	-	The whole study area	The whole study area	Reference maps	-	-
Ma & Chang [78]	AVIRIS (10 m)	-	All	Reference map	-	-	The whole study area	The whole study area	Reference maps	-	Spatial resampling the reference maps
	CASI (2.5 m)	Urban surface materials	All	Reference map	-	-	The whole study area	The whole study area	Reference maps	-	-
	ROSIS (4 m)	Urban surface materials	All	Reference map	-	-	The whole study area	The whole study area	Reference maps	-	-
Matabishi et al. [469]	DESIS (30 m)	Roof materials	All	VHR images	-	Field validation data	1053 ground reference points	-	Reference fractional abundance maps	Full	-
Meng et al. [163]	Sentinel-2 (10–20–60 m)	Vegetation, non-vegetation	1	Google Earth Pro image (1 m)	-	-	10535 squares (10 × 10 m)	Stratified random	Reference fractional abundance maps	Partial	-
Nill et al. [125]	Landsat TM, OLI (30 m)	Shrubs, coniferous trees, herbaceous plants, lichens, water, barren surfaces	All	RGB camera (0.4–8 cm) Orthophotos (10–15 cm)	-	Field validation data	216 validation pixels	Stratified random	Reference fractional abundance maps	Full	-
Ouyang et al. [126]	Landsat-8 OLI (30 m)	Impervious surface, evergreen vegetation, seasonally exposed soil	1	Land use and land cover maps (0.5 m)	-	-	264 circles (1 km radius)	Random	Reference fractional abundance map	Partial	-

Table A1. *Cont.*

Paper	Remote Image	Determined Endmembers	Validated Endmembers	Sources of Reference Data	Method for Mapping the Endmembers	Validation of Reference Data with Other Reference Data	Sample Sizes and Number of Small Sample Sizes	Sampling Designs	Reference Data	Estimation of Fractional Abundances	Error in Co-Localization and Spatial Resampling
Ozer & Leloglu [167]	Sentinel-2 (10–20–60 m)	Soil, vegetation, water	All	Aerial images (30 cm)	-	-	-	-	Reference fractional abundance map	Partial	-
P et al. [61]	ASTER (90 m)	Iron Oxide	1	In situ data	-	-	13 samples	-	-	-	-
Palsson et al. [59]	Apex	Asphalt, vegetation, water, roof	All	Reference map	-	-	The whole study area	The whole study area	Reference maps	-	-
	AVIRIS (10 m)	Road, soil, tree, water	All	Reference map	-	-	The whole study area	The whole study area	Reference maps	-	-
	CASI (2.5)	Urban surface materials	All	Reference map	-	-	The whole study area	The whole study area	Reference maps	-	-
	HYDICE (10 m)	Asphalt, grass, trees, roofs	All	Reference map	-	-	The whole study area	The whole study area	Reference maps	-	-
	Samson (3.2 m)	Soil, tree, water	All	Reference map	-	-	The whole study area	The whole study area	Reference maps	-	-
Pan & Jiang [65]	AVHRR (1–5 km)	Snow, bare land, grass, forest, shadow	All	Landsat7 TM+ image (30 m)	The same procedure performed to AVHRR image	-	Landsat image	Representative area	Reference fractional abundance maps	Full	-
Pan et al. [66]	AVHRR (1–5 km)	Snow, bare land, grass, forest, shadow	All	Landsat5 TM image (30 m)	The same procedure performed to AVHRR image	The land use/land cover	Landsat image	Representative area	Reference fractional abundance maps	Full	-
Paul et al. [470]	DESIS (30 m)	PV panel, vegetation, sand	All	VHR image	-	-	-	Random	Reference fractional abundance maps	Full	-
Pervin et al. [154]	NEON (1 m)	Tall woody plants, herbaceous and low stature vegetation, bare soil	All	NEON AOP image (0.1 m)	Supervised classification	Drone imagery (0.01 m)	13 sets of 10 pixels	Random	Reference fractional abundance maps	Partial	-
Qi et al. [89]	AVIRIS (10 m)	Road, soil, tree, water	All	Reference map	-	-	The whole study area	The whole study area	Reference maps	-	-
	HYDICE (10 m)	Asphalt, grass, trees, roofs	All	Reference map	-	-	The whole study area	The whole study area	Reference maps	-	-
	Samson (3.2 m)	Soil, tree, water	All	Reference map	-	-	The whole study area	The whole study area	Reference maps	-	-
Rajendran et al. [116]	Hyperion (30 m)	Chlorophyll-a	1	WorldView-3 image (0.31–1.24–3.7 m)		Field validation data	-	-	Reference fractional abundance maps	Full	-
Ronay et al. [170]	Specim IQ	Weed species	All	In situ data	-	-	The whole study area	The whole study area	Reference fractional abundance maps	Full	-
Santos et al. [131]	Landsat MSS, TM, OLI (30 m)	Natural vegetation, anthropized area, burned, water	All	In situ data	-	-	samples	Random	Reference maps	-	-
Shaik et al. [158]	PRISMA (30 m)	Broadleaved forest, Coniferous forest, Mixed forest, Natural grasslands, Sclerophyllous vegetation	All	Land use and land cover map	-	Field validation data	-	-	Reference maps	-	-
Shao et al. [109]	Landsat-8 OLI (15–30 m) GaoFen-1 (2–8–16 m)	Vegetation, soil impervious surfaces (high albedo; low albedo), water	1	GaoFen-1 image (2 m)	Object-based classification and photointerpretation of the results.	Ground-based measurements	300 pixels	Uniform	Reference fractional abundance map	Partial	-
Shi et al. [90]	AVIRIS (10 m)	Road, soil, tree, water	All	Reference map	-	-	The whole study area	The whole study area	Reference maps	-	-
	HYDICE (10 m)	Road, roof, soil, grass, trail, tree, water	All	Reference map	-	-	The whole study area	The whole study area	Reference maps	-	-
Shi et al. [79]	AVIRIS (10 m)	Road, soil, tree, water	All	Reference map	-	-	The whole study area	The whole study area	Reference maps	-	-
	HYDICE (10 m)	Road, roof, soil, grass, trail, tree, water	All	Reference map	-	-	The whole study area	The whole study area	Reference maps	-	-
Shimabukuro et al. [132]	Landsat TM, OLI (30 m)	Forest plantation	All	MapBiomas annual LULC map collection 6.0	-	-	20000 samples	Stratified random	Reference maps	Partial	-
Silvan-Cardenas et al. [139]	Landsat (30 m)	-	-	In situ data	-	-	samples	-	Reference maps	-	-
Sofan et al. [135]	Landsat-8 OLI (15–30 m)	Vegetation, smoldering, burnt area	All	PlanetScope images (3 m)	Photointerpretation	-	-	Random	-	-	-
Song et al. [153]	MODIS (0.5 km)	Water, urban, tree, grass	All	GlobalLand30 maps (GLC30) produced based on Landsat (30 m)	-	-	-	-	Reference fractional abundance maps	Full	-
	AVIRIS (10 m)	-	-	Reference map	-	-	The whole study area	The whole study area	Reference maps	-	-
	HYDICE (10 m)	Road, roof, soil, grass, trail, tree, water	-	Reference map	-	-	The whole study area	The whole study area	Reference maps	-	-
Sun et al. [80]	AVIRIS (10 m)	Andradite, chalcedony, kaolinite, jarosite, montmorillonite, nontronite	All	Reference map	-	-	The whole study area	The whole study area	Reference fractional abundance maps	Full	-
Sun et al. [165]	Sentinel-2 (10–20–60 m)	Rice residues, soil, green moss, white moss	1	Photos (1.5 m)	Photointerpretation	In situ observations	30 samples	Random	Reference fractional abundance maps	Partial	-

Table A1. *Cont.*

Paper	Remote Image	Determined Endmembers	Validated Endmembers	Sources of Reference Data	Method for Mapping the Endmembers	Validation of Reference Data with Other Reference Data	Sample Sizes and Number of Small Sample Sizes	Sampling Designs	Reference Data	Estimation of Fractional Abundances	Error in Co-Localization and Spatial Resampling
Sutton et al. [119]	Landsat TM, OLI (30 m)	Drylands, semi-arid zone, arid zone	All	In situ data	-	-	4207 samples	No-uniform	-	-	-
Tao et al. [91]	AVIRIS (10 m)	Andradite, chalcedony, kaolinite, jarosite, montmorillonite, nontronite	All	Reference map	-	-	The whole study area	The whole study area	Reference maps	-	-
Tarazona Coronel [127]	Landsat TM, OLI (30 m)	Vegetation	1	Landsat (15–30 m) and Sentinel-2 (10–20–60 m) images	Photointerpretation	Official truth-terrain data from deforested and non-deforested areas prepared by PRODES	300 samples	Stratified random	Reference fractional abundance maps	Partial	-
van Kuik et al. [133]	Landsat TM, OLI (30 m) Sentinel-2 (10–20–60 m)	Blowouts to sand, water, vegetation	1	Unoccupied Aerial Vehicle (UAV) orthomosaics (1 m)	Photointerpretation	-	-	-	Reference fractional abundance maps	Partial	-
Viana-Soto et al. [138]	Landsat TM, OLI (30 m)	Tree, shrub, background (herbaceous, soil, rock)	1	Orthophotos	Photointerpretation	Validation samples	-	Uniform	Reference fractional abundance maps	Full	-
Wang et al. [87]	AVIRIS (10 m)	-	-	Reference map	-	-	The whole study area	The whole study area	Reference maps	-	-
Wang et al. [142]	Landsat-8 OLI (30 m)	Impervious surfaces (high albedo, low albedo), forest, grassland, soil	1	QuickBird image (0.6 m)	Spectral angle mapping classification	In situ observations	13,080 points	Random	Reference fractional abundance maps	Partial	-
Wang et al. [150]	MODIS (0.5 km)	Vegetation, non-vegetation	All	Landsat image (30 m)	K-means-based unsupervised classification	-	Landsat image	Representative area	Reference fractional abundance maps	Partial	-
Wang et al. [92]	AVIRIS (10 m)	Andradite, chalcedony, kaolinite, jarosite, montmorillonite, nontronite	All	Reference map	-	-	The whole study area	The whole study area	Reference map	-	-
Wu & Wang [85]	AVIRIS (10 m)	Urban surface materials	All	Reference map	-	-	The whole study area	The whole study area	Reference maps	-	-
	HYDICE (10 m)	Road, roof, soil, grass, trail, tree, water	All	Reference map	-	-	The whole study area	The whole study area	Reference maps	-	-
	ROSIS (4 m)	Urban surface materials	All	Reference map	-	-	The whole study area	The whole study area	Reference maps	-	-
Xia et al. [128]	Landsat ETM+, OLI (30 m)	High albedo, vegetation low albedo, shadow	2	Google Earth images	Photointerpretation	-	100 polygons (30 × 30 m)	Random	Reference fractional abundance maps	Partial	-
Xu et al. [162]	Sentinel-2 (10–20–60 m)	Impervious surface, water body, vegetation, bare land	All	Google Earth images	Photointerpretation	In situ observations	-	-	Reference fractional abundance maps	Partial	-
Yang et al. [57]	AMMIS (0.5 m) AVIRIS ROSIS	-	All	Reference map	-	-	The whole study area	The whole study area	Reference maps	-	-
Yang [81]	AVIRIS (20 m)	Vegetation, water, soil	All	Reference map	-	-	The whole study area	The whole study area	Reference maps	-	-
	HYDICE (10 m)	Road, roof, soil, grass, trail, tree, water	All	Reference map	-	-	The whole study area	The whole study area	Reference maps	-	-
	ROSIS (4 m)	Urban surface materials	All	Reference map	-	-	The whole study area	The whole study area	Reference maps	-	-
Yang et al. [141]	Landsat-8 OLI (30 m)	Water, non-water	All	Google Earth images	-	-	The whole study area	The whole study area	Reference fractional abundance maps	Partial	-
Yi et al. [82]	AVIRIS (20 m)	Vegetation, water, soil	All	Reference map	-	-	The whole study area	The whole study area	Reference maps	-	-
	HYDICE (10 m)	Road, roof, soil, grass, trail, tree, water	All	Reference map	-	-	The whole study area	The whole study area	Reference maps	-	-
Yin et al. [82]	MODIS (0.250 km)	Water, soil	1	Landsat OLI image (30 m)	Modified normalized difference water index (MNDWI)	-	Landsat image	Representative area	Reference fractional abundance maps	Partial	Spatial resampling the reference maps
Zhang & Jiang [108]	Landsat (30 m) Sentinel-2 (20 m) MODIS (0.5 km)	Snow	1	GaoFen-2 image (3.2 m)	Supervised classification	-	-	-	Reference fractional abundance map	Partial	-
Zhang et al. [117]	HySpec (0.7 m)	Bitumen, red-painted metal sheets, blue fabric, red fabric, green fabric, grass	All	Reference map	-	-	-	-	Reference maps	Partial	-
Zhang et al. [83]	AVIRIS (20 m)	Andradite, chalcedony, kaolinite, jarosite, montmorillonite, nontronite	All	Reference map	-	-	The whole study area	The whole study area	Reference maps	-	-
Zhang et al. [93]	AVIRIS (10/20 m)	Dumortierite, muscovite, Alunite+muscovite, kaolinite, alunite, montmorillonite Tree, water, road, soil	All	Reference map	-	-	The whole study area	The whole study area	Reference maps	-	-
Zhang et al. [129]	Landsat-8 OLI (30 m)	Vegetation, impervious surfaces	All	GaoFen-1 image (2–8 m)	Photointerpretation	-	101 samples	Uniform	Reference fractional abundance maps	Partial	-
Zhang et al. [130]	Landsat-8 OLI (30 m)	Vegetation	All	GaoFen-1 image (2–8 m)	Object-based classification	-	101 samples	Uniform	Reference fractional abundance map	Partial	-

Table A1. *Cont.*

Paper	Remote Image	Determined Endmembers	Validated Endmembers	Sources of Reference Data	Method for Mapping the Endmembers	Validation of Reference Data with Other Reference Data	Sample Sizes and Number of Small Sample Sizes	Sampling Designs	Reference Data	Estimation of Fractional Abundances	Error in Co-Localization and Spatial Resampling
Zhang et al. [88]	AVIRIS (10/20 m)	Cuprite, road, trees, water, soil Asphalt, dirt, tree, roof	All	Reference map Reference map	-	-	The whole study area	The whole study area	Reference maps	-	-
Zhao et al. [84]	AVIRIS (10 m)	Road, trees, water, soil Asphalt, grass, tree, roof, metal, dirt	All	Reference map Reference map	-	-	The whole study area	The whole study area	Reference maps	-	-
Zhao et al. [96]	AVIRIS (10 m)	Road, trees, water, soil	All	Reference map	-	-	The whole study area	The whole study area	Reference maps	-	-
	HYDICE (10 m)	Road, roof, soil, grass, trail, tree, water	All	Reference map	-	-	The whole study area	The whole study area	Reference maps	-	-
Zhao et al. [94]	AVIRIS (10 m)	Road, trees, water, soil	All	Reference map	-	-	The whole study area	The whole study area	Reference maps	-	-
Zhao et al. [95]	AVIRIS (20 m)	Andradite, chalcedony, kaolinite, jarosite, montmorillonite, nontronite	All	Reference map	-	-	The whole study area	The whole study area	Reference maps	-	-
Zhao et al. [136]	Landsat-8 OLI (30 m) Sentinel-2 (10–20–60 m)	Impervious surfaces, vegetation, soil, water	2	WorldView-2 image (0.50–2 m)	-	-	172 polygons (480 × 480 m)	Random	Reference fractional abundance maps	Full	-
Zhao et al. [140]	Landsat (30 m) Spot (30 m)	Vegetation	1	Fractional vegetation cover reference maps (provided by VALERI project and the ImagineS)	-	In situ measurements of LAI (provided by VALERI project and the ImagineS)	445 squares (20 × 20 m or 30 × 30 m)	-	Reference fractional abundance map	Full	-
Zhao & Qin [168]	Sentinel-2 (10–20–60 m)	Vegetation, mineral area	All	In situ data	-	-	-	-	Reference fractional abundance maps	Partial	-
Zhu et al. [64]	AVHRR (1–5 km)	Snow, non-snow (bare land, vegetation, and water)	1	Landsat TM image (30 m)	Normalized difference snow index	-	Landsat image	Representative area	Reference fractional abundance map	Full	Spatial resolution variation
Zhu et al. [97]	AVIRIS (10 m)	Road, trees, water, soil	All	Reference map	-	-	The whole study area	The whole study area	Reference maps	-	-
	HYDICE (10 m)	Road, roof, soil, grass, trail, tree, water	All	Reference map	-	-	The whole study area	The whole study area	Reference maps	-	-
	Samson (3.2 m)	Soil, tree, water	All	Reference map	-	-	The whole study area	The whole study area	Reference maps	-	-

Table A2. Main characteristics of the eligible papers that were published in 2021.

Paper	Remote Image	Determined Endmembers	Validated Endmembers	Sources of Reference Data	Method for Mapping the Endmembers	Validation of Reference Data with Other Reference Data	Sample Sizes and Number of Small Sample Sizes	Sampling Designs	Reference Data	Estimation of Fractional Abundances	Error in Co-Localization and Spatial Resampling
Azar et al. [174]	AVIRIS CASI	Trees, Mostly Grass Ground Surface, Mixed Ground Surface, Dirt/Sand, Road	All All	Reference map CASI image	- Photointerpretation	-	The whole study area	The whole study area	Reference map Reference map	-	-
Badola et al. [226]	AVIRIS-NG (5 m) Sentinel-2 (10–20–60 m)	Black Spruce Birch Alder Gravel	All	In situ data	Photointerpretation	In situ observations	29 plots	Random	Reference map	-	-
Bai et al. [175]	AVIRIS	Asphalt, Grass, Tree, Roof, Metal, Dirt	All	Reference map	-	-	The whole study area	The whole study area	Reference map	-	-
Bair et al. [254]	Landsat MODIS	Snow, canopy	1	WorldView-2–3 images (0.34–0.55 m)	Photointerpretation	Airborne Snow Observatory (ASO) (3 m)	-	-	Reference fractional abundance map	Full	Spatial resampling the reference maps Evaluation of the errors in co-localization and spatial-resampling
Benhalouche et al. [230]	HYDICE (10 m) Samson (3.2)	Asphalt, grass, tree, roof Soil, tree, water	All	Reference map	-	-	The whole study area	The whole study area	Reference map	-	-
Benhalouche et al. [265]	PRISMA (30 m)	Mineral	All	Geological map	-	-	The whole study area	The whole study area	Reference map	-	-
Borsoi et al. [176]	AVIRIS	-	All	Reference map	-	-	The whole study area	The whole study area	Reference map	-	-
Cerra et al. [238]	HySpex	Target	All	In situ data	-	Reference targets and Aeronet data	-	-	Reference fractional abundance maps	-	-
Chang et al. [229]	GF-5 (30 m) Sentinel 2 (10–20–60 m) ZY-1-02D (30 m)	-	All	In situ data	-	-	-	-	Reference fractional abundance maps	-	-
Chen et al. [239]	Landsat	-	All	UAV images	-	Ground survey data	-	-	Reference fractional abundance maps	-	-
Chen et al. [245]	Landsat	Vegetation, impervious surface, bare soil, and water	All	Google Earth images	-	-	-	-	Reference fractional abundance maps	-	-

Table A2. *Cont.*

Paper	Remote Image	Determined Endmembers	Validated Endmembers	Sources of Reference Data	Method for Mapping the Endmembers	Validation of Reference Data with Other Reference Data	Sample Sizes and Number of Small Sample Sizes	Sampling Designs	Reference Data	Estimation of Fractional Abundances	Error in Co-Localization and Spatial Resampling
Chen et al. [246]	Landsat	-	All	Google Earth images	-	Field surveys	300 plots	Random	Reference fractional abundance maps	-	-
Converse et al. [247]	Landsat	Green vegetation, non-photosynthetic vegetation, soil	All	UAS images	-	Field surveys	Plots	-	Reference fractional abundance maps	Full	-
Di et al. [177]	AVIRIS	Cuprite	All	Reference map	-	-	The whole study area	The whole study area	Reference map	-	-
Dong & Yuan [178]	AVIRIS	-	All	Reference map	-	-	The whole study area	The whole study area	Reference map	-	-
Dong et al. [179]	AVIRIS	-	All	Reference map	-	-	The whole study area	The whole study area	Reference map	-	-
Dong et al. [180]	AVIRIS	-	All	Reference map	-	-	The whole study area	The whole study area	Reference map	-	-
Dutta et al. [248]	Landsat	Vegetation, impervious surface, bare soil,	1	In situ data	-	Built-up density, urban expansion and population density of the area	-	-	Reference fractional abundance maps	Full	-
Ekanayake et al. [181]	AVIRIS	-	All	Reference map	-	-	The whole study area	The whole study area	Reference map	-	-
Elrewainy & Sherif [182]	AVIRIS	-	All	Reference map	-	-	The whole study area	The whole study area	Reference map	-	-
Feng & Fan [255]	Landsat (30 m) Sentinel 2 (10–20–60 m)	Vegetation, high-albedo impervious surface, low-albedo impervious surface soil	All	In situ data	-	-	18000 testing areas	random	Reference fractional abundance maps	Full	-
Fernández-García et al. [256]	Landsat (30 m)	Arboreal vegetation, shrubby vegetation, herbaceous vegetation, rock and bare soil, water	All	Orthophotographs (0.25 m)	-	-	250 plots (30 × 30 m)	random	Reference fractional abundance maps	Full	Spatial resolution variation
Finger et al. [249]	Landsat (30 m)	-	All	California Department of Fish and Wildlife (CDFW) aerial survey canopy area product	-	-	-	-	Reference fractional abundance maps	Full	-
Gu et al. [183]	AVIRIS	-	All	Reference map	-	-	The whole study area	The whole study area	Reference map	-	-
Guo et al. [184]	AVIRIS	-	All	Reference map	-	-	The whole study area	The whole study area	Reference map	-	-
Gu et al. [185]	AVIRIS	-	All	Reference map	-	-	The whole study area	The whole study area	Reference map	-	-
Han et al. [186]	AVIRIS	Asphalt, grass, tree, roof	All	Reference map	-	-	The whole study area	The whole study area	Reference map	-	-
Han et al. [268]	AVIRIS	-	All	Reference map	-	-	The whole study area	The whole study area	Reference map	-	-
Haq et al. [234]	Hyperion (30 m)	Clean snow, blue ice, refreezing ice dirty snow, dirty glacier ice, firn, moraine, and glacier ice	All	In situ data	-	Sentinel-2 images	-	-	Reference fractional abundance maps	Full	-
He et al. [231]	HYDICE (10 m) MODIS (0.5–1 km)	-	All All	Reference map Finer Resolution Observation and Monitoring of Global Land Cov (30 m)	-	-	- 61 scenes	-	Reference fractional abundance maps	Full	-
He et al. [56]	ROSIS (4m)	Urban surface materials	All	Reference map	-	-	The whole study area	The whole study area	Reference map	-	-
Hua et al. [187]	AVIRIS	-	All	Reference map	-	-	The whole study area	The whole study area	Reference map	-	-
Hua et al. [188]	AVIRIS Samson (3.2)	- Soil, tree, water	All	Reference map	-	-	The whole study area	The whole study area	Reference map	-	-
Huang et al. [189]	AVIRIS	-	All	Reference map	-	-	The whole study area	The whole study area	Reference map	-	-
Jia et al. [190]	AVIRIS	Cuprite	All	Reference map	-	-	The whole study area	The whole study area	Reference map	-	-
Ji et al. [235]	Hyperion (30 m)	Photosynthetic vegetation, non-photosynthetic vegetation, bore soil	All	Reference map	-	-	The whole study area	The whole study area	Reference map	-	-
Jiji [250]	Landsat (30 m)	Heavy metals	All	In situ data	-	-	17 samples	Random	Reference fractional abundance maps	Full	-
Jin et al. [267]	ROSIS (4 m) Samson (3.2 m)	Urban surface materials Soil, tree, water	All	Reference map	-	-	The whole study area	The whole study area	Reference map	-	-
Kneib et al. [271]	Sentinel 2 (10–20–60 m)	-	all	Pleiades images (2 m)	Photointerpretation	-	-	-	Reference fractional abundance maps	Full	-
Kucuk & Yuksel [202]	AVIRIS	Cuprite	All	Reference map	-	-	The whole study area	The whole study area	Reference map	-	-
Kumar & Chakravortty [191]	AVIRIS ROSIS (4 m)	- Urban surface materials	All	Reference map	-	-	The whole study area	The whole study area	Reference map	-	-
Li et al. [203]	AVIRIS	Cuprite	All	Reference map	-	-	The whole study area	The whole study area	Reference map	-	-
Li et al. [192]	AVIRIS HYDICE (10 m)	Cuprite -	All	Reference map	-	-	The whole study area	The whole study area	Reference map	-	-
Li et al. [193]	AVIRIS		All	Reference map	-	-	The whole study area	The whole study area	Reference map	-	-
Li [194]	AVIRIS	Cuprite	All	Reference map	-	-	The whole study area	The whole study area	Reference map	-	-
Li et al. [195]	AVIRIS	Cuprite	All	Reference map	-	-	The whole study area	The whole study area	Reference map	-	-

Table A2. *Cont.*

Paper	Remote Image	Determined Endmembers	Validated Endmembers	Sources of Reference Data	Method for Mapping the Endmembers	Validation of Reference Data with Other Reference Data	Sample Sizes and Number of Small Sample Sizes	Sampling Designs	Reference Data	Estimation of Fractional Abundances	Error in Co-Localization and Spatial Resampling
Li et al. [196]	AVIRIS	Cuprite	All	Reference map	-	-	The whole study area	The whole study area	Reference map	-	-
Li et al. [197]	AVIRIS	Cuprite	All	Reference map	-	-	The whole study area	The whole study area	Reference map	-	-
Li et al. [251]	Landsat (30 m)	Impervious, vegetation, bare land, water	All	Google Earth images	-	Field surveys	4296 sampled points	Random	Reference fractional abundance maps	Full	-
Li [257]	Landsat (30 m)	Impervious, soil, vegetation	All	Images	-	-	200 sample points	Random	Reference fractional abundance maps	Full	-
Li et al. [204]	AVIRIS HYDICE (10 m)	-	All	Reference map	-	-	The whole study area	The whole study area	Reference map	-	-
Li et al. [205]	AVIRIS	Cuprite	All	Reference map	-	-	The whole study area	The whole study area	Reference map	-	-
Liu et al. [206]	AVIRIS	-	All	Reference map	-	-	The whole study area	The whole study area	Reference map	-	-
Lui & Zhu [207]	AVIRIS Samson (3.2 m)	- Soil, tree, water	All	Reference map	-	-	The whole study area	The whole study area	Reference map	-	-
Lombard & Andrieu [240]	Landsat	-	3	Google Earth images	Phointerpretation	-	8490 sample points	Random	Reference fractional abundance maps	Full	-
Luo & Chen [260]	Landsat	Vegetation, impervious, soil	1	Gaofen-2 and WorldView-2 images	-	-	-	-	Reference fractional abundance maps	Full	Spatial resolution variation
Ma et al. [276]	WorldView-3	Vegetation	All	Digital cover photography	-	Vegetation spectra	30 sample points	-	Reference fractional abundance map	Full	-
Mudereri et al. [273]	Sentinel 2 (10–20–60 m)	-	All	Google Earth images	-	Field surveys	1370 pixels	Random	Reference fractional abundance maps	Full	-
Muhuri et al. [258]	Landsat Sentinel 2 (10–20–60 m)	Snow cover	All	In situ data	-	Airborne Snow Observatory (ASO) (2 m)	-	-	Reference fractional abundance maps	Full	-
Okujeni et al. [228]	Simulated EnMAP	-	All	Google Earth images	-	Landsat images	3183 sites	Random	Reference fractional abundance maps	Full	-
Ou et al. [233]	HyMap (4.5 m)	Soil organic matter, soil heavy meta	All	In situ data	-	-	95 soil samples	Random	Reference fractional abundance maps	Full	-
Pan et al. [261]	MODIS (0.5–1 km)	Snow	All	Landsat images	MESMA	-	The whole study area	The whole study area	Reference fractional abundance maps	Full	-
Patel et al. [208]	AVIRIS	-	All	Reference map	-	-	The whole study area	The whole study area	Reference map	-	-
Peng et al. [209]	AVIRIS	-	All	Reference map	-	-	The whole study area	The whole study area	Reference map	-	-
Qin et al. [210]	AVIRIS Samson (3.2 m)	- Soil, tree, water	All	Reference map	-	-	The whole study area	The whole study area	Reference map	-	-
Racoviteanu et al. [241]	Landsat	Debris-covered glaciers	All	Pléiades 1A image (2 m) RapidEye image (5 m) PlanetScope (3 m)	Phointerpretation	DEM	151 test pixels	Random	Reference fractional abundance maps	Full	-
Rittger et al. [262]	MODIS (0.5–1 km)	Snow	All	Landsat images	-	-	-	Random	Reference fractional abundance maps	Full	Spatial resolution variation
Sall et al. [252]	Landsat (30 m)	Waterbodies	All	DigitalGlobe WorldView-2 (0.46 m)	-	National AgricultureImagery Program (NAIP)	-	-	Reference fractional abundance maps	Full	-
Sarkar & Sur [173]	ASTER (15–30–90 m)	Bauxite minerals	All	In situ data	-	Petrological, EPMA, SEM-EDS studies DEM	-	-	Reference fractional abundance maps	Full	-
Seydi & Hasanlou [236]	Hyperion (30 m)	-	All	In situ data	-	-	73505 samples	Random	Reference fractional abundance maps	Full	-
Seydi & Hasanlou [237]	Hyperion (30 m)	-	All	In situ data	-	-	-	-	Reference fractional abundance maps	Full	-
Shahid & Schizas [211]	AVIRIS Samson (3.2 m)	- Soil, tree, water	All	Reference map	-	-	The whole study area	The whole study area	Reference map	-	-
Shen et al. [242]	Landsat (30 m)	Impervious, non-impervious surface	All	Land use map by the National Basic Geographic Information Center	-	-	-	-	Reference map	-	-
Shen et al. [270]	Sentinel 2 (10–20–60 m)	-	All	Google Earth images	Phointerpretation	-	467 polygons	Random	Reference fractional abundance maps	Full	-
Shumack et al. [243]	Landsat (30 m) Sentinel 2 (10–20–60 m)	Bare soil, photosynthetic vegetation, non-photosynthetic vegetation	All	Orthorectified mosaic images (0.02 m)	Object based image analyses	SLATS dataset of fractional ground cover surveys	400 point per images	Random	Reference fractional abundance maps	Full	-
Song et al. [232]	HYDICE (10 m) Samson (3.2 m)	Road, trees, water, soil Soil, tree, water	All	Reference map	-	-	The whole study area	The whole study area	Reference map	-	-

Table A2. *Cont.*

Paper	Remote Image	Determined Endmembers	Validated Endmembers	Sources of Reference Data	Method for Mapping the Endmembers	Validation of Reference Data with Other Reference Data	Sample Sizes and Number of Small Sample Sizes	Sampling Designs	Reference Data	Estimation of Fractional Abundances	Error in Co-Localization and Spatial Resampling
Soydan et al. [272]	Sentinel 2 (10–20–60 m)	-	All	Laboratory analysis of field collected samples through Inductive Coupled Plasma	-	Laboratory analysis of field collected samples through X-Ray Diffraction, and ASD spectral analysis	-	-	Reference fractional abundance maps	Full	-
Su et al. [212]	AVIRIS HYDICE (10 m) Hyperion (30 m)	- Road, trees, water, soil	All	Reference map	-	-	The whole study area	The whole study area	Reference map	-	-
Sun et al. [263]	MODIS (0.5–1 km)	Green vegetation, sand, saline, and dark surface	All	Google Earth images Field observations	-	-	89 samples 10 plots (1 × 1 km)	Random	Reference fractional abundance maps	Full	Spatial resolution variation
Sun et al. [275]	WorldView-2	Mosses, lichens, rock, water, snow		In situ data	-	Photos and spectra	32 plots (2 × 2 m)	Random	Reference fractional abundance maps	-	-
Tan et al. [198]	AVIRIS	Cuprite	All	Reference map	-	-	The whole study area	The whole study area	Reference map	-	-
Vibhute et al. [213]	AVIRIS	Tree, soil, water, road	All	Reference map	-	-	The whole study area	The whole study area	Reference map	-	-
Wan et al. [214]	AVIRIS HYDICE (10 m) Samson (3.2 m)	- Soil, tree, water	All	Reference map	-	-	The whole study area	The whole study area	Reference map	-	-
Wang et al. [215]	AVIRIS	-	All	Reference map	-	-	The whole study area	The whole study area	Reference map	-	-
Vermeulen et al. [244]	Landsat Sentinel 2 (10–20–60 m)	Soil, Photosynthetic Vegetation, Non-Photosynthetic Vegetation	All	Images, field data	-	-	(10 × 10 m) plots	-	Reference fractional abundance maps	-	-
Wang et al. [199]	AVIRIS	-	All	Reference map	-	-	The whole study area	The whole study area	Reference map	-	-
Wang et al. [216]	AVIRIS HYDICE (10 m)	-	All	Reference map	-	-	The whole study area	The whole study area	Reference map	-	-
Wang [217]	AVIRIS ROSIS (4 m)	- Urban surface materials	All	Reference map	-	-	The whole study area	The whole study area	Reference map	-	-
Wang et al. [200]	AVIRIS ROSIS (4 m)	- Urban surface materials	All	Reference map	-	-	The whole study area	The whole study area	Reference map	-	-
Wu et al. [253]	Landsat Sentinel 2 (10–20–60 m)	Bare soil, agricultural crop Water, vegetation, urban	All	Google Maps	Phointerpretation	-	-	-	Reference fractional abundance maps	Full	-
Xiong et al. [201]	AVIRIS	-	All	Reference map	-	-	The whole study area	The whole study area	Reference map	-	-
Xiong et al. [218]	AVIRIS HYDICE (10 m)	- Road, trees, water, soil	All	Reference map	-	-	The whole study area	The whole study area	Reference map	-	-
Xu et al. [219]	AVIRIS	Cuprite	All	Reference map	-	-	The whole study area	The whole study area	Reference map	-	-
Xu & Somers [269]	Sentinel 2 (10–20–60 m)	Vegetation, soil, impervious surface	All	Google Earth images	Object-oriented classification	-	-	-	Reference fractional abundance maps	Full	-
Yang et al. [264]	MODIS (0.5–1 km)	Vegetation, soil	All	GF-1, Google Earth images	-	-	2044 samples (0.5 × 0.5 km)	Random	Reference fractional abundance maps	Full	-
Ye et al. [220]	AVIRIS	-	All	Reference map	-	-	The whole study area	The whole study area	Reference map	-	-
Yu et al. [227]	Landsat (30 m) CASI	-	All	GF-1 image (2 m) GeoEye image (2 m) Reference map	Classification	-	The whole study area	The whole study area	Reference fractional abundance maps	Partial	-
Yuan et al. [274]	UAV multispectral image	-	All	In situ data	-	-	67 samples	-	Reference fractional abundance maps	Full	-
Yuan & Dong [221]	AVIRIS	-	All	Reference map	-	-	The whole study area	The whole study area	Reference map	-	-
Yuan et al. [222]	AVIRIS	-	All	Reference map	-	-	The whole study area	The whole study area	Reference map	-	-
Zang et al. [259]	Landsat	Vegetation, soil, impervious surface	All	Google Earth Pro image		Night light data, population data at township scale, administrative data	120 samples	Random	Reference fractional abundance maps	Full	-
Zhang & Pezeril [223]	AVIRIS	-	All	Reference map	-	-	The whole study area	The whole study area	Reference map	-	-
Zhao et al. [266]	ROSIS (4 m)	Urban surface materials	All	Reference map	-	-	The whole study area	The whole study area	Reference map	-	-
Zheng et al. [224]	AVIRIS Samson (3.2 m)	- Soil, tree, water	All	Reference map	-	-	The whole study area	The whole study area	Reference map	-	-
Zhu et al. [225]	AVIRIS Samson (3.2 m)	- Soil, tree, water	All	Reference map	-	-	The whole study area	The whole study area	Reference map	-	-

Table A3. Main characteristics of the eligible papers that were published in 2020.

Paper	Remote Image	Determined Endmembers	Validated Endmembers	Sources of Reference Data	Method for Mapping the Endmembers	Validation of Reference Data with Other Reference Data	Sample Sizes and Number of Small Sample Sizes	Sampling Designs	Reference Data	Estimation of Fractional Abundances	Error in Co-Localization and Spatial Resampling
Aalstad et al. [340]	Landsat MODIS Sentinel2	Shadow, cloudy, snow, snow-free	All	305 terrestrial images	Classification	DEM	-	-	Reference fractional abundance maps	Full	-
Aldeghlawi et al. [334]	HYDICE	Urban surface materials	All	Reference maps	-	-	The whole study area	The whole study area	Reference map	-	-
Arai et al. [368]	PROBA-V	Vegetation, soil, shade	All	Landsat images (30 m)	Calculate Geometry function	Land use and land cover map produced by the MapBiomas Project and the Agricultural Census	298 sampling units	Uniform	Reference fractional abundance maps	Full	Spatial resampling the reference maps
Bai et al. [281]	AVIRIS	-	All	Reference map	-	-	The whole study area	The whole study area	Reference map	-	-
Benhalouche et al. [278]	ASTER	-	All	In situ data	-	-	2 samples	-	Reference fractional abundance maps	Full	-
Binh et al. [341]	Landsat	-	All	Google Earth images	Phointerpretation	Field surveys	-	-	Reference fractional abundance maps	Full	Evaluation of the errors in co-localization and spatial-resampling
Borsoi et al. [283]	AVIRIS	-	All	Reference map	-	-	The whole study area	The whole study area	Reference map	-	-
Borsoi et al. [282]	AVIRIS	-	All	Reference map	-	-	The whole study area	The whole study area	Reference map	-	-
Borsoi et al. [176]	AVIRIS	-	All	Reference map	-	-	The whole study area	The whole study area	Reference map	-	-
Bullock et al. [349]	Landsat	-	All	In situ data	-	-	500 samples	Random	Reference fractional abundance maps	Full	-
Carlson et al. [377]	Sentinel (10–20–60 m)	-	All	In situ data	-	Aerial photograhs	-	Random	Reference fractional abundance maps	Full	-
Chen et al. [299]	AVIRIS HYDICE	- Road, trees, water, soil	All	Reference map	-	-	The whole study area	The whole study area	Reference map	-	-
Cheng et al. [543]	Hyperspectral	-	All	In situ data	-	-	-	Random	Reference fractional abundance maps	Full	Evaluation of the errors in co-localization and spatial-resampling
Cooper et al. [330]	Simulated EnMAP (30 m)	-	All	Google Earth images	Phointerpretation	-	260 polygons (90 × 90 m)	Random	Reference fractional abundance maps	Full	-
Czekajlo et al. [350]	Landsat	-	All	Google Earth images	Phointerpretation	-	1085 grids (6 × 6 m)	Random	Reference fractional abundance maps	Full	-
Dai et al. [351]	Landsat	-	All	In situ data		DEM	2223 samples sites	Random			
Das et al. [300]	AVIRIS	-	All	Reference map	-	-	The whole study area	The whole study area	Reference map	-	-
Dou et al. [301]	AVIRIS Samson	- Soil, tree, water	All	Reference map	-	-	The whole study area	The whole study area	Reference map	-	-
Drumetz et al. [329]	CASI	-	All	Reference map	-	-	The whole study area	The whole study area	Reference map	-	-
Elkholy et al. [284]	AVIRIS Samson	- Soil, tree, water	All	Reference map	-	-	The whole study area	The whole study area	Reference map	-	-
Fang et al. [285]	AVIRIS ROSIS	- Urban surface materials	All	Reference map	-	-	The whole study area	The whole study area	Reference map	-	-
Fathy et al. [286]	AVIRIS	-	All	Reference map	-	-	The whole study area	The whole study area	Reference map	-	-
Fernández-Guisuraga et al. [342]	Landsat WorldView-2	Photosynthetic vegetation, non-photosynthetic vegetation, soil and shade	All	In situ data	-	-	85 (30 × 30 m) field plots 360 (2 × 2 m) field plots	Random	Reference fractional abundance maps	Full	Co-localization the maps
Firozjaei et al. [364]	MODIS	-	All	Landsat images	-	Annual primary energy consumption, Global gridded population density, Population size data, Normalized difference vegetation index (NDVI) Data, CO and NOx emissions	The whole study area	The whole study area	Reference fractional abundance maps	Full	-
Fraga et al. [378]	Sentinel-2 (10–20–60 m)	-	All	In situ data	-		15 sampling points	Random	Reference fractional abundance maps	Full	-
Gharbi et al. [545]	Hyperspectral	-	All	Reference map	-	-	The whole study area	The whole study area	Reference map	-	-
Girolamo-Neto et al. [379]	Sentinel-2 (10–20–60 m)	-	All	In situ data			461 field observations	Random	Reference fractional abundance maps	Full	-
Godinho Cassol et al. [369]	PROBA-V	Vegetation, soil, shade	All	Landsat images (30 m)	-	-	622 sampling units	Uniform	Reference fractional abundance maps	Full	-
Han et al. [287]	AVIRIS	-	All	Reference map	-	-	The whole study area	The whole study area	Reference map	-	-
He et al. [356]	Landsat	-	All	In situ data	-	Photos	118 field sites	Random	Reference fractional abundance maps	Full	-
Holland & Du [288]	AVIRIS	-	All	Reference map	-	-	The whole study area	The whole study area	Reference map	-	-
Hua et al. [289]	AVIRIS	-	All	Reference map	-	-	The whole study area	The whole study area	Reference map	-	-
Huang et al. [302]	AVIRIS	-	All	Reference map	-	-	The whole study area	The whole study area	Reference map	-	-

Table A3. *Cont.*

Paper	Remote Image	Determined Endmembers	Validated Endmembers	Sources of Reference Data	Method for Mapping the Endmembers	Validation of Reference Data with Other Reference Data	Sample Sizes and Number of Small Sample Sizes	Sampling Designs	Reference Data	Estimation of Fractional Abundances	Error in Co-Localization and Spatial Resampling
Huechacona-Ruiz et al. [380]	Sentinel-2 (10–20–60 m)	-	All	In situ data	-	GPS	288 sampling units	Random	Reference fractional abundance maps	Full	-
Imbiriba et al. [303]	AVIRIS Samson	- Soil, tree, water	All	Reference map	-	-	The whole study area	The whole study area	Reference map	-	-
Jarchow et al. [358]	Landsat	-	All	WorldView-2 (0.5 m)	-	National Agriculture Imagery Program (NAIP) scene	154 pods	Random	Reference fractional abundance maps	Full	-
Ji et al. [333]	GF1 Landsat Sentinel-2 (10–20–60 m)	-	All	In situ data	-	GPS	111 surveyed fractional-cover sites	Random	Reference fractional abundance maps	Full	-
Jiang et al. [304]	AVIRIS	-	All	Reference map	-	-	The whole study area	The whole study area	Reference map	-	-
Karoui et al. [290]	AVIRIS	-	All	Reference map	-	-	The whole study area	The whole study area	Reference map	-	-
Khan et al. [352]	Landsat	-	All	In situ data	-	GPS, "Land Use, Land Use Change and Forestry Projects"	108 circular sample plots	Random	Reference fractional abundance maps	Full	-
Kompella et al. [328]	AWiFS Sentienl-2 (10–20–60 m)	-	All	In situ data	-	GPS	2 sampling areas	-	Reference fractional abundance maps	Partial	Co-localization the maps
Laamrani et al. [343]	Landsat	-	All	Photographs	-	Field surveys, GPS	70 (30 × 30 m) sampling area	-	Reference fractional abundance maps	Full	Co-localization the maps
Lewińska et al. [359]	MODIS	Soil, green vegetation, non-photosynthetic vegetation shade		Land cover classifications (30 m), Map of the Natural Vegetation of Europe	-	-	The whole study area	The whole study area	Reference fractional abundance maps	Full	-
Li et al. [305]	AVIRIS Samson	- Soil, tree, water	All	Reference map	-	-	The whole study area	The whole study area	Reference map	-	-
Li [360]	Landsat	Vegetation, high albedo, low albedo, soil	All	Orthophotography images, Google Earth images	-	-	The whole study area	The whole study area	Reference fractional abundance maps	Full	-
Ling et al. [365]	MODIS	water and land	All	Radar altimetry water levels	-	-	The whole study area	The whole study area	Reference fractional abundance maps	Full	-
Liu et al. [332]	GF1 GF2 Landsat Sentinel-2 (10–20–60 m)	Water, vegetation, soil	All	Google Earth images		Meteorological data	129 sample points		Reference fractional abundance maps	Full	-
Lu et al. [306]	AVIRIS	-	All	Reference map	-	-	The whole study area	The whole study area	Reference map	-	-
Lymburner et al. [348]	Landsat	-	All	LIDAR survey	-	-	100 (10 × 10 km) tiles	Random	Reference fractional abundance maps	Full	-
Lyu et al. [338]	Hyperion (30 m)	-	All	In situ data	-	Land use data	36 plots	Random	Reference fractional abundance maps	Full	-
Markiet & Mõttus [277]	AISA Eagle II airborne hyperspectral scanner	-	-	In situ data	-	Site fertility class, tree species composition, diameter at breast height, median tree height, effective leaf area index calculated from canopy gap fraction	250 plots	Random	Reference fractional abundance maps	Full	-
Mei et al. [307]	AVIRIS HYDICE	- Road, trees, water, soil	All	Reference map	-	-	The whole study area	The whole study area	Reference map	-	-
Moghadam et al. [336]	HyMap Hyperion (30 m)	-	All	Geological map	-	-	The whole study area	The whole study area	Reference fractional abundance maps	Partial	-
Montorio et al. [339]	Landsat Sentinel-2 (10–20–60 m)	-	All	Pléiades-1A orthoimage	-	-	275/280 plots	Random	Reference fractional abundance maps	Full	-
Park et al. [546]	Hyperspectral	-	All	In situ data	-	-	-	-	Reference fractional abundance maps	Full	-
Patel et al. [372]	ROSIS	Urban surface materials	All	Reference map	-	-	The whole study area	The whole study area	Reference map	-	-
Peng et al. [297]	AVIRIS	-	All	Reference map	-	-	The whole study area	The whole study area	Reference map	-	-
Peroni Venancio et al. [347]	Landsat	photosynthetic vegetation, soil/non-photosynthetic vegetation	All	In situ data	-	-	-	Random	Reference fractional abundance maps	Full	-
Qi et al. [312]	AVIRIS	-	All	Reference map	-	-	The whole study area	The whole study area	Reference map	-	
Qi et al. [308]	AVIRIS	-	All	Reference map	-	-	The whole study area	The whole study area	Reference map	-	-
Qian et al. [309]	AVIRIS HYDICE	- Road, trees, water, soil	All	Reference map	-	-	The whole study area	The whole study area	Reference map	-	-
Qu & Bao [321]	AVIRIS HYDICE	-	All	Reference map	-	-	The whole study area	The whole study area	Reference map	-	-

Table A3. *Cont.*

Paper	Remote Image	Determined Endmembers	Validated Endmembers	Sources of Reference Data	Method for Mapping the Endmembers	Validation of Reference Data with Other Reference Data	Sample Sizes and Number of Small Sample Sizes	Sampling Designs	Reference Data	Estimation of Fractional Abundances	Error in Co-Localization and Spatial Resampling
Quintano et al. [381]	Sentinel-2 (10–20–60 m)	Char, green vegetation, non-photosynthetic vegetation, soil, shade	All	Official burn severity (three severity levels) and fire perimeter maps provided by Portuguese Study Center of Forest Fires	-	-	The whole study area	The whole study area	Reference map	-	-
Rasti et al. [320]	AVIRIS Samson	- Trees, water, soil	All	Reference map	-	-	The whole study area	The whole study area	Reference map	-	-
Redowan et al. [371]	Landsat	-	All	Google Earth images	-	-	Representative areas	Representative areas	Reference fractional abundance maps	Full	-
Rathnayake et al. [293]	AVIRIS HYDICE	- Road, trees, water, soil	All	Reference map	-	-	The whole study area	The whole study area	Reference map	-	-
Salvatore et al. [385]	WorldView-2 WorldView-3	-	All	In situ data	-	-	-	-	Reference fractional abundance maps	Full	-
Sall et al. [252]	Landsat	-	All	WorldView-2 (0.46 m)		National Agriculture Imagery Program (NAIP	89 waterbodies	The whole study area	Reference fractional abundance maps	Full	-
Salehi et al. [280]	HyMap ASTER Landsat Sentinel-2	-	All	In situ data	-	Geological map, X-ray fluorescence analysis	-	-	Reference fractional abundance maps	Full	-
Senf et al. [345]	Landsat	-	All	Aerial images	-	-	360 sample areas	Random	Reference fractional abundance maps	Full	-
Shah et al. [313]	AVIRIS	-	All	Reference map	-	-	The whole study area	The whole study area	Reference map	-	-
Shih et al. [354]	Landsat	Vegetation, Impervious, Soil	All	Google Earth VHR images	-	-	107 (90 × 90 m) samples	Random	Reference fractional abundance maps	Partial	
Shimabukuro et al. [370]	PROBA-V	-	All	Sentinel-2	-	-	Representative areas	Representative areas	Reference fractional abundance maps	Full	-
Shimabukuro et al. [353]	Landsat Suomi NPP-VIIRS ROBA-V	-	All	Sentinel-2 MODIS	-	Annual classifications of the Program for Monitoring Deforestation in the Brazilian Amazon (PRODES), Global Burned Area Products (Fire CCI, MCD45A1,MCD64A1)	-	-	Reference fractional abundance maps	Partial	-
Siebels et al. [319]	AVIRIS	-	All	Reference map	-	-	The whole study area	The whole study area	Reference map	-	-
Sing & Gray [363]	Landsat	-	All	In situ data	-	-	346 field plots	Random	Reference fractional abundance maps	Full	-
Sun et al. [331]	GF-1	-	All	Google Earth images	-	-	4500 pixels	Random	Reference fractional abundance maps	Full	-
Takodjou Wambo et al. [279]	ASTER Landsat	-	All	In situ data	-	Geological map, X-ray diffraction analysis	7 outcrops, 53 rock samples	-	Reference fractional abundance maps	Full	-
Tao et al. [315]	AVIRIS Samson	- Soil, tree, water	All	Reference map	-	-	The whole study area	The whole study area	Reference map	-	-
Thayn et al. [357]	Landsat	-	All	Low-altitude aerial imagery collected from a DJI Mavic Pro drone	-	-	Representative areas	Representative areas	Reference fractional abundance maps	Full	-
Tong et al. [311]	AVIRIS	-	All	Reference map	-	-	The whole study area	The whole study area	Reference map	-	-
Topouzelis et al. [382]	Sentinel-2 (10–20–60 m)	-	All	Unmanned Aerial System images	-	-	Representative areas	Representative areas	Reference fractional abundance maps	Full	-
Topouzelis et al. [383]	Sentinel-2 (10–20–60 m)	-	All	Unmanned Aerial System images	-	-	Representative areas	Representative areas	Reference fractional abundance maps	Full	-
Trinder & Liu [344]	Landsat	-	All	Ziyuan-3 image, Gaofen-1 satellite image,	-	-	-	-	Reference fractional abundance maps	Full	-
Uezato et al. [325]	AVIRIS	-	All	Reference map	-	-	The whole study area	The whole study area	Reference map	-	-
Vijayashekhar et al. [292]	AVIRIS HYDICE	- Road, trees, water, soil	All	Reference map	-	-	The whole study area	The whole study area	Reference map	-	-
Wang et al. [375]	Samson	Soil, tree, water	All	Reference map	-	-	The whole study area	The whole study area	Reference map	-	-
Wang et al. [366]	PlanetScope (3 m)	Green vegetation Non-photosynthetic vegetation	All	In situ data		Field measurements of LAI, phenocam-based leafless tree-crown fraction, phenocam-based leafy tree-crown fraction	no	no	Reference fractional abundance maps	Full	Expansion of the windows of field sample size

Table A3. *Cont.*

Paper	Remote Image	Determined Endmembers	Validated Endmembers	Sources of Reference Data	Method for Mapping the Endmembers	Validation of Reference Data with Other Reference Data	Sample Sizes and Number of Small Sample Sizes	Sampling Designs	Reference Data	Estimation of Fractional Abundances	Error in Co-Localization and Spatial Resampling
Wang et al. [346]	Landsat	Water, urban, agriculture, forest	All	Reference map	-	-	The whole study area	The whole study area	Reference map	-	-
Wang et al. [373]	ROSIS (4 m)	Urban surface materials	All	Reference map	-	-	The whole study area	The whole study area	Reference map	-	-
Wang et al. [322]	AVIRIS HYDICE	-	All	Reference map	-	-	The whole study area	The whole study area	Reference map	-	-
Wright & Polashenski [362]	MODIS (0.5 m)	-	All	WorldView-2 (0.46 m) WorldView-3 (0.31 m)	-		Representative areas	Representative areas	Reference fractional abundance maps	Full	-
Xiong et al. [323]	AVIRIS Samson	- Soil, tree, water	All	Reference map	-	-	The whole study area	The whole study area	Reference map	-	-
Xu et al. [295]	AVIRIS	-	All	Reference map	-	-	The whole study area	The whole study area	Reference map	-	-
Xu et al. [296]	AVIRIS	-	All	Reference map	-	-	The whole study area	The whole study area	Reference map	-	-
Xu et al. [316]	AVIRIS HYDICE	- Road, trees, water, soil	All	Reference map	-	-	The whole study area	The whole study area	Reference map	-	-
Xu et al. [318]	AVIRIS HYDICE	- Asphalt, trees, water, soil	All	Reference map	-	-	The whole study area	The whole study area	Reference map	-	-
Yang & Chen [294]	AVIRIS	-	All	Reference map	-	-	The whole study area	The whole study area	Reference map	-	-
Yang et al. [327]	AVIRIS	-	All	Reference map	-	-	The whole study area	The whole study area	Reference map	-	-
Yang et al. [298]	AVIRIS HYDICE	- Asphalt, trees, water, soil	All	Reference map	-	-	The whole study area	The whole study area	Reference map	-	-
Yang et al. [374]	Samson	Soil, tree, water	All	Reference map	-	-	The whole study area	The whole study area	Reference map	-	-
Yin et al. [355]	Landsat	-	All	Google Earth images	-	-	500 samples	Random	Reference fractional abundance maps	Full	-
Yuan et al. [314]	AVIRIS	-	All	Reference map	-	-	The whole study area	The whole study area	Reference map	-	-
Yue et al. [376]	Sentinel-2 (10–20–60 m)	-	All	Digital photos	-	-	The whole study area	The whole study area	Reference fractional abundance maps	Full	-
Zeng et al. [317]	AVIRIS	-	All	Reference map	-	-	The whole study area	The whole study area	Reference map	-	-
Zhang et al. [337]	HySpex (0.7 m)			Google Earth images	-	-	-	-	Reference fractional abundance maps	Full	-
Zhang et al. [384]	UAV hyperspectral data	-	All	In situ data	-	Laboratory analysis	35 samples	-	Reference fractional abundance maps	Full	-
Zhang et al. [326]	AVIRIS	Cuprite	All	Reference map	-	-	The whole study area	The whole study area	Reference map	-	-
Zhou et al. [310]	AVIRIS HYDICE	- Asphalt, trees, water, soil	All	Reference map	-	-	The whole study area	The whole study area	Reference map	-	-
Zhou et al. [324]	AVIRIS HYDICE Samson	- - Soil, tree, water	All	Reference map	-	-	The whole study area	The whole study area	Reference map	-	-
Zhou et al. [291]	AVIRIS (16 m) AVIRIS NG (4 m)	Turfgrass, non-photosynthetic vegetation (NPV), paved, roof, soil, and tree	All	NAIP high-resolution images (1 m)	-	-	64 regions of interest (180 × 180 m)	Random	Reference fractional abundance maps	Partial	-
Zhu et al. [335]	HYDICE	Asphalt, trees, water, soil	All	Reference map	-	-	The whole study area	The whole study area	Reference map	-	-

Table A4. Main characteristics of the eligible papers that were published in 2011.

Paper	Remote Image	Determined Endmembers	Validated Endmembers	Sources of Reference Data	Method for Mapping the Endmembers	Validation of Reference Data with Other Reference Data	Sample Sizes and Number of Small Sample Sizes	Sampling Designs	Reference Data	Estimation of Fractional Abundances	Error in Co-Localization and Spatial Resampling
Altmann et al. [404]	AVIRIS	-	All	Reference map	-	-	The whole study area	The whole study area	Reference map	-	-
Ambikapathi et al. [405]	AVIRIS	Cuprite	All	Reference map	-	-	The whole study area	The whole study area	Reference map	-	-
Bartholomeus et al. [386]	AHS	Maize	All	In situ data	-	-	14 samples	Random	Reference fractional abundance maps	Partial	-
Bouaziz et al. [420]	MODIS	-	All	In situ data	-	-	102 samples	Random	Reference fractional abundance maps	Partial	-
Canham et al. [406]	AVIRIS	Cuprite	All	Reference map	-	-	The whole study area	The whole study area	Reference map	-	-
Cao et al. [429]	HJ-1 (30 m)	-	All	In situ data	-	-	13 sample plots	Random	Reference fractional abundance maps	-	-
Castrodad et al. [392]	AVIRIS HYDICE HyMAP	- Asphalt, trees, water, soil	All	Reference map	-	-	The whole study area	The whole study area	Reference map	-	-
Chen et al. [430]	HJ-1 (30 m)	-	All	In situ data	-	-	13 sample plots	Random	Reference fractional abundance maps	-	-

Table A4. *Cont.*

Paper	Remote Image	Determined Endmembers	Validated Endmembers	Sources of Reference Data	Method for Mapping the Endmembers	Validation of Reference Data with Other Reference Data	Sample Sizes and Number of Small Sample Sizes	Sampling Designs	Reference Data	Estimation of Fractional Abundances	Error in Co-Localization and Spatial Resampling
Chudnovsky et al. [428]	Hyperion (30 m)	-	All	In situ data	-	Bulk mineral, geo-chemical composition	8 samples	-	Reference fractional abundance maps	-	-
Cui et al. [421]	MODIS (0.5–1 km)	-	All	Landsat image	-	-	Landsat image	Representative area	Reference fractional abundance maps	Partial	-
de Jong et al. [427]	HyMAP (5 m)	-	All	In situ data	-	Physical characterization, infiltration measurements	107 plots	Random	Reference fractional abundance maps	-	-
Dopido et al. [393]	AVIRIS	Cuprite	All	Reference map	-	-	The whole study area	The whole study area	Reference map	-	-
Eches et al. [407]	AVIRIS	Cuprite	All	Reference map	-	-	The whole study area	The whole study area	Reference map	-	-
Ghrefat & Goodell [387]	ASTER AVIRIS Hyperion Landsat	-	All	In situ data	-	-	-	-	Reference fractional abundance maps	-	-
Gilichinsky et al. [439]	Landsat SPOT	-	-	In situ data	-	-	229 validation areas	Random	Reference fractional abundance maps	-	-
Gillis & Plemmons [424]	HYDICE	Asphalt, trees, water, soil	All	Reference map	-	-	The whole study area	The whole study area	Reference map	-	-
Griffin et al. [431]	Landsat	-	All	In situ data	-	-	304 samples	Random	Reference fractional abundance maps	Full	-
Halimi et al. [394]	AVIRIS	-	All	Reference map	-	-	The whole study area	The whole study area	Reference map	-	-
Halimi et al. [408]	AVIRIS	-	All	Reference map	-	-	The whole study area	The whole study area	Reference map	-	-
Hamada et al. [441]	QuickBird (0.6–2.4 m) SPOT (10 m)	-	All	Infrared aerial photography (0.15 m)	Phointerpretation	-	30 samples	Random	Reference fractional abundance maps	Full	Spatial resolution variation
Heylen et al. [395]	AVIRIS	Cuprite	All	Reference map	-	-	The whole study area	The whole study area	Reference map	-	-
Heylen et al. [396]	AVIRIS	Cuprite	All	Reference map	-	-	The whole study area	The whole study area	Reference map	-	-
Heylen & Scheunders [397]	AVIRIS	Cuprite	All	Reference map	-	-	The whole study area	The whole study area	Reference map	-	-
Hosseinjani & Tangestani [388]	ASTER	-	All	In situ data	-	Geological map, X-ray diffraction analysis	8 samples	Random	Reference fractional abundance maps	Full	-
Hu & Weng [390]	ASTER	-	All	Images	-	-	Representative area	Representative area	Reference fractional abundance maps	Full	-
Iordache et al. [398]	AVIRIS	Cuprite	All	Reference map	-	-	The whole study area	The whole study area	Reference map	-	-
Iordache et al. [409]	AVIRIS	Cuprite	All	Reference map	-	-	The whole study area	The whole study area	Reference map	-	-
Ji & Feng [442]	QuickBird (2.4 m)	-	All	QuickBird (0.6 m)	-	-	The whole study area	The whole study area	Reference fractional abundance maps	Partial	-
Jiao et al. [434]	Landsat	-	All	Airborne images	-	-	Representative area	Representative area	Reference fractional abundance maps	Full	-
Kamal & Phinn [418]	CASI	-	All	Map of the mangrove speciesderived from aerial photographic interpretation at scale of 1:25,000 Provided by Queensland Herbarium/Environmental Protection Agency (EPA)	-	-	400 samples	Random	Reference fractional abundance maps	Partial	-
Knight & Voth [422]	MODIS	-	All	Landsat image	-	-	The whole study area	The whole study area	Reference fractional abundance maps	Full	-
Liu et al. [399]	AVIRIS	-	All	Reference map	-	-	The whole study area	The whole study area	Reference map	-	-
Lu et al. [435]	Landsat	High-albedo, low-albedo, vegetation, soil	All	QuickBird	Hybrid method	-	250 points	Random	Reference fractional abundance maps	Partial	Spatial resolution variation
Lu et al. [432]	Landsat	High-albedo, low-albedo, vegetation, soil	All	QuickBird	Hybrid method	-	1512 samples	Random	Reference fractional abundance maps	Partial	-
Lu et al. [423]	Landsat MODIS	Forest and non-forest Vegetation, shade and soil	All	Annual classifications of the Program for Monitoring Deforestation in the Brazilian Amazon (PRODES)	-	Official truth-terrain data from deforested and non-deforested areas prepared by PRODES	-	-	Reference fractional abundance maps	Full	-
Martin & Plaza [410]	AVIRIS	Cuprite	All	Reference map	-	-	The whole study area	The whole study area	Reference map	-	-
Martin et al. [411]	AVIRIS	Cuprite	All	Reference map	-	-	The whole study area	The whole study area	Reference map	-	-
Mei al. [307]	AVIRIS	-	All	Reference map	-	-	The whole study area	The whole study area	Reference map	-	-
Mei & He [412]	AVIRIS	Cuprite	All	Reference map	-	-	The whole study area	The whole study area	Reference map	-	-
Mianji et al. [400]	AVIRIS	-	All	Reference map	-	-	The whole study area	The whole study area	Reference map	-	-
Negrón-Juárez et al. [433]	Landsat	Photosynthetic vegetation, non-photosynthetic vegetation	All	In situ data	-	-	30 pixel	random	Reference fractional abundance maps	Partial	-
Qian et al. [425]	HYDICE	Asphalt, trees, water, soil	All	Reference map	-	-	The whole study area	The whole study area	Reference map	-	-

Table A4. *Cont.*

Paper	Remote Image	Determined Endmembers	Validated Endmembers	Sources of Reference Data	Method for Mapping the Endmembers	Validation of Reference Data with Other Reference Data	Sample Sizes and Number of Small Sample Sizes	Sampling Designs	Reference Data	Estimation of Fractional Abundances	Error in Co-Localization and Spatial Resampling
Reno et al. [436]	Landsat	Vegetation, soil, water	All	In situ data	-	Photos, botanical observations	168 ground points	-	Reference fractional abundance maps	Full	-
Sankey & Glenn [437]	Landsat	-	All	In situ data	-	-	100 plots (30 × 30 m)	Random	Reference fractional abundance maps	Full	-
Sunderman & Weisberg [438]	Landsat	-	All	In situ data	-	-	400 plots	Random	Reference fractional abundance maps	Full	-
Swatantran et al. [401]	AVIRIS	-	All	In situ data	-	Laser Vegetation Imaging Sensor	125 field plots classified based on WHR type for analysis by species/vegetation type	Random	Reference fractional abundance maps	Full	-
Vicente & de Souza Filho [389]	ASTER	-	All	In situ data	-	X-ray diffraction analysis on the same samples	42 soil samples	Random	Reference fractional abundance maps	Full	-
Villa et al. [413]	AVIRIS	-	All	Reference map	-	-	The whole study area	The whole study area	Reference map	-	-
Weng et al. [391]	ASTER	Green vegetation, soils low-albedo surfaces and high-albedo surface	All	Other ASTER images	Same procedures	-	The whole study area	The whole study area	Reference fractional abundance maps	Full	-
Xia et al. [414]	AVIRIS HYDICE	- Asphalt, trees, water, soil	All	Reference map	-	-	The whole study area	The whole study area	Reference map	-	-
Xia et al. [402]	AVIRIS	-	All	Reference map	-	-	The whole study area	The whole study area	Reference map	-	-
Yang et al. [415]	AVIRIS HYDICE	-	All	Reference map	-	-	The whole study area	The whole study area	Reference map	-	-
Youngentob et al. [426]	HyMap (3.5 m)	-	All	In situ data	-	-	99 isolated eucalypt paddock trees	Random	Reference fractional abundance maps	Full	-
Zare [403]	AVIRIS	-	All	Reference map	-	-	The whole study area	The whole study area	Reference map	-	-
Zhan et al. [416]	AVIRIS	-	All	Reference map	-	-	The whole study area	The whole study area	Reference map	-	
Zhao et al. [417]	AVIRIS	-	All	Reference map	-	-	The whole study area	The whole study area	Reference map	-	
Zurita-Milla et al. [419]	MERIS	-	All	High-spatial-resolution land-cover dataset (Dutch land-use database) (25 m)	-	-	The whole study area	The whole study area	Reference fractional abundance maps	Full	Spatial resampling the reference maps

Table A5. Main characteristics of the eligible papers that were published in 2010.

Paper	Remote Image	Determined Endmembers	Validated Endmembers	Sources of Reference Data	Method for Mapping the Endmembers	Validation of Reference Data with Other Reference Data	Sample Sizes and Number of Small Sample Sizes	Sampling Designs	Reference Data	Estimation of Fractional Abundances	Error in Co-Localization and Spatial Resampling
Alves Aguilar et al. [496]	MODIS (0.5–1 km)	Vegetation, soil	1	Landsat TM image (30 m)	NDVI	In situ observations	Landsat image	Representative area	Reference fractional abundance map	Partial	-
Biggs et al. [477]	Landsat (30 m)	Green vegetation, nonphotosynthetic vegetation, impervious surfaces, soil, shade	All	High resolution imagery	Photointerpretation	-	38 squares	Random	Reference fractional abundance maps	Full	-
Bolman [478]	Landsat (30 m)	Deciduous crowns, fully leaved crowns, shade	2	In situ data		-	17 plots	Uniform	Reference fractional abundance maps	Full	-
Borfecchia et al. [489]	Landsat (30 m)	-	-	QuickBird image (2.8 m)	Maximum Likelihood classification	Aerial photos	The whole study area	The whole study area	Reference fractional abundance maps	Full	
Castrodad et al. [471]	HYDICE	Trees, grass, road	All	Reference map	-	-	The whole study area	The whole study area	Reference maps	-	-
	HyMAP	Coniferous trees, deciduous trees, grass, water, crop, road, concrete, gravel	All	Reference map	-	-	The whole study area	The whole study area	Reference maps	-	-
Cavalli et al. [494]	MIVIS (3 m)	Vegetation, soil	1	Land cover map	-	In situ observations	-	Random	Reference maps	-	-
Chang et al. [458]	AVIRIS (20 m)	Cuprite, vegetation, soil	All	Reference map	-	-	The whole study area	The whole study area	Reference maps	-	-
	HYDICE (1.5 m)	-	-	Reference map	-	-	The whole study area	The whole study area	Reference maps	-	-
Chen et al. [475]	HJ-1 CCD (30 m)	Vegetation	All	In situ data	-	Land-use, land-cover, vegetation maps	-	-	Reference fractional abundance map	Full	-
Eches et al. [457]	AVIRIS (20 m)	Cuprite, vegetation, soil	All	Reference map	-	-	The whole study area	The whole study area	Reference maps	-	-
Eckmann et al. [496]	MODIS (0.5–1 km)	Fire	1	Band 9 of ASTER image (30 m)	-	GLC 2000 land-cover	Aster image	Representative area	Reference map	-	-
Elatawneh et al. [473]	Hyperion (30 m)	Land-cover classes	All	QuickBird image	-	In situ observations	The whole study area	The whole study area	Reference fractional abundance maps	Full	-

Table A5. *Cont.*

Paper	Remote Image	Determined Endmembers	Validated Endmembers	Sources of Reference Data	Method for Mapping the Endmembers	Validation of Reference Data with Other Reference Data	Sample Sizes and Number of Small Sample Sizes	Sampling Designs	Reference Data	Estimation of Fractional Abundances	Error in Co-Localization and Spatial Resampling
Elmore & Guin [484]	Landsat (30 m)	Vegetation, substrate, and shade	All	Aerial photographs	Photointerpretation	Land cover based on aerial photography called GIRAS	-	Random	Reference fractional abundance maps	Full	-
Estes et al. [447]	ASTER (15–30–90 m)	-	-	In situ data	-	-	127 circles (11.3 m radius)	-	Reference fractional abundance maps	Full	Change the windows of pixels
Gilichinsky et al. [492]	Landsat (30 m) SPOT (10 m)	Lichen classes	1	In situ data	-	-	229 plots	Uniform	Reference fractional abundance maps	Full	-
Golubiewski & Wessman [456]	AVIRIS (20 m)	Vegetation, soil, manmade materials	All	In situ data	-	-	-	-	Reference fractional abundance maps	-	-
He et al. [485]	Landsat (30 m)	2 vegetations, water	All	QuickBird image	Classification	-	The whole study area	The whole study area	Reference fractional abundance maps	Full	-
Hendrix et al. [464]	CASI	-	-	In situ data	-	-	The whole study area	The whole study area	Reference maps	-	-
Hu & Weng [445]	ASTER (15–30–90 m)	-	-	QuickBird image (0.61 m)	Classification	-	The whole study area	The whole study area	Reference fractional abundance maps	Full	-
Huang et al. [479]	Landsat (30 m)	Fractional vegetation cover	All	In situ data	-	-	12 polygons (45 × 30 m)	Random	Reference fractional abundance map	Full	-
Huang et al. [449]	AVIRIS (20 m)	Road, trees, lawn, path, roof, shadow	All	Reference map	-	-	The whole study area	The whole study area	Reference maps	-	-
Huck et al. [459]	AVIRIS (20 m)	Minerals	All	Reference map	-	-	The whole study area	The whole study area	Reference maps	-	-
Iordarche et al. [460]	AVIRIS (20 m)	Minerals	All	Reference map	-	-	The whole study area	The whole study area	Reference maps	-	-
Jin et al. [450]	AVIRIS (20 m) AVIRIS (20 m)	Minerals -	All	Reference map	-	-	The whole study area	The whole study area	Reference maps	-	-
Li et al. [482]	Landsat (30 m)	Low albedo, high albedo, soil, vegetation	All	In situ data	-	-	400 samples	Random	Reference fractional abundance map	Full	-
Liu et al. [491]	Landsat (30 m)	Urban, forest, water, cropland, grass, developing land	All	QuickBird image (0.61 m)	Photointerpretation	In situ observations	3000 samples	Uniform	Reference fractional abundance map	Full	-
Liu & Yue [486]	Landsat TM (30 m) SPOT (10–20 m)	Urban vegetation fraction	All	In situ data	-	-	samples	Random	Reference fractional abundance map	Full	-
Luo et al. [451]	AVIRIS (20 m)	-	-	Reference map	-	-	The whole study area	The whole study area	Reference maps	-	-
Luo et al. [452]	AVIRIS (20 m)	-	-	Reference map	-	-	The whole study area	The whole study area	Reference maps	-	-
Martin et al. [461]	AVIRIS (20 m)	Alunite, buddingtonite, calcite, kaolinite and muscovite	All	Reference map	-	-	The whole study area	The whole study area	Reference maps	-	-
Martin & Plaza [462]	AVIRIS (20 m)	Minerals	All	Reference map	-	-	The whole study area	The whole study area	Reference maps	-	-
Martin & Plaza [462]	AVIRIS (20 m)	Minerals	Field reference data	-	-	The whole of study area		Reference maps	-	-	
Mei et al. [453]	AVIRIS (20 m)	Vegetation	All	Reference map	-	-	The whole study area	The whole study area	Reference maps	-	-
Mei et al. [454]	AVIRIS (20 m)	Mineral	All	Reference map	-	-	The whole study area	The whole study area	Reference maps	-	-
Meng et al. [476]	HJ-1A/1B (30 m)	Road, vegetation, Building	All	Aerial photo	Photointerpretation Classification	-	The whole study area	The whole study area	Reference fractional abundance maps	Full	-
Meusburger et al. [497]	QuickBird (2.4 m)	Vegetations Soil	-	In situ data	-	-	43 plots (10 × 10 m)	Random	Reference fractional abundance map	Full	-
Meusburger et al. [498]	QuickBird (2.4 m)	Vegetations Soil	All	In situ data	-	-	63 samples	Random	Reference fractional abundance map	Full	-
Mezned et al. [446]	ASTER (30 m) Landsat ETM+ (15 m)	Calcite, clays, gypsum, oxyhydroxides, pyrite	All	In situ data	-	-	-	Random	Reference fractional abundance maps	Partial	-
Mucher et al. [444]	AHS (2.4 m)	Heathland vegetation	All	In situ data	-	Aerial photos	104 circles (3 m radius)	-	Reference fractional abundance maps	Full	-
Pacheco & McNairn [480]	Landsat (30 m) SPOT (20 m)	Vegetation, soil and residue	All	Digital photographs	-	Soil Landscapes of Canada Working Group, 2007	Digital images	Representative area	Reference fractional abundance maps	Full	Size and spatial resolution of the reference maps
Pascucci et al. [101]	ATM (2 m) CASI (2 m)	Soil, vegetation	All	Land cover map		In situ observations	25 samples	Random	Reference fractional abundance maps	Full	-
Plaza & Plaza [465]	DAIS (6 m)	Cork-oak trees, pasture, bare soil	All	ROSIS image (1.2 m)	Maximum-likelihood supervised classification	-	The whole study area	The whole study area	Reference fractional abundance maps	Full	Co-localization the maps
Powell & Roberts [483]	Landsat (30 m)	Vegetation, impervious soil	All	Aerial photos	-	-	41 samples	-	Reference fractional abundance maps	Full	-
Raksuntorn et al. [463]	AVIRIS (10 m) HYDICE (10 m)	Minerals -	All -	Reference map Reference map	-	-	The whole study area The whole study area	The whole study area The whole study area	Reference maps Reference maps	-	-
Ruescas et al. [448]	AVHRR (1 km)	Vegetation, burnt area, rocks, soil	All	AHS image (6 m)	Maximum likelihood classification	Statistic reports provided by the Environmental Ministry of Spain	AHS image	Representative area	Reference fractional abundance maps	Full	Evaluation of the errors in co-localization and spatial-resampling

Table A5. *Cont.*

Paper	Remote Image	Determined Endmembers	Validated Endmembers	Sources of Reference Data	Method for Mapping the Endmembers	Validation of Reference Data with Other Reference Data	Sample Sizes and Number of Small Sample Sizes	Sampling Designs	Reference Data	Estimation of Fractional Abundances	Error in Co-Localization and Spatial Resampling
Sarapirome & Kulrat [493]	Landsat (30 m)	Vegetation, impervious soil; vegetation, soil, shade	All	Air photos	-	In situ observations	-	-	Reference fractional abundance maps	Full	-
Schmidt & Witte [499]	SPOT (2.5–10 m)	Water, soil, vegetation	All	In situ data	-	-	Polygons	Random	Reference maps	-	-
Silván-Cárdenas & Wang [490]	Landsat (30 m)	Vegetations	All	AISA image (1 m)	Spectral angle mapper classification	In situ observations	300 points (30 × 30 m)	Random	Reference fractional abundance maps	Full	-
Soenen et al. [500]	SPOT (10–25 m)	Sunlit canopy, sunlit background, shadow	All	In situ data	-	-	36 plots (400 m^2)	Random	Reference fractional abundance maps	Full	The size of reference maps
Solans Vila & Barbosa [481]	Landsat (15 m)	Green vegetation, soil, shade, non-photosynthetic vegetation	All	In situ data	-	-	-	-	Reference fractional abundance maps	Full	-
Somers et al. [472]	Landsat (30 m) Hyperion (30 m)	Eucalyptus trees, soil, litter and grass	All	In situ data	-	-	46 plots	Stratified random	Reference fractional abundance map	Full	-
Tommervik et al. [487]	Landsat (30 m)	Vegetations	All	Aerial photographs and QuickBird-2 image	Photointerpretation	-	10 plots	Random	Reference fractional abundance map	Full	-
Verrelst et al. [467]	CHRIS (17 m)	Vegetation, snow	All	Aerial photographs	-	-	Aerial photographs	Representative area	Reference fractional abundance map	Full	-
Villa et al. [455]	AVIRIS (10 m) HYDICE (10 m)	- Asphalt, trees, water, soil	- -	Reference map Reference map	-	-	The whole study area The whole study area	The whole study area The whole study area	Reference maps Reference maps	-	-
Xiong et al. [470]	HYDICE (10 m)	-	-	Reference map	-	-	The whole study area	The whole study area	Reference maps	-	-
Yang & Everitt [443]	Airborne hyperspectral image (about 1.5 m)	Invasive weeds	All	In situ data	-	-	425 circular areas (diameter of 3 m)	Stratified random	Reference fractional abundance map	Full	-
Yang et al. [488]	Landsat TM (30 m)	2Vegetation, impervious surfaces (low and high albedo), soil	All	Aerial photographs	Photointerpretation	-	138 samples	Random	Reference fractional abundance maps	Full	-

Table A6. Main characteristics of the eligible papers that were published in 1996.

Paper	Remote Image	Determined Endmembers	Validated Endmembers	Sources of Reference Data	Method for Mapping the Endmembers	Validation of Reference Data with Other Reference Data	Sample Sizes and Number of Small Sample Sizes	Sampling Designs	Reference Data	Estimation of Fractional Abundances	Error in Co-Localization and Spatial Resampling
Ben-dor et al. [507]	SPOT	Mineral	All	Geological map	-	GER scanner data	The whole study area	The whole study area	Reference fractional abundance map	Partial	Co-localization the maps
Bowers & Rowan [503]	AVIRIS	Mineral	All	Geological map	-	-	The whole study area	The whole study area	Reference fractional abundance map	Partial	-
Hunt et al. [502]	AVIRIS	-	All	Landsat image	Unconstrained linear spectral unmixing	-	The whole study area	The whole study area	Reference fractional abundance map	Partial	-
Rosenthal et al. [505]	Landsat	-	All	High resolution aerial photographs	-	-	The whole study area	The whole study area	Reference fractional abundance map	Full	-
Thomas et al. [14]	Landsat	-	All	Images	Photointerpretation	-	The whole study area	The whole study area	Reference fractional abundance map	Full	-
Ustin et al. [501]	AVIRIS	-	All	Aerial photograph	-	Field based vegetation map	The whole study area	The whole study area	Reference fractional abundance map	Full	-
Van der Meer [504]	GERIS	-	All	Map	-	-	The whole study area	The whole study area	Reference fractional abundance map	Partial	-
Van der Meer [506]	Landsat	-	All	Map	-	-	The whole study area	The whole study area	Reference fractional abundance map	Partial	-

Table A7. Main characteristics of the eligible papers that were published in 1995.

Paper	Remote Image	Determined Endmembers	Validated Endmembers	Sources of Reference Data	Method for Mapping the Endmembers	Validation of Reference Data with Other Reference Data	Sample Sizes and Number of Small Sample Sizes	Sampling Designs	Reference Data	Estimation of Fractional Abundances	Error in Co-Localization and Spatial Resampling
Bianchi et al. [514]	MIVIS (4 m)	Oil, water, wood, cultivated field, smooth and grooved surface soil, rice field	1	In situ data	-	-	200 samples	Uniform	Reference fractional abundance map	Full	-
Dwyer et al. [509]	AVIRIS (20 m)	Minerals	All	Geological map	-	Remotely sensed and ground-based data	The whole study area	The whole study area	Reference maps	-	
Hall et al. [515]	MMR	Canopy, canopy plus background, background	All	In situ data	-	-	-	-	Reference fractional abundance map	Full	-
Kerdiles & Grondona [508]	AVHRR (1 km)	Vegetation, soil	All	Landsat TM image (30 m)	classification	-	-	-	Reference fractional abundance maps	Full	-
Lacaze et al. [510]	AVIRIS (20 m)	Vegetation, soil, rock	All	Landsat TM image (30 m)	classification	-	-	-	Reference fractional abundance maps	Full	-
Lavreau et al. [512]	Landsat (30 m)	Vegetation	All	Land cover map	-	-	-		Reference maps	-	-
Rowan et al. [511]	AVIRIS (20 m)	Minerals	All	Geological map	-	-	The whole study area	The whole study area	Reference maps	-	-
Van Der Meer [513]	Landsat (30 m)	Minerals	All	Geological map	-	In situ observations	The whole study area	The whole study area	Reference fractional abundance maps	Full	-

References

1. Ichoku, C.; Karnieli, A. A Review of Mixture Modeling Techniques for Sub-Pixel Land Cover Estimation. *Remote Sens. Rev.* **1996**, *13*, 161–186. [CrossRef]
2. Plaza, A.; Martinez, P.; Perez, R.; Plaza, J. A New Approach to Mixed Pixel Classification of Hyperspectral Imagery Based on Extended Morphological Profiles. *Pattern Recognit.* **2004**, *37*, 1097–1116. [CrossRef]
3. Mei, S.; Feng, D.; He, M. Hopfield Neural Network Based Mixed Pixel Unmixing for Multispectral Data. In Proceedings of the Satellite Data Compression, Communication, and Processing IV, San Diego, CA, USA, 28 August 2008; Volume 7084, pp. 88–95.
4. Borsoi, R.A.; Imbiriba, T.; Bermudez, J.C.M.; Richard, C.; Chanussot, J.; Drumetz, L.; Tourneret, J.-Y.; Zare, A.; Jutten, C. Spectral Variability in Hyperspectral Data Unmixing: A Comprehensive Review. *IEEE Geosci. Remote Sens. Mag.* **2021**, *9*, 223–270. [CrossRef]
5. Wei, J.; Wang, X. An Overview on Linear Unmixing of Hyperspectral Data. *Math. Probl. Eng.* **2020**, *2020*, 1–12. [CrossRef]
6. Keshava, N.; Mustard, J.F. Spectral Unmixing. *IEEE Signal Process. Mag.* **2002**, *19*, 44–57. [CrossRef]
7. Bioucas-Dias, J.M.; Plaza, A. Hyperspectral Unmixing: Geometrical, Statistical, and Sparse Regression-Based Approaches. In Proceedings of the Mage and Signal Processing for Remote Sensing XVI, SPIE, Toulouse, France, 7 October 2010; Bruzzone, L., Ed.; p. 78300A.
8. Heylen, R.; Parente, M.; Gader, P. A Review of Nonlinear Hyperspectral Unmixing Methods. *IEEE J. Sel. Top. Appl. Earth Obs. Remote Sens.* **2014**, *7*, 1844–1868. [CrossRef]
9. Settle, J.; Drake, N. Linear Mixing and the Estimation of Ground Cover Proportions. *Int. J. Remote Sens.* **1993**, *14*, 1159–1177. [CrossRef]
10. Borel, C.C.; Gerstl, S.A.W. Nonlinear Spectral Mixing Models for Vegetative and Soil Surfaces. *Remote Sens. Environ.* **1994**, *47*, 403–416. [CrossRef]
11. Ray, T.W.; Murray, B.C. Nonlinear Spectral Mixing in Desert Vegetation. *Remote Sens. Environ.* **1996**, *55*, 59–64. [CrossRef]
12. Johnson, P.E.; Smith, M.O.; Taylor-George, S.; Adams, J.B. A Semiempirical Method for Analysis of the Reflectance Spectra of Binary Mineral Mixtures. *J. Geophys. Res. Solid Earth* **1983**, *88*, 3557–3561. [CrossRef]
13. Smith, M.O.; Johnson, P.E.; Adams, J.B. Quantitative Determination of Mineral Types and Abundances from Reflectance Spectra Using Principal Components Analysis. *J. Geophys. Res. Solid Earth* **1985**, *90*, C797–C804. [CrossRef]
14. Thomas, G.; Hobbs, S.E.; Dufour, M. Woodland Area Estimation by Spectral Mixing: Applying a Goodness-of-Fit Solution Method. *Int. J. Remote Sens.* **1996**, *17*, 291–301. [CrossRef]
15. Goetz, A.F.H.; Boardman, J.W. Quantitative Determination of Imaging Spectrometer Specifications Based on Spectral Mixing Models. In Proceedings of the 12th Canadian Symposium on Remote Sensing Geoscience and Remote Sensing Symposium, Vancouver, BC, Canada, 10–14 July 1989; Volume 2, pp. 1036–1039.
16. Adams, J.B.; Smith, M.O.; Gillespie, A.R. Simple Models for Complex Natural Surfaces: A Strategy for The Hyperspectral Era of Remote Sensing. In Proceedings of the 12th Canadian Symposium on Remote Sensing Geoscience and Remote Sensing Symposium, Vancouver, BC, Canada, 10–14 July 1989; Volume 1, pp. 16–21.
17. Gillespie, A. Interpretation of Residual Images: Spectral Mixture Analysis of AVIRIS Images, Owens Valley, California. Jet Propulsion Laboratory. In Proceedings of the Second Airborne Visible/Infrared Imaging Spectrometer (AVIRIS) Workshop, Owens Valley, CA, USA, 4–5 June 1990; pp. 243–270.
18. Gillespie, A.R. Spectral Mixture Analysis of Multispectral Thermal Infrared Images. *Remote Sens. Environ.* **1992**, *42*, 137–145. [CrossRef]
19. Sabol, D.E.; Adams, J.B.; Smith, M.O. Quantitative Subpixel Spectral Detection of Targets in Multispectral Images. *J. Geophys. Res.* **1992**, *97*, 2659. [CrossRef]
20. Farrand, W.H.; Harsanyi, J.C. Discrimination of Poorly Exposed Lithologies in AVIRIS Data. In Proceedings of the JPL, Summaries of the 4th Annual JPL Airborne Geoscience Workshop, Washington, DC, USA, 28–29 October 1993; Volume 1. AVIRIS Workshop.
21. Adams, J.B.; Sabol, D.E.; Kapos, V.; Almeida Filho, R.; Roberts, D.A.; Smith, M.O.; Gillespie, A.R. Classification of Multispectral Images Based on Fractions of Endmembers: Application to Land-Cover Change in the Brazilian Amazon. *Remote Sens. Environ.* **1995**, *52*, 137–154. [CrossRef]
22. Tompkins, S. Optimization of Endmembers for Spectral Mixture Analysis. *Remote Sens. Environ.* **1997**, *59*, 472–489. [CrossRef]
23. Adams, J.B.; Smith, M.O.; Johnson, P.E. Spectral Mixture Modeling: A New Analysis of Rock and Soil Types at the Viking Lander 1 Site. *J. Geophys. Res.* **1986**, *91*, 8098. [CrossRef]
24. Huete, A.; Escadafal, R. Assessment of Soil-Vegetation-Senesced Materials with Spectral Mixture Modeling: Preliminary Analysis. In Proceedings of the 10th Annual International Symposium on Geoscience and Remote Sensing, College Park, MD, USA, 20–24 May 1990; pp. 1621–1624.
25. Sohn, Y.; McCoy, R.M. Mapping Desert Shrub Rangeland Using Spectral Unmixing and Modeling Spectral Mixtures with TM Data. *Photogramm. Eng. Remote Sens.* **1997**, *63*, 707–716.
26. Boardman, J.W.; Kruse, F.A.; Green, R.O. Mapping Target Signatures via Partial Unmixing of AVIRIS Data. In Proceedings of the Summaries of the Fifth Annual JPL Airborne Earth Science Workshop, Pasadena, CA, USA, 23–26 January 1995.
27. Adams, J.B.; McCord, T.B. Optical Properties of Mineral Separates, Glass, and Anorthositic Fragments from Apollo Mare Samples. In Proceedings of the Lunar and Planetary Science Conference Proceedings, Woodlands, TX, USA, 11–14 January 1971; Volume 2, p. 2183.

28. Singer, R.B.; McCord, T.B. Mars-Large Scale Mixing of Bright and Dark Surface Materials and Implications for Analysis of Spectral Reflectance. In Proceedings of the Lunar and Planetary Science Conference Proceedings, Huston, TX, USA, 19–23 March 1979; Volume 10, pp. 1835–1848.
29. Hapke, B. Bidirectional Reflectance Spectroscopy: 1. Theory. *J. Geophys. Res. Solid Earth* **1981**, *86*, 3039–3054. [CrossRef]
30. Shimabukuro, Y.; Carvalho, V.; Rudorff, B. NOAA-AVHRR Data Processing for the Mapping of Vegetation Cover. *Int. J. Remote Sens.* **1997**, *18*, 671–677. [CrossRef]
31. Shimabukuro, Y.E.; Smith, J.A. The Least-Squares Mixing Models to Generate Fraction Images Derived from Remote Sensing Multispectral Data. *IEEE Trans. Geosci. Remote Sens.* **1991**, *29*, 16–20. [CrossRef]
32. Boardman, J.W. Inversion of Imaging Spectrometry Data Using Singular Value Decomposition. In Proceedings of the 12th Canadian Symposium on Remote Sensing Geoscience and Remote Sensing Symposium, Vancouver, BC, Canada, 10–14 July 1989; Volume 4, pp. 2069–2072.
33. Heinz, D.C. Chein-I-Chang Fully Constrained Least Squares Linear Spectral Mixture Analysis Method for Material Quantification in Hyperspectral Imagery. *IEEE Trans. Geosci. Remote Sens.* **2001**, *39*, 529–545. [CrossRef]
34. Keshava, N. A Survey of Spectral Unmixing Algorithms. *Linc. Lab. J.* **2003**, 55–78.
35. Martínez, P.J.; Pérez, R.M.; Plaza, A.; Aguilar, P.L.; Cantero, M.C.; Plaza, J. Endmember Extraction Algorithms from Hyperspectral Images. *Ann. Geophys.* **2006**, *49*, 93–101. [CrossRef]
36. Veganzones, M.A.; Grana, M. Endmember Extraction Methods: A Short Review. In Proceedings of the International Conference on Knowledge-Based and Intelligent Information and Engineering Systems, Zagreb, Croatia, 3–5 September 2008; pp. 400–407.
37. Parente, M.; Plaza, A. Survey of Geometric and Statistical Unmixing Algorithms for Hyperspectral Images. In Proceedings of the 2010 2nd Workshop on Hyperspectral Image and Signal Processing: Evolution in Remote Sensing, Reykjavik, Iceland, 14–16 June 2010; pp. 1–4.
38. Bioucas-Dias, J.M.; Plaza, A. An Overview on Hyperspectral Unmixing: Geometrical, Statistical, and Sparse Regression Based Approaches. In Proceedings of the 2011 IEEE International Geoscience and Remote Sensing Symposium, Vancouver, BC, Canada, 24–29 July 2011; pp. 1135–1138.
39. Somers, B.; Asner, G.P.; Tits, L.; Coppin, P. Endmember Variability in Spectral Mixture Analysis: A Review. *Remote Sens. Environ.* **2011**, *115*, 1603–1616. [CrossRef]
40. Bioucas-Dias, J.M.; Plaza, A.; Dobigeon, N.; Parente, M.; Du, Q.; Gader, P.; Chanussot, J. Hyperspectral Unmixing Overview: Geometrical, Statistical, and Sparse Regression-Based Approaches. *IEEE J. Sel. Top. Appl. Earth Obs. Remote Sens.* **2012**, *5*, 354–379. [CrossRef]
41. Quintano, C.; Fernández-Manso, A.; Shimabukuro, Y.E.; Pereira, G. Spectral Unmixing. *Int. J. Remote Sens.* **2012**, *33*, 5307–5340. [CrossRef]
42. Ismail, M.M.B.; Bchir, O. Survey on Number of Endmembers Estimation Techniques for Hyperspectral Data Unmixing. In Proceedings of the 2014 International Conference on Audio, Language and Image Processing, Shanghai, China, 7–9 July 2014; pp. 651–655.
43. Shi, C.; Wang, L. Incorporating Spatial Information in Spectral Unmixing: A Review. *Remote Sens. Environ.* **2014**, *149*, 70–87. [CrossRef]
44. Drumetz, L.; Chanussot, J.; Jutten, C. Variability of the Endmembers in Spectral Unmixing: Recent Advances. In Proceedings of the 2016 8th Workshop on Hyperspectral Image and Signal Processing: Evolution in Remote Sensing (WHISPERS), Los Angeles, CA, USA, 21–24 August 2016; pp. 1–5.
45. Wang, L.; Shi, C.; Diao, C.; Ji, W.; Yin, D. A Survey of Methods Incorporating Spatial Information in Image Classification and Spectral Unmixing. *Int. J. Remote Sens.* **2016**, *37*, 3870–3910. [CrossRef]
46. Bassani, C.; Cavalli, R.M.; Antonelli, P. Influence of Aerosol and Surface Reflectance Variability on Hyperspectral Observed Radiance. *Atmos. Meas. Tech.* **2012**, *5*, 1193–1203. [CrossRef]
47. Abbate, G.; Cavalli, R.M.; Pascucci, S.; Pignatti, S.; Poscolieri, M. Others Relations between Morphological Settings and Vegetation Covers in a Medium Relief Landscape of Central Italy. *Ann. Geophys.* **2006**, *49*, 153–166.
48. CEOS Working Group on Calibration & Validation (WGCV). Available online: https://ceos.org/ourwork/workinggroups/wgcv/ (accessed on 22 March 2023).
49. Moher, D.; Liberati, A.; Tetzlaff, J.; Altman, D.G. The PRISMA Group Preferred Reporting Items for Systematic Reviews and Meta-Analyses: The PRISMA Statement. *PLoS Med.* **2009**, *6*, e1000097. [CrossRef]
50. Page, M.J.; McKenzie, J.E.; Bossuyt, P.M.; Boutron, I.; Hoffmann, T.C.; Mulrow, C.D.; Shamseer, L.; Tetzlaff, J.M.; Akl, E.A.; Brennan, S.E.; et al. The PRISMA 2020 Statement: An Updated Guideline for Reporting Systematic Reviews. *Int. J. Surg.* **2021**, *88*, 105906. [CrossRef]
51. Foody, G.; Cox, D. Sub-Pixel Land Cover Composition Estimation Using a Linear Mixture Model and Fuzzy Membership Functions. *Remote Sens.* **1994**, *15*, 619–631. [CrossRef]
52. Jasinski, M.F.; Eagleson, P.S. Estimation of Subpixel Vegetation Cover Using Red-Infrared Scattergrams. *IEEE Trans. Geosci. Remote Sens.* **1990**, *28*, 253–267. [CrossRef]
53. Macomber, S.A.; Woodcock, C.E. Mapping and Monitoring Conifer Mortality Using Remote Sensing in the Lake Tahoe Basin. *Remote Sens. Environ.* **1994**, *50*, 255–266. [CrossRef]

54. Marsh, Switzer, Kowalik And Lyon Resolving the Percentage of Component Terrains within Single Resolution Elements. *Photogramm. Eng. Remote Sens.* **1980**, *46*, 10791086.
55. Cen, Y.; Zhang, L.; Zhang, X.; Wang, Y.; Qi, W.; Tang, S.; Zhang, P. Aerial Hyperspectral Remote Sensing Classification Dataset of Xiongan New Area (Matiwan Village). *J. Remote Sens* **2020**, *24*, 1299–1306.
56. He, D.; Shi, Q.; Liu, X.; Zhong, Y.; Liu, X. Spectral–Spatial Fusion Sub-Pixel Mapping Based on Deep Neural Network. *IEEE Geosci. Remote Sens. Lett.* **2022**, *19*, 1–5. [CrossRef]
57. Yang, X.; Cao, W.; Lu, Y.; Zhou, Y. Hyperspectral Image Transformer Classification Networks. *IEEE Trans. Geosci. Remote Sens.* **2022**, *60*, 1–15. [CrossRef]
58. Schaepman, M.E.; Jehle, M.; Hueni, A.; D'Odorico, P.; Damm, A.; Weyermann, J.; Schneider, F.D.; Laurent, V.; Popp, C.; Seidel, F.C.; et al. Advanced Radiometry Measurements and Earth Science Applications with the Airborne Prism Experiment (APEX). *Remote Sens. Environ.* **2015**, *158*, 207–219. [CrossRef]
59. Palsson, B.; Sveinsson, J.R.; Ulfarsson, M.O. Blind Hyperspectral Unmixing Using Autoencoders: A Critical Comparison. *IEEE J. Sel. Top. Appl. Earth Obs. Remote Sens.* **2022**, *15*, 1340–1372. [CrossRef]
60. Advanced Spaceborne Thermal Emission and Reflection Radiometer (ASTER). Available online: https://terra.nasa.gov/about/terra-instruments/aster (accessed on 15 May 2023).
61. Roy, P. Detection of Iron-Bearing Mineral Assemblages in Nainarmalai Granulite Region, South India, Based on Satellite Image Processing and Geochemical Anomalies. *Environ. Monit. Assess.* **2022**, *194*, 866. [CrossRef]
62. Abay, H.H.; Legesse, D.; Venkata Suryabhagavan, K.; Atnafu, B. Mapping of Ferric (Fe^{3+}) and Ferrous (Fe^{2+}) Iron Oxides Distribution Using ASTER and Landsat 8 OLI Data, in Negash Lateritic Iron Deposit, Northern Ethiopia. *Geol. Ecol. Landsc.* **2022**, 1–18. [CrossRef]
63. Advanced Very High Resolution Radiometer (AVHRR). Available online: https://www.earthdata.nasa.gov/sensors/avhrr (accessed on 15 May 2023).
64. Zhu, J.; Cao, S.; Shang, G.; Shi, J.; Wang, X.; Zheng, Z.; Liu, C.; Yang, H.; Xie, B. Subpixel Snow Mapping Using Daily AVHRR/2 Data over Qinghai–Tibet Plateau. *Remote Sens.* **2022**, *14*, 2899. [CrossRef]
65. Pan, F.; Jiang, L. Accuracy Evaluation of Several AVHRR Fractional Snow Cover Retrieval Algorithms in Asia Water Tower Region. In Proceedings of the IGARSS 2022–2022 IEEE International Geoscience and Remote Sensing Symposium, Kuala Lumpur, Malaysia, 17–22 July 2022; pp. 3860–3863.
66. Pan, F.; Jiang, L.; Zheng, Z.; Wang, G.; Cui, H.; Zhou, X.; Huang, J. Retrieval of Fractional Snow Cover over High Mountain Asia Using 1 Km and 5 Km AVHRR/2 with Simulated Mid-Infrared Reflective Band. *Remote Sens.* **2022**, *14*, 3303. [CrossRef]
67. Airborne Visible/Infrared Imaging Spectrometer (AVIRIS). Available online: https://aviris.jpl.nasa.gov/ (accessed on 15 May 2023).
68. Hadi, F.; Yang, J.; Ullah, M.; Ahmad, I.; Farooque, G.; Xiao, L. DHCAE: Deep Hybrid Convolutional Autoencoder Approach for Robust Supervised Hyperspectral Unmixing. *Remote Sens.* **2022**, *14*, 4433. [CrossRef]
69. Hong, D.; Gao, L.; Yao, J.; Yokoya, N.; Chanussot, J.; Heiden, U.; Zhang, B. Endmember-Guided Unmixing Network (EGU-Net): A General Deep Learning Framework for Self-Supervised Hyperspectral Unmixing. *IEEE Trans. Neural Netw. Learn. Syst.* **2022**, *33*, 6518–6531. [CrossRef]
70. Dhaini, M.; Berar, M.; Honeine, P.; Van Exem, A. End-to-End Convolutional Autoencoder for Nonlinear Hyperspectral Unmixing. *Remote Sens.* **2022**, *14*, 3341. [CrossRef]
71. Fang, Y.; Wang, Y.; Xu, L.; Zhuo, R.; Wong, A.; Clausi, D.A. BCUN: Bayesian Fully Convolutional Neural Network for Hyperspectral Spectral Unmixing. *IEEE Trans. Geosci. Remote Sens.* **2022**, *60*, 1–14. [CrossRef]
72. Hua, Z.; Li, X.; Feng, Y.; Zhao, L. Dual Branch Autoencoder Network for Spectral-Spatial Hyperspectral Unmixing. *IEEE Geosci. Remote Sens. Lett.* **2022**, *19*, 1–5. [CrossRef]
73. Jin, Q.; Ma, Y.; Mei, X.; Ma, J. TANet: An Unsupervised Two-Stream Autoencoder Network for Hyperspectral Unmixing. *IEEE Trans. Geosci. Remote Sens.* **2022**, *60*, 1–15. [CrossRef]
74. Li, M.; Yang, B.; Wang, B. Robust Nonlinear Unmixing for Hyperspectral Images Based on an Extended Multilinear Mixing Model. In Proceedings of the IGARSS 2022–2022 IEEE International Geoscience and Remote Sensing Symposium, Kuala Lumpur, Malaysia, 17 July 2022; pp. 1780–1783.
75. Li, H.; Wu, K.; Xu, Y. An Integrated Change Detection Method Based on Spectral Unmixing and the CNN for Hyperspectral Imagery. *Remote Sens.* **2022**, *14*, 2523. [CrossRef]
76. Li, Z.; Altmann, Y.; Chen, J.; Mclaughlin, S.; Rahardja, S. Sparse Linear Spectral Unmixing of Hyperspectral Images Using Expectation-Propagation. *IEEE Trans. Geosci. Remote Sens.* **2022**, *60*, 1–13. [CrossRef]
77. Luo, W.; Gao, L.; Hong, D.; Chanussot, J. Endmember Purification with Affine Simplicial Cone Model. *IEEE Trans. Geosci. Remote Sens.* **2022**, *60*, 1–23. [CrossRef]
78. Ma, K.Y.; Chang, C.-I. Kernel-Based Constrained Energy Minimization for Hyperspectral Mixed Pixel Classification. *IEEE Trans. Geosci. Remote Sens.* **2022**, *60*, 1–23. [CrossRef]
79. Shi, S.; Zhao, M.; Zhang, L.; Altmann, Y.; Chen, J. Probabilistic Generative Model for Hyperspectral Unmixing Accounting for Endmember Variability. *IEEE Trans. Geosci. Remote Sens.* **2022**, *60*, 1–15. [CrossRef]
80. Sun, C.; Xing, F.; Liu, D.; Han, J.; Yang, B. Nonlinear Spectral Unmixing of Hyperspectral Imagery Based on Hapke Model and Relevance Vector Regression Algorithm. *J. Phys. Conf. Ser.* **2022**, *2219*, 012044. [CrossRef]

81. Yang, B. Supervised Nonlinear Hyperspectral Unmixing With Automatic Shadow Compensation Using Multiswarm Particle Swarm Optimization. *IEEE Trans. Geosci. Remote Sens.* **2022**, *60*, 1–18. [CrossRef]
82. Yi, C.; Liu, Y.; Zheng, L.; Gan, Y. Joint Processing of Spatial Resolution Enhancement and Spectral Unmixing for Hyperspectral Image. *IEEE Geosci. Remote Sens. Lett.* **2022**, *19*, 1–5. [CrossRef]
83. Zhang, H.; Lei, L.; Zhang, S.; Huang, M.; Li, F.; Deng, C.; Wang, S. Spatial Graph Regularized Nonnegative Matrix Factorization for Hyperspectral Unmixing. In Proceedings of the IGARSS 2022—2022 IEEE International Geoscience and Remote Sensing Symposium, Kuala Lumpur, Malaysia, 17 July 2022; pp. 1624–1627.
84. Zhao, M.; Wang, X.; Chen, J.; Chen, W. A Plug-and-Play Priors Framework for Hyperspectral Unmixing. *IEEE Trans. Geosci. Remote Sens.* **2022**, *60*, 1–13. [CrossRef]
85. Wu, Z.; Wang, B. Kernel-Based Decomposition Model with Total Variation and Sparsity Regularizations via Union Dictionary for Nonlinear Hyperspectral Anomaly Detection. *IEEE Trans. Geosci. Remote Sens.* **2022**, *60*, 1–16. [CrossRef]
86. Guan, Q.; Xu, T.; Feng, S.; Yu, F.; Song, K. Optimal Segmentation and Improved Abundance Estimation for Superpixel-Based Hyperspectral Unmixing. *Eur. J. Remote Sens.* **2022**, *55*, 485–506. [CrossRef]
87. Wang, G.; Zhang, Y.; Xie, W.-F.; Qu, Y.; Feng, L. Hyperspectral Linear Unmixing Based on Collaborative Sparsity and Multi-Band Non-Local Total Variation. *Int. J. Remote Sens.* **2022**, *43*, 1–26. [CrossRef]
88. Zhang, J.; Zhang, X.; Meng, H.; Sun, C.; Wang, L.; Cao, X. Nonlinear Unmixing via Deep Autoencoder Networks for Generalized Bilinear Model. *Remote Sens.* **2022**, *14*, 5167. [CrossRef]
89. Qi, L.; Gao, F.; Dong, J.; Gao, X.; Du, Q. SSCU-Net: Spatial–Spectral Collaborative Unmixing Network for Hyperspectral Images. *IEEE Trans. Geosci. Remote Sens.* **2022**, *60*, 1–15. [CrossRef]
90. Shi, S.; Zhang, L.; Altmann, Y.; Chen, J. Deep Generative Model for Spatial–Spectral Unmixing With Multiple Endmember Priors. *IEEE Trans. Geosci. Remote Sens.* **2022**, *60*, 1–14. [CrossRef]
91. Tao, X.; Paoletti, M.E.; Han, L.; Haut, J.M.; Ren, P.; Plaza, J.; Plaza, A. Fast Orthogonal Projection for Hyperspectral Unmixing. *IEEE Trans. Geosci. Remote Sens.* **2022**, *60*, 1–13. [CrossRef]
92. Wang, Z.; Li, J.; Liu, Y.; Xie, F.; Li, P. An Adaptive Surrogate-Assisted Endmember Extraction Framework Based on Intelligent Optimization Algorithms for Hyperspectral Remote Sensing Images. *Remote Sens.* **2022**, *14*, 892. [CrossRef]
93. Zhang, G.; Mei, S.; Xie, B.; Ma, M.; Zhang, Y.; Feng, Y.; Du, Q. Spectral Variability Augmented Sparse Unmixing of Hyperspectral Images. *IEEE Trans. Geosci. Remote Sens.* **2022**, *60*, 1–13. [CrossRef]
94. Zhao, M.; Wang, M.; Chen, J.; Rahardja, S. Perceptual Loss-Constrained Adversarial Autoencoder Networks for Hyperspectral Unmixing. *IEEE Geosci. Remote Sens. Lett.* **2022**, *19*, 1–5. [CrossRef]
95. Zhao, M.; Gao, T.; Chen, J.; Chen, W. Hyperspectral Unmixing via Nonnegative Matrix Factorization with Handcrafted and Learned Priors. *IEEE Geosci. Remote Sens. Lett.* **2022**, *19*, 1–5. [CrossRef]
96. Zhao, M.; Wang, M.; Chen, J.; Rahardja, S. Hyperspectral Unmixing for Additive Nonlinear Models With a 3-D-CNN Autoencoder Network. *IEEE Trans. Geosci. Remote Sens.* **2022**, *60*, 1–15. [CrossRef]
97. Zhu, Q.; Wang, L.; Chen, J.; Zeng, W.; Zhong, Y.; Guan, Q.; Yang, Z. S^3 TRM: Spectral-Spatial Unmixing of Hyperspectral Imagery Based on Sparse Topic Relaxation-Clustering Model. *IEEE Trans. Geosci. Remote Sens.* **2022**, *60*, 1–13. [CrossRef]
98. Gu, J.; Yang, B.; Wang, B. Nonlinear Unmixing for Hyperspectral Images via Kernel-Transformed Bilinear Mixing Models. *IEEE Trans. Geosci. Remote Sens.* **2022**, *60*, 1–13. [CrossRef]
99. Airborne Visible InfraRed Imaging Spectrometer—Next Generation (AVIRIS NG). Available online: https://www.jpl.nasa.gov/missions/airborne-visible-infrared-imaging-spectrometer-next-generation-aviris-ng (accessed on 15 May 2023).
100. Lyngdoh, R.B.; Dave, R.; Anand, S.S.; Ahmad, T.; Misra, A. Hyperspectral Unmixing with Spectral Variability Using Endmember Guided Probabilistic Generative Deep Learning. In Proceedings of the IGARSS 2022–2022 IEEE International Geoscience and Remote Sensing Symposium, Kuala Lumpur, Malaysia, 17 July 2022; pp. 1768–1771.
101. Pascucci, S.; Cavalli, R.; Palombo, A.; Pignatti, S. Suitability of CASI and ATM Airborne Remote Sensing Data for Archaeological Subsurface Structure Detection under Different Land Cover: The Arpi Case Study (Italy). *J. Geophys. Eng.* **2010**, *7*, 183–189. [CrossRef]
102. DLR Earth Sensing Imaging Spectrometer (DESIS). Available online: https://www.dlr.de/os/en/desktopdefault.aspx/tabid-12923/ (accessed on 15 May 2023).
103. Legleiter, C.J.; King, T.V.; Carpenter, K.D.; Hall, N.C.; Mumford, A.C.; Slonecker, T.; Graham, J.L.; Stengel, V.G.; Simon, N.; Rosen, B.H. Spectral Mixture Analysis for Surveillance of Harmful Algal Blooms (SMASH): A Field-, Laboratory-, and Satellite-Based Approach to Identifying Cyanobacteria Genera from Remotely Sensed Data. *Remote Sens. Environ.* **2022**, *279*, 113089. [CrossRef]
104. Cerra, D.; Ji, C.; Heiden, U. Solar Panels Area Estimation Using the Spaceborne Imaging Spectrometer Desis: Outperforming Multispectral Sensors. *ISPRS Ann. Photogramm. Remote Sens. Spat. Inf. Sci.* **2022**, *V-1–2022*, 9–14. [CrossRef]
105. EnMAP (Environmental Mapping and Analysis Program). Available online: https://www.dlr.de/eoc/en/desktopdefault.aspx/tabid-5514/20470_read-47899/ (accessed on 15 May 2023).
106. Gaofen (GF). Available online: https://space.skyrocket.de/doc_sdat/gf-6.htm (accessed on 15 May 2023).
107. Li, Y.; Sun, B.; Gao, Z.; Su, W.; Wang, B.; Yan, Z.; Gao, T. Extraction of Rocky Desertification Information in Karst Area by Using Different Multispectral Sensor Data and Multiple Endmember Spectral Mixture Analysis Method. *Front. Environ. Sci.* **2022**, *10*, 996708. [CrossRef]

108. Zhang, C.; Jiang, L. Fractional Snow Cover Mapping with High Spatiotemporal Resolution Based on Landsat, Sentinel-2 And Modis Observation. In Proceedings of the IGARSS 2022—2022 IEEE International Geoscience and Remote Sensing Symposium, Kuala Lumpur, Malaysia, 17 July 2022; pp. 3935–3938.
109. Shao, Z.; Zhang, Y.; Zhang, C.; Huang, X.; Cheng, T. Mapping Impervious Surfaces with a Hierarchical Spectral Mixture Analysis Incorporating Endmember Spatial Distribution. *Geo-Spat. Inf. Sci.* **2022**, *25*, 550–567. [CrossRef]
110. Rickard, L.J.; Basedow, R.W.; Zalewski, E.F.; Silverglate, P.R.; Landers, M. HYDICE: An Airborne System for Hyperspectral Imaging. In Proceedings of the Imaging Spectrometry of the Terrestrial Environment, SPIE, Orlando, FL, USA, 23 September 1993; Volume 1937, pp. 173–179.
111. Kuester, J.; Anastasiadis, J.; Middelmann, W.; Heizmann, M. Investigating the Influence of Hyperspectral Data Compression on Spectral Unmixing. In Proceedings of the Image and Signal Processing for Remote Sensing XXVIII, Edinburgh, UK, 26–28 September 2022; Pierdicca, N., Bruzzone, L., Bovolo, F., Eds.; SPIE: Berlin, Germany, 2022; p. 16.
112. Pearlman, J.S.; Barry, P.S.; Segal, C.C.; Shepanski, J.; Beiso, D.; Carman, S.L. Hyperion, a Space-Based Imaging Spectrometer. *IEEE Trans. Geosci. Remote Sens.* **2003**, *41*, 1160–1173. [CrossRef]
113. Kumar, V.; Pandey, K.; Panda, C.; Tiwari, V.; Agrawal, S. Assessment of Different Spectral Unmixing Techniques on Space Borne Hyperspectral Imagery. *Remote Sens. Earth Syst. Sci.* **2022**, 5. [CrossRef]
114. Cavalli, R.M. The Weight of Hyperion and PRISMA Hyperspectral Sensor Characteristics on Image Capability to Retrieve Urban Surface Materials in the City of Venice. *Sensors* **2023**, *23*, 454. [CrossRef] [PubMed]
115. Jamshid Moghadam, H.; Mohammady Oskouei, M.; Nouri, T. The Influence of Noise Intensity in the Nonlinear Spectral Unmixing of Hyperspectral Data. *PFG J. Photogramm. Remote Sens. Geoinf. Sci.* **2022**, *91*, 21–42. [CrossRef]
116. Rajendran, S.; Al-Naimi, N.; Al Khayat, J.A.; Sorino, C.F.; Sadooni, F.N.; Al Saad Al Kuwari, H. Chlorophyll-a Concentrations in the Arabian Gulf Waters of Arid Region: A Case Study from the Northern Coast of Qatar. *Reg. Stud. Mar. Sci.* **2022**, *56*, 102680. [CrossRef]
117. Zhang, G.; Scheunders, P.; Cerra, D.; Muller, R. Shadow-Aware Nonlinear Spectral Unmixing for Hyperspectral Imagery. *IEEE J. Sel. Top. Appl. Earth Obs. Remote Sens.* **2022**, *15*, 5514–5533. [CrossRef]
118. Landsat Satellite Missions. Available online: https://www.usgs.gov/landsat-missions/landsat-satellite-missions (accessed on 15 May 2023).
119. Sutton, A.; Fisher, A.; Metternicht, G. Assessing the Accuracy of Landsat Vegetation Fractional Cover for Monitoring Australian Drylands. *Remote Sens.* **2022**, *14*, 6322. [CrossRef]
120. Bera, D.; Kumar, P.; Siddiqui, A.; Majumdar, A. Assessing Impact of Urbanisation on Surface Runoff Using Vegetation-Impervious Surface-Soil (VIS) Fraction and NRCS Curve Number (CN) Model. *Model. Earth Syst. Environ.* **2022**, *8*, 309–322. [CrossRef]
121. Brice, E.M.; Halabisky, M.; Ray, A.M. Making the Leap from Ponds to Landscapes: Integrating Field-Based Monitoring of Amphibians and Wetlands with Satellite Observations. *Ecol. Indic.* **2022**, *135*, 108559. [CrossRef]
122. Ding, Q.; Pan, T.; Lin, T.; Zhang, C. Urban Land-Cover Changes in Major Cities in China from 1990 to 2015. *Int. J. Environ. Res. Public Health* **2022**, *19*, 16079. [CrossRef]
123. Halbgewachs, M.; Wegmann, M.; da Ponte, E. A Spectral Mixture Analysis and Landscape Metrics Based Framework for Monitoring Spatiotemporal Forest Cover Changes: A Case Study in Mato Grosso, Brazil. *Remote Sens.* **2022**, *14*, 1907. [CrossRef]
124. Lathrop, R.G.; Merchant, D.; Niles, L.; Paludo, D.; Santos, C.D.; Larrain, C.E.; Feigin, S.; Smith, J.; Dey, A. Multi-Sensor Remote Sensing of Intertidal Flat Habitats for Migratory Shorebird Conservation. *Remote Sens.* **2022**, *14*, 5016. [CrossRef]
125. Nill, L.; Grünberg, I.; Ullmann, T.; Gessner, M.; Boike, J.; Hostert, P. Arctic Shrub Expansion Revealed by Landsat-Derived Multitemporal Vegetation Cover Fractions in the Western Canadian Arctic. *Remote Sens. Environ.* **2022**, *281*, 113228. [CrossRef]
126. Ouyang, L.; Wu, C.; Li, J.; Liu, Y.; Wang, M.; Han, J.; Song, C.; Yu, Q.; Haase, D. Mapping Impervious Surface Using Phenology-Integrated and Fisher Transformed Linear Spectral Mixture Analysis. *Remote Sens.* **2022**, *14*, 1673. [CrossRef]
127. Tarazona Coronel, Y. Mapping Deforestation Using Fractions Indices and the Non-Seasonal PVts-β Detection Approach. *IEEE Geosci. Remote Sens. Lett.* **2022**, *19*, 1–5. [CrossRef]
128. Xia, Z.; Li, Y.; Zhang, W.; Chen, R.; Guo, S.; Zhang, P.; Du, P. Solar Photovoltaic Program Helps Turn Deserts Green in China: Evidence from Satellite Monitoring. *J. Environ. Manag.* **2022**, *324*, 116338. [CrossRef]
129. Zhang, Y.; Wang, Y.; Ding, N.; Yang, X. Spatial Pattern Impact of Impervious Surface Density on Urban Heat Island Effect: A Case Study in Xuzhou, China. *Land* **2022**, *11*, 2135. [CrossRef]
130. Zhang, Y.; Wang, Y.; Ding, N. Spatial Effects of Landscape Patterns of Urban Patches with Different Vegetation Fractions on Urban Thermal Environment. *Remote Sens.* **2022**, *14*, 5684. [CrossRef]
131. Santos, F.C.; da Silva Pinto Vieira, R.M.; Barbosa, A.A.; da Cruz Ferreira, Y.; Polizel, S.P.; Sestini, M.F.; Ometto, J.P.H.B. Application of Remote Sensing to Analyze the Loss of Natural Vegetation in the Jalapão Mosaic (Brazil) before and after the Creation of Protected Area (1970–2018). *Environ. Monit. Assess.* **2022**, *194*, 201. [CrossRef]
132. Shimabukuro, Y.E.; Arai, E.; da Silva, G.M.; Dutra, A.C.; Mataveli, G.; Duarte, V.; Martini, P.R.; Cassol, H.L.G.; Ferreira, D.S.; Junqueira, L.R. Mapping and Monitoring Forest Plantations in São Paulo State, Southeast Brazil, Using Fraction Images Derived from Multiannual Landsat Sensor Images. *Forests* **2022**, *13*, 1716. [CrossRef]
133. van Kuik, N.; de Vries, J.; Schwarz, C.; Ruessink, G. Surface-Area Development of Foredune Trough Blowouts and Associated Parabolic Dunes Quantified from Time Series of Satellite Imagery. *Aeolian Res.* **2022**, *57*, 100812. [CrossRef]

134. Compains Iso, L.; Fernández-Manso, A.; Fernández-García, V. Optimizing Spectral Libraries from Landsat Imagery for the Analysis of Habitat Richness Using MESMA. *Forests* **2022**, *13*, 1824. [CrossRef]
135. Sofan, P.; Chulafak, G.A.; Pambudi, A.I.; Yulianto, F. Assessment of Space-Based Tropical Smouldering Peatlands: Mixed Pixel Analysis. *IOP Conf. Ser. Earth Environ. Sci.* **2022**, *1109*, 012054. [CrossRef]
136. Zhao, Y.; Zhang, X.; Feng, W.; Xu, J. Deep Learning Classification by ResNet-18 Based on the Real Spectral Dataset from Multispectral Remote Sensing Images. *Remote Sens.* **2022**, *14*, 4883. [CrossRef]
137. Cipta, I.M.; Jaelani, L.M.; Sanjaya, H. Identification of Paddy Varieties from Landsat 8 Satellite Image Data Using Spectral Unmixing Method in Indramayu Regency, Indonesia. *ISPRS Int. J. Geo-Inf.* **2022**, *11*, 510. [CrossRef]
138. Viana-Soto, A.; Okujeni, A.; Pflugmacher, D.; García, M.; Aguado, I.; Hostert, P. Quantifying Post-Fire Shifts in Woody-Vegetation Cover Composition in Mediterranean Pine Forests Using Landsat Time Series and Regression-Based Unmixing. *Remote Sens. Environ.* **2022**, *281*, 113239. [CrossRef]
139. Silvan-Cardenas, J.L.; Wang, L. Fully Constrained Linear Spectral Unmixing: Analytic Solution Using Fuzzy Sets. *IEEE Trans. Geosci. Remote Sens.* **2010**, *48*, 3992–4002. [CrossRef]
140. Zhao, J.; Li, J.; Liu, Q.; Zhang, Z.; Dong, Y. Comparative Study of Fractional Vegetation Cover Estimation Methods Based on Fine Spatial Resolution Images for Three Vegetation Types. *IEEE Geosci. Remote Sens. Lett.* **2022**, *19*, 1–5. [CrossRef]
141. Yang, X.; Chu, Q.; Wang, L.; Yu, M. Water Body Super-Resolution Mapping Based on Multiple Endmember Spectral Mixture Analysis and Multiscale Spatio-Temporal Dependence. *Remote Sens.* **2022**, *14*, 2050. [CrossRef]
142. Wang, J.; Zhao, Y.; Fu, Y.; Xia, L.; Chen, J. Improving LSMA for Impervious Surface Estimation in an Urban Area. *Eur. J. Remote Sens.* **2022**, *55*, 37–51. [CrossRef]
143. Jin, M.; Ding, X.; Han, H.; Pang, J.; Wang, Y. An Improved Method Combining Fisher Transformation and Multiple Endmember Spectral Mixture Analysis for Lunar Mineral Abundance Quantification Using Spectral Data. *Icarus* **2022**, *380*, 115008. [CrossRef]
144. Bassani, C.; Cavalli, M.; Palombo, A.; Pignatti, S.; Madonna, F. Laboratory Activity for a New Procedure of MIVIS Calibration and Relative Validation with Test Dataa. *Ann. Geophys.* **2006**, *49*, 45–56.
145. Cavalli, R.M. Spatial Validation of Spectral Unmixing Results: A Case Study of Venice City. *Remote Sens.* **2022**, *14*, 5165. [CrossRef]
146. Medium Resolution Imaging Spectrometer (MERIS). Available online: https://earth.esa.int/eogateway/instruments/meris (accessed on 15 May 2023).
147. Ambarwulan, W.; Salama, M.S.; Verhoef, W.; Mannaerts, C.M. The Estimation of Total Suspended Matter from Satellite Imagery of Tropical Coastal Water Berau Estuary, Indonesia. *IOP Conf. Ser. Earth Environ. Sci.* **2022**, *950*, 012089. [CrossRef]
148. MODIS (Moderate Resolution Imaging Spectroradiomete. Available online: https://modis.gsfc.nasa.gov/about/ (accessed on 15 May 2023).
149. Hu, Z.; Kuipers Munneke, P.; Lhermitte, S.; Dirscherl, M.; Ji, C.; van den Broeke, M. FABIAN: A Daily Product of Fractional Austral-Summer Blue Ice over ANtarctica during 2000–2021 Based on MODIS Imagery Using Google Earth Engine. *Remote Sens. Environ.* **2022**, *280*, 113202. [CrossRef]
150. Wang, Q.; Ding, X.; Tong, X.; Atkinson, P.M. Real-Time Spatiotemporal Spectral Unmixing of MODIS Images. *IEEE Trans. Geosci. Remote Sens.* **2022**, *60*, 1–16. [CrossRef]
151. Yin, Z.; Ling, F.; Li, X.; Cai, X.; Chi, H.; Li, X.; Wang, L.; Zhang, Y.; Du, Y. A Cascaded Spectral–Spatial CNN Model for Super-Resolution River Mapping with MODIS Imagery. *IEEE Trans. Geosci. Remote Sens.* **2022**, *60*, 1–13. [CrossRef]
152. Ding, X.; Wang, Q.; Tong, X. Integrating 250 m MODIS Data in Spectral Unmixing for 500 m Fractional Vegetation Cover Estimation. *Int. J. Appl. Earth Obs. Geoinf.* **2022**, *111*, 102860. [CrossRef]
153. Song, M.; Zhong, Y.; Ma, A.; Xu, X.; Zhang, L. A Joint Spectral Unmixing and Subpixel Mapping Framework Based on Multiobjective Optimization. *IEEE Trans. Geosci. Remote Sens.* **2022**, *60*, 1–17. [CrossRef]
154. Pervin, R.; Robeson, S.M.; MacBean, N. Fusion of Airborne Hyperspectral and LiDAR Canopy-Height Data for Estimating Fractional Cover of Tall Woody Plants, Herbaceous Vegetation, and Other Soil Cover Types in a Semi-Arid Savanna Ecosystem. *Int. J. Remote Sens.* **2022**, *43*, 3890–3926. [CrossRef]
155. PRISMA (Hyperspectral Precursor of the Application Mission). Available online: https://www.asi.it/en/earth-science/prisma/ (accessed on 15 May 2023).
156. Benhalouche, F.Z.; Benabbou, O.; Karoui, M.S.; Kebir, L.W.; Bennia, A.; Deville, Y. Minerals Detection and Mapping in the Southwestern Algeria Gara-Djebilet Region with a Multistage Informed NMF-Based Unmixing Approach Using Prisma Remote Sensing Hyperspectral Data. In Proceedings of the IGARSS 2022—2022 IEEE International Geoscience and Remote Sensing Symposium, Kuala Lumpur, Malaysia, 17 July 2022; pp. 6422–6425.
157. Damarjati, S.; Nugraha, W.A.; Arjasakusuma, S. Mapping the Invasive Palm Species *Arenga Obtusifolia* Using Multiple Endmember Spectral Mixture Analysis (MESMA) and PRISMA Hyperspectral Data in Ujung Kulon National Park, Indonesia. *Geocarto Int.* **2022**, 1–21. [CrossRef]
158. Shaik, R.U.; Laneve, G.; Fusilli, L. An Automatic Procedure for Forest Fire Fuel Mapping Using Hyperspectral (PRISMA) Imagery: A Semi-Supervised Classification Approach. *Remote Sens.* **2022**, *14*, 1264. [CrossRef]
159. Bigdeli, B.; Samadzadegan, F.; Reinartz, P. A Multiple SVM System for Classification of Hyperspectral Remote Sensing Data. *J. Indian Soc. Remote Sens.* **2013**, *41*, 763–776. [CrossRef]
160. SENTINEL-2. Available online: https://sentinel.esa.int/web/sentinel/missions/sentinel-2 (accessed on 15 May 2023).

161. Fernández-Guisuraga, J.M.; Suárez-Seoane, S.; Quintano, C.; Fernández-Manso, A.; Calvo, L. Comparison of Physical-Based Models to Measure Forest Resilience to Fire as a Function of Burn Severity. *Remote Sens.* **2022**, *14*, 5138. [CrossRef]
162. Xu, Y.; Jiang, C.; Li, X.; Ji, E.; Ban, S. Research on the Extraction Method of Impervious Surface in Nanjing Based on Random Forest Classification. In Proceedings of the 2022 29th International Conference on Geoinformatics, Beijing, China, 15–18 August 2022; pp. 1–10.
163. Meng, R.; Xu, B.; Zhao, F.; Dong, Y.; Wang, C.; Sun, R.; Zhou, Y.; Zhou, L.; Gong, S.; Zhang, D. Characterizing the Provision and Inequality of Primary School Greenspaces in China's Major Cities Based on Multi-Sensor Remote Sensing. *Urban For. Urban Green.* **2022**, *75*, 127670. [CrossRef]
164. Cao, S.; Feng, J.; Hu, Z.; Li, Q.; Wu, G. Improving Estimation of Urban Land Cover Fractions with Rigorous Spatial Endmember Modeling. *ISPRS J. Photogramm. Remote Sens.* **2022**, *189*, 36–49. [CrossRef]
165. Sun, Z.; Zhu, Q.; Deng, S.; Li, X.; Hu, X.; Chen, R.; Shao, G.; Yang, H.; Yang, G. Estimation of Crop Residue Cover in Rice Paddies by a Dynamic-Quadripartite Pixel Model Based on Sentinel-2A Data. *Int. J. Appl. Earth Obs. Geoinf.* **2022**, *106*, 102645. [CrossRef]
166. Kremezi, M.; Kristollari, V.; Karathanassi, V.; Topouzelis, K.; Kolokoussis, P.; Taggio, N.; Aiello, A.; Ceriola, G.; Barbone, E.; Corradi, P. Increasing the Sentinel-2 Potential for Marine Plastic Litter Monitoring through Image Fusion Techniques. *Mar. Pollut. Bull.* **2022**, *182*, 113974. [CrossRef]
167. Ozer, E.; Leloglu, U.M. Wetland Spectral Unmixing Using Multispectral Satellite Images. *Geocarto Int.* **2022**, 1–24. [CrossRef]
168. Zhao, S.; Qin, Q. Detection and Identification of Surface Cover in Coalbed Methane Enrichment Area Based on Spectral Unmixing. In Proceedings of the IGARSS 2022—2022 IEEE International Geoscience and Remote Sensing Symposium, Kuala Lumpur, Malaysia, 17 July 2022; pp. 3732–3735.
169. Hajnal, W.; Priem, F.; Canters, F. M-CORE: A Novel Approach for Land Cover Fraction Mapping Using Multisite Spectral Libraries. *IEEE Trans. Geosci. Remote Sens.* **2022**, *60*, 1–15. [CrossRef]
170. Ronay, I.; Kizel, F.; Lati, R. The effect of spectral mixtures on weed species classification. *ISPRS Ann. Photogramm. Remote Sens. Spat. Inf. Sci.* **2022**, *V-3–2022*, 477–484. [CrossRef]
171. Satellite Pour l'Observation de La Terre (SPOT). Available online: https://earth.esa.int/eogateway/missions/spot (accessed on 15 May 2023).
172. WorldView. Available online: https://earth.esa.int/eogateway/missions/worldview (accessed on 15 May 2023).
173. Sarkar, D.; Sur, P. Targeting the Bauxite Rich Pockets from Lateritic Terrain Utilizing ASTER Data: A Case Study from Kabirdham District, Chhattisgarh, India. *J. Earth Syst. Sci.* **2021**, *130*, 189. [CrossRef]
174. Ghanbari Azar, S.; Meshgini, S.; Beheshti, S.; Yousefi Rezaii, T. Linear Mixing Model with Scaled Bundle Dictionary for Hyperspectral Unmixing with Spectral Variability. *Signal Process.* **2021**, *188*, 108214. [CrossRef]
175. Bai, J.; Feng, R.; Wang, L.; Zhong, Y.; Zhang, L. Weakly Supervised Convolutional Neural Networks for Hyperspectral Unmixing. In Proceedings of the 2021 IEEE International Geoscience and Remote Sensing Symposium IGARSS, Brussels, Belgium, 11 July 2021; pp. 3857–3860.
176. Borsoi, R.A.; Imbiriba, T.; Bermudez, J.C.M.; Richard, C. Deep Generative Models for Library Augmentation in Multiple Endmember Spectral Mixture Analysis. *IEEE Geosci. Remote Sens. Lett.* **2021**, *18*, 1831–1835. [CrossRef]
177. Di, W.-C.; Huang, J.; Wang, J.-J.; Huang, T.-Z. Enhancing Reweighted Low-Rank Representation for Hyperspectral Image Unmixing. In Proceedings of the 2021 IEEE International Geoscience and Remote Sensing Symposium IGARSSk, Brussels, Belgium, 11 July 2021; pp. 3825–3828.
178. Dong, L.; Yuan, Y. Sparse Constrained Low Tensor Rank Representation Framework for Hyperspectral Unmixing. *Remote Sens. Remote Sens.* **2021**, *13*, 1473. [CrossRef]
179. Dong, L.; Yuan, Y.; Lu, X. Spectral–Spatial Joint Sparse NMF for Hyperspectral Unmixing. *IEEE Trans. Geosci. Remote Sens.* **2021**, *59*, 2391–2402. [CrossRef]
180. Dong, L.; Lu, X.; Liu, G.; Yuan, Y. A Novel NMF Guided for Hyperspectral Unmixing From Incomplete and Noisy Data. *IEEE Trans. Geosci. Remote Sens.* **2022**, *60*, 1–15. [CrossRef]
181. Ekanayake, E.M.M.B.; Weerasooriya, H.M.H.K.; Ranasinghe, D.Y.L.; Herath, S.; Rathnayake, B.; Godaliyadda, G.M.R.I.; Ekanayake, M.P.B.; Herath, H.M.V.R. Constrained Nonnegative Matrix Factorization for Blind Hyperspectral Unmixing Incorporating Endmember Independence. *IEEE J. Sel. Top. Appl. Earth Obs. Remote Sens.* **2021**, *14*, 11853–11869. [CrossRef]
182. Elrewainy, A.; Sherif, S. Robust Anomaly Detection Algorithm for Hyperspectral Images Using Spectral Unmixing. In *Proceedings of the Image and Signal Processing for Remote Sensing XXVII*; Bruzzone, L., Bovolo, F., Benediktsson, J.A., Eds.; SPIE: Bellingham, DC, USA, 2021; p. 38.
183. Gu, J.; Cheng, T.; Wang, B. Reweighted Kernel-Based Nonlinear Hyperspectral Unmixing With Regional ℓ_1-Norm Regularization. *IEEE Geosci. Remote Sens. Lett.* **2022**, *19*, 1–5. [CrossRef]
184. Guo, Z.; Min, A.; Yang, B.; Chen, J.; Li, H.; Gao, J. A Sparse Oblique-Manifold Nonnegative Matrix Factorization for Hyperspectral Unmixing. *IEEE Trans. Geosci. Remote Sens.* **2022**, *60*, 1–13. [CrossRef]
185. Guo, Z.; Min, A.; Yang, B.; Chen, J.; Li, H. A Modified Huber Nonnegative Matrix Factorization Algorithm for Hyperspectral Unmixing. *IEEE J. Sel. Top. Appl. Earth Obs. Remote Sens.* **2021**, *14*, 5559–5571. [CrossRef]
186. Han, Z.; Hong, D.; Gao, L.; Zhang, B.; Chanussot, J. Deep Half-Siamese Networks for Hyperspectral Unmixing. *IEEE Geosci. Remote Sens. Lett.* **2021**, *18*, 1996–2000. [CrossRef]

187. Hua, Z.; Li, X.; Qiu, Q.; Zhao, L. Autoencoder Network for Hyperspectral Unmixing With Adaptive Abundance Smoothing. *IEEE Geosci. Remote Sens. Lett.* **2021**, *18*, 1640–1644. [CrossRef]
188. Hua, Z.; Li, X.; Jiang, J.; Zhao, L. Gated Autoencoder Network for Spectral–Spatial Hyperspectral Unmixing. *Remote Sens.* **2021**, *13*, 3147. [CrossRef]
189. Huang, J.; Di, W.-C.; Wang, J.-J.; Lin, J.; Huang, T.-Z. Bilateral Joint-Sparse Regression for Hyperspectral Unmixing. *IEEE J. Sel. Top. Appl. Earth Obs. Remote Sens.* **2021**, *14*, 10147–10161. [CrossRef]
190. Jia, P.; Zhang, M.; Shen, Y. Deep Spectral Unmixing Framework via 3D Denoising Convolutional Autoencoder. *IET Image Process.* **2021**, *15*, 1399–1409. [CrossRef]
191. Kumar, P.; Chakravortty, S. Generation of Sub-Pixel-Level Maps for Mixed Pixels in Hyperspectral Image Data. *Curr. Sci.* **2021**, *120*, 166. [CrossRef]
192. Li, C.; Jiang, Y.; Chen, X. Hyperspectral Unmixing via Noise-Free Model. *IEEE Trans. Geosci. Remote Sens.* **2021**, *59*, 3277–3291. [CrossRef]
193. Li, C.; Gu, Y.; Chen, X.; Zhang, Y.; Ruan, L. Hyperspectral Unmixing via Latent Multiheterogeneous Subspace. *IEEE Trans. Geosci. Remote Sens.* **2021**, *59*, 563–577. [CrossRef]
194. Li, F. Low-Rank and Spectral-Spatial Sparse Unmixing for Hyperspectral Remote Sensing Imagery. *Wirel. Commun. Mob. Comput.* **2021**, *2021*, 1–14. [CrossRef]
195. Li, F.; Zhang, S.; Liang, B.; Deng, C.; Xu, C.; Wang, S. Hyperspectral Sparse Unmixing With Spectral-Spatial Low-Rank Constraint. *IEEE J. Sel. Top. Appl. Earth Obs. Remote Sens.* **2021**, *14*, 6119–6130. [CrossRef]
196. Li, F.; Zhang, S.; Deng, C.; Liang, B.; Cao, J.; Wang, S. Robust Double Spatial Regularization Sparse Hyperspectral Unmixing. *IEEE J. Sel. Top. Appl. Earth Obs. Remote Sens.* **2021**, *14*, 12569–12582. [CrossRef]
197. Li, H.; Borsoi, R.A.; Imbiriba, T.; Closas, P.; Bermudez, J.C.M.; Erdogmus, D. Model-Based Deep Autoencoder Networks for Nonlinear Hyperspectral Unmixing. *IEEE Geosci. Remote Sens. Lett.* **2022**, *19*, 1–5. [CrossRef]
198. Tan, X.; Yu, Q.; Wang, Z.; Zhu, J. Semi-Supervised Unmixing of Hyperspectral Data via Spectral-Spatial Factorization. *IEEE Sens. J.* **2021**, *21*, 25963–25972. [CrossRef]
199. Wang, J.-J.; Huang, T.-Z.; Huang, J.; Deng, L.-J. A Two-Step Iterative Algorithm for Sparse Hyperspectral Unmixing via Total Variation. *Appl. Math. Comput.* **2021**, *401*, 126059. [CrossRef]
200. Wang, L.; Wang, S.; Jia, X.; Bi, T. A Novel Hyperspectral Unmixing Method Based on Least Squares Twin Support Vector Machines. *Eur. J. Remote Sens.* **2021**, *54*, 72–85. [CrossRef]
201. Xiong, F.; Zhou, J.; Ye, M.; Lu, J.; Qian, Y. NMF-SAE: An Interpretable Sparse Autoencoder for Hyperspectral Unmixing. In Proceedings of the ICASSP 2021—2021 IEEE International Conference on Acoustics, Speech and Signal Processing (ICASSP), Toronto, ON, Canada, 6 June 2021; pp. 1865–1869.
202. Kucuk, S.; Yuksel, S.E. Total Utility Metric Based Dictionary Pruning for Sparse Hyperspectral Unmixing. *IEEE Trans. Comput. Imaging* **2021**, *7*, 562–572. [CrossRef]
203. Li, C.; Chen, X.; Jiang, Y.; Yang, L. Elastic Constraints on Split Hierarchical Abundances for Blind Hyperspectral Unmixing. *Signal Process.* **2021**, *188*, 108229. [CrossRef]
204. Li, X.; Huang, R.; Zhao, L. Correntropy-Based Spatial-Spectral Robust Sparsity-Regularized Hyperspectral Unmixing. *IEEE Trans. Geosci. Remote Sens.* **2021**, *59*, 1453–1471. [CrossRef]
205. Li, Y.; Bao, W.; Qu, K.; Shen, X. Nonlocal Weighted Sparse Unmixing Based on Global Search and Parallel Optimization. *J. Appl. Rem. Sens.* **2021**, *15*. [CrossRef]
206. Liu, J.; Zhang, Y.; Liu, Y.; Mu, C. Hyperspectral Images Unmixing Based on Abundance Constrained Multi-Layer KNMF. *IEEE Access* **2021**, *9*, 91080–91090. [CrossRef]
207. Liu, R.; Zhu, X. Endmember Bundle Extraction Based on Multiobjective Optimization. *IEEE Trans. Geosci. Remote Sens.* **2021**, *59*, 8630–8645. [CrossRef]
208. Patel, J.R.; Joshi, M.V.; Bhatt, J.S. Spectral Unmixing Using Autoencoder with Spatial and Spectral Regularizations. In Proceedings of the 2021 IEEE International Geoscience and Remote Sensing Symposium IGARSS, Brussels, Belgium, 11 July 2021; pp. 3321–3324.
209. Peng, J.; Zhou, Y.; Sun, W.; Du, Q.; Xia, L. Self-Paced Nonnegative Matrix Factorization for Hyperspectral Unmixing. *IEEE Trans. Geosci. Remote Sens.* **2021**, *59*, 1501–1515. [CrossRef]
210. Qin, J.; Lee, H.; Chi, J.T.; Drumetz, L.; Chanussot, J.; Lou, Y.; Bertozzi, A.L. Blind Hyperspectral Unmixing Based on Graph Total Variation Regularization. *IEEE Trans. Geosci. Remote Sens.* **2021**, *59*, 3338–3351. [CrossRef]
211. Shahid, K.T.; Schizas, I.D. Unsupervised Hyperspectral Unmixing via Nonlinear Autoencoders. *IEEE Trans. Geosci. Remote Sens.* **2022**, *60*, 1–13. [CrossRef]
212. Su, Y.; Xu, X.; Li, J.; Qi, H.; Gamba, P.; Plaza, A. Deep Autoencoders With Multitask Learning for Bilinear Hyperspectral Unmixing. *IEEE Trans. Geosci. Remote Sens.* **2021**, *59*, 8615–8629. [CrossRef]
213. Vibhute, A.D.; Gaikwad, S.V.; Kale, K.V.; Mane, A.V. Hyperspectral Image Unmixing for Land Cover Classification. In Proceedings of the 2021 IEEE India Council International Subsections Conference (INDISCON), Nagpur, India, 27 August 2021; pp. 1–5.
214. Wan, L.; Chen, T.; Plaza, A.; Cai, H. Hyperspectral Unmixing Based on Spectral and Sparse Deep Convolutional Neural Networks. *IEEE J. Sel. Top. Appl. Earth Obs. Remote Sens.* **2021**, *14*, 11669–11682. [CrossRef]

215. Wang, J.-J.; Wang, D.-C.; Huang, T.-Z.; Huang, J. Endmember Constraint Non-Negative Tensor Factorization Via Total Variation for Hyperspectral Unmixing. In Proceedings of the 2021 IEEE International Geoscience and Remote Sensing Symposium IGARSS, Brussels, Belgium, 11 July 2021; pp. 3313–3316.
216. Wang, J.-J.; Wang, D.-C.; Huang, T.-Z.; Huang, J.; Zhao, X.-L.; Deng, L.-J. Endmember Independence Constrained Hyperspectral Unmixing via Nonnegative Tensor Factorization. *Knowl. Based Syst.* **2021**, *216*, 106657. [CrossRef]
217. Wang, J. A Novel Collaborative Representation Algorithm for Spectral Unmixing of Hyperspectral Remotely Sensed Imagery. *IEEE Access* **2021**, *9*, 89243–89248. [CrossRef]
218. Xiong, F.; Zhou, J.; Tao, S.; Lu, J.; Qian, Y. SNMF-Net: Learning a Deep Alternating Neural Network for Hyperspectral Unmixing. *IEEE Trans. Geosci. Remote Sens.* **2022**, *60*, 1–16. [CrossRef]
219. Xu, C.; Wu, Z.; Li, F.; Zhang, S.; Deng, C.; Wang, Y. Spectral-Spatial Joint Sparsity Unmixing of Hyperspectral Images Based on Framelet Transform. *Infrared Phys. Technol.* **2021**, *112*, 103564. [CrossRef]
220. Ye, C.; Liu, S.; Xu, M.; Du, B.; Wan, J.; Sheng, H. An Endmember Bundle Extraction Method Based on Multiscale Sampling to Address Spectral Variability for Hyperspectral Unmixing. *Remote Sens.* **2021**, *13*, 3941. [CrossRef]
221. Yuan, Y.; Dong, L. Weighted Sparsity Constraint Tensor Factorization for Hyperspectral Unmixing. In Proceedings of the 2021 IEEE International Geoscience and Remote Sensing Symposium IGARSS, Brussels, Belgium, 11 July 2021; pp. 3333–3336.
222. Yuan, Y.; Dong, L.; Li, X. Hyperspectral Unmixing Using Nonlocal Similarity-Regularized Low-Rank Tensor Factorization. *IEEE Trans. Geosci. Remote Sens.* **2022**, *60*, 1–14. [CrossRef]
223. Zhang, M.; Pezeril, S. A Comparative Study of Recent Multi-Component Unmixing Algorithms. In Proceedings of the 2021 11th Workshop on Hyperspectral Imaging and Signal Processing: Evolution in Remote Sensing (WHISPERS), Amsterdam, The Netherlands, 24 March 2021; pp. 1–5.
224. Zheng, P.; Su, H.; Du, Q. Sparse and Low-Rank Constrained Tensor Factorization for Hyperspectral Image Unmixing. *IEEE J. Sel. Top. Appl. Earth Obs. Remote Sens.* **2021**, *14*, 1754–1767. [CrossRef]
225. Zhu, Q.; Wang, L.; Zeng, W.; Guan, Q.; Hu, Z. A Sparse Topic Relaxion and Group Clustering Model for Hyperspectral Unmixing. *IEEE J. Sel. Top. Appl. Earth Obs. Remote Sens.* **2021**, *14*, 4014–4027. [CrossRef]
226. Badola, A.; Panda, S.K.; Roberts, D.A.; Waigl, C.F.; Bhatt, U.S.; Smith, C.W.; Jandt, R.R. Hyperspectral Data Simulation (Sentinel-2 to AVIRIS-NG) for Improved Wildfire Fuel Mapping, Boreal Alaska. *Remote Sens.* **2021**, *13*, 1693. [CrossRef]
227. Yu, J.; Wang, B.; Lin, Y.; Li, F.; Cai, J. A Novel Inequality-Constrained Weighted Linear Mixture Model for Endmember Variability. *Remote Sens. Environ.* **2021**, *257*, 112359. [CrossRef]
228. Okujeni, A.; Jänicke, C.; Cooper, S.; Frantz, D.; Hostert, P.; Clark, M.; Segl, K.; Van Der Linden, S. Multi-Season Unmixing of Vegetation Class Fractions across Diverse Californian Ecoregions Using Simulated Spaceborne Imaging Spectroscopy Data. *Remote Sens. Environ.* **2021**, *264*, 112558. [CrossRef]
229. Chang, M.; Meng, X.; Sun, W.; Yang, G.; Peng, J. Collaborative Coupled Hyperspectral Unmixing Based Subpixel Change Detection for Analyzing Coastal Wetlands. *IEEE J. Sel. Top. Appl. Earth Obs. Remote Sens.* **2021**, *14*, 8208–8224. [CrossRef]
230. Benhalouche, F.Z.; Deville, Y.; Karoui, M.S.; Ouamri, A. Hyperspectral Unmixing Based on Constrained Bilinear or Linear-Quadratic Matrix Factorization. *Remote Sens.* **2021**, *13*, 2132. [CrossRef]
231. He, D.; Zhong, Y.; Wang, X.; Zhang, L. Deep Convolutional Neural Network Framework for Subpixel Mapping. *IEEE Trans. Geosci. Remote Sens.* **2021**, *59*, 9518–9539. [CrossRef]
232. Song, H.; Wu, X.; Zou, A.; Liu, Y.; Zou, Y. Weighted Total Variation Regularized Blind Unmixing for Hyperspectral Image. *IEEE Geosci. Remote Sens. Lett.* **2022**, *19*, 1–5. [CrossRef]
233. Ou, D.; Tan, K.; Lai, J.; Jia, X.; Wang, X.; Chen, Y.; Li, J. Semi-Supervised DNN Regression on Airborne Hyperspectral Imagery for Improved Spatial Soil Properties Prediction. *Geoderma* **2021**, *385*, 114875. [CrossRef]
234. Haq, M.A.; Alshehri, M.; Rahaman, G.; Ghosh, A.; Baral, P.; Shekhar, C. Snow and Glacial Feature Identification Using Hyperion Dataset and Machine Learning Algorithms. *Arab. J. Geosci.* **2021**, *14*, 1525. [CrossRef]
235. Ji, C.; Li, X.; Wang, J.; Chen, M.; Pan, J. A Proposed Fully Constrained Least Squares for Solving Sparse Endmember Fractions with Linear Spectral Mixture Model. In Proceedings of the 2021 IEEE International Geoscience and Remote Sensing Symposium IGARSS, Brussels, Belgium, 11 July 2021; pp. 4143–4146.
236. Seydi, S.T.; Hasanlou, M. A New Structure for Binary and Multiple Hyperspectral Change Detection Based on Spectral Unmixing and Convolutional Neural Network. *Measurement* **2021**, *186*, 110137. [CrossRef]
237. Seydi, S.T.; Shah-Hosseini, R.; Hasanlou, M. New Framework for Hyperspectral Change Detection Based on Multi-Level Spectral Unmixing. *Appl. Geomat.* **2021**, *13*, 763–780. [CrossRef]
238. Cerra, D.; Pato, M.; Alonso, K.; Köhler, C.; Schneider, M.; de los Reyes, R.; Carmona, E.; Richter, R.; Kurz, F.; Reinartz, P.; et al. Dlr Hysu—a Benchmark Dataset for Spectral Unmixing. *Remote Sens.* **2021**, *13*, 2559. [CrossRef]
239. Chen, A.; Yang, X.; Xu, B.; Jin, Y.; Guo, J.; Xing, X.; Yang, D.; Wang, P.; Zhu, L. Monitoring the Spatiotemporal Dynamics of Aeolian Desertification Using Google Earth Engine. *Remote Sens.* **2021**, *13*, 1730. [CrossRef]
240. Lombard, F.; Andrieu, J. Mapping Mangrove Zonation Changes in Senegal with Landsat Imagery Using an OBIA Approach Combined with Linear Spectral Unmixing. *Remote Sens.* **2021**, *13*, 1961. [CrossRef]
241. Racoviteanu, A.E.; Nicholson, L.; Glasser, N.F. Surface Composition of Debris-Covered Glaciers across the Himalaya Using Linear Spectral Unmixing of Landsat 8 OLI Imagery. *Cryosphere* **2021**, *15*, 4557–4588. [CrossRef]

242. Shen, J.; Shuai, Y.; Li, P.; Cao, Y.; Ma, X. Extraction and Spatio-Temporal Analysis of Impervious Surfaces over Dongying Based on Landsat Data. *Remote Sens.* **2021**, *13*, 3666. [CrossRef]
243. Shumack, S.; Fisher, A.; Hesse, P.P. Refining Medium Resolution Fractional Cover for Arid Australia to Detect Vegetation Dynamics and Wind Erosion Susceptibility on Longitudinal Dunes. *Remote Sens. Environ.* **2021**, *265*, 112647. [CrossRef]
244. Vermeulen, L.M.; Munch, Z.; Palmer, A. Fractional Vegetation Cover Estimation in Southern African Rangelands Using Spectral Mixture Analysis and Google Earth Engine. *Comput. Electron. Agric.* **2021**, *182*, 105980. [CrossRef]
245. Chen, R.; Li, X.; Zhang, Y.; Zhou, P.; Wang, Y.; Shi, L.; Jiang, L.; Ling, F.; Du, Y. Spatiotemporal Continuous Impervious Surface Mapping by Fusion of Landsat Time Series Data and Google Earth Imagery. *Remote Sens.* **2021**, *13*, 2409. [CrossRef]
246. Chen, Y.; Huang, X.; Huang, J.; Liu, S.; Lu, D.; Zhao, S. Fractional Monitoring of Desert Vegetation Degradation, Recovery, and Greening Using Optimized Multi-Endmembers Spectral Mixture Analysis in a Dryland Basin of Northwest China. *GIScience Remote Sens.* **2021**, *58*, 300–321. [CrossRef]
247. Converse, R.L.; Lippitt, C.D.; Lippitt, C.L. Assessing Drought Vegetation Dynamics in Semiarid Grass- and Shrubland Using MESMA. *Remote Sens.* **2021**, *13*, 3840. [CrossRef]
248. Dutta, D.; Rahman, A.; Paul, S.K.; Kundu, A. Impervious Surface Growth and Its Inter-Relationship with Vegetation Cover and Land Surface Temperature in Peri-Urban Areas of Delhi. *Urban Clim.* **2021**, *37*, 100799. [CrossRef]
249. Finger, D.J.I.; McPherson, M.L.; Houskeeper, H.F.; Kudela, R.M. Mapping Bull Kelp Canopy in Northern California Using Landsat to Enable Long-Term Monitoring. *Remote Sens. Environ.* **2021**, *254*, 112243. [CrossRef]
250. Jiji, G.W. A Study on the Analysis of Heavy Metal Concentration Using Spectral Mixture Modelling Approach and Regression in Tirupur, India. *Earth Sci. Inf.* **2021**, *14*, 2077–2086. [CrossRef]
251. Li, M.; Zheng, Z.; Zhu, M.; He, Y.; Xia, J.; Chen, X.; Peng, Q.; He, Y.; Zhang, X.; Li, P. The Spatiotemporal Evolution of Urban Impervious Surface for Chengdu, China. *Photogramm Eng. Remote Sens.* **2021**, *87*, 491–502. [CrossRef]
252. Sall, I.; Jarchow, C.J.; Sigafus, B.H.; Eby, L.A.; Forzley, M.J.; Hossack, B.R. Estimating Inundation of Small Waterbodies with Sub-pixel Analysis of Landsat Imagery: Long-term Trends in Surface Water Area and Evaluation of Common Drought Indices. *Remote Sens. Ecol. Conserv.* **2021**, *7*, 109–124. [CrossRef]
253. Wu, K.; Chen, T.; Xu, Y.; Song, D.; Li, H. A Novel Change Detection Approach Based on Spectral Unmixing from Stacked Multitemporal Remote Sensing Images with a Variability of Endmembers. *Remote Sens.* **2021**, *13*, 2550. [CrossRef]
254. Bair, E.H.; Stillinger, T.; Dozier, J. Snow Property Inversion from Remote Sensing (SPIReS): A Generalized Multispectral Unmixing Approach with Examples from MODIS and Landsat 8 OLI. *IEEE Trans. Geosci. Remote Sens.* **2021**, *59*, 7270–7284. [CrossRef]
255. Feng, S.; Fan, F. Impervious Surface Extraction Based on Different Methods from Multiple Spatial Resolution Images: A Comprehensive Comparison. *Int. J. Digit. Earth* **2021**, *14*, 1148–1174. [CrossRef]
256. Fernández-García, V.; Marcos, E.; Fernández-Guisuraga, J.M.; Fernández-Manso, A.; Quintano, C.; Suárez-Seoane, S.; Calvo, L. Multiple Endmember Spectral Mixture Analysis (MESMA) Applied to the Study of Habitat Diversity in the Fine-Grained Landscapes of the Cantabrian Mountains. *Remote Sens.* **2021**, *13*, 979. [CrossRef]
257. Li, W. Improving Urban Impervious Surfaces Mapping through Integrating Statistical Methods and Spectral Mixture Analysis. *Remote Sens.* **2021**, *13*, 2474. [CrossRef]
258. Muhuri, A.; Gascoin, S.; Menzel, L.; Kostadinov, T.S.; Harpold, A.A.; Sanmiguel-Vallelado, A.; Lopez-Moreno, J.I. Performance Assessment of Optical Satellite-Based Operational Snow Cover Monitoring Algorithms in Forested Landscapes. *IEEE J. Sel. Top. Appl. Earth Obs. Remote Sens.* **2021**, *14*, 7159–7178. [CrossRef]
259. Zang, J.; Zhang, T.; Chen, L.; Li, L.; Liu, W.; Yuan, L.; Zhang, Y.; Liu, R.; Wang, Z.; Yu, Z.; et al. Optimization of Modelling Population Density Estimation Based on Impervious Surfaces. *Land* **2021**, *10*, 791. [CrossRef]
260. Luo, H.; Chen, N. A Combined Unmixing Framework for Impervious Surface Mapping on Medium-Resolution Images with Visible Shadows. *Photogramm. Eng. Remote Sens.* **2021**, *87*, 431–443. [CrossRef]
261. Pan, F.; Jiang, L.; Wang, G.; Su, X.; Zhou, X. Estimating Cloud-Free Fractional Snow Cover from Himawari-8, FY-4A and Modis Observation. In Proceedings of the 2021 IEEE International Geoscience and Remote Sensing Symposium IGARSS, Brussels, Belgium, 11 July 2021; pp. 5566–5569.
262. Rittger, K.; Krock, M.; Kleiber, W.; Bair, E.H.; Brodzik, M.J.; Stephenson, T.R.; Rajagopalan, B.; Bormann, K.J.; Painter, T.H. Multi-Sensor Fusion Using Random Forests for Daily Fractional Snow Cover at 30 m. *Remote Sens. Environ.* **2021**, *264*, 112608. [CrossRef]
263. Sun, Q.; Zhang, P.; Jiao, X.; Han, W.; Sun, Y.; Sun, D. Identifying and Understanding Alternative States of Dryland Landscape: A Hierarchical Analysis of Time Series of Fractional Vegetation-Soil Nexuses in China's Hexi Corridor. *Landsc. Urban Plan.* **2021**, *215*, 104225. [CrossRef]
264. Yang, Y.; Wu, T.; Zeng, Y.; Wang, S. An Adaptive-Parameter Pixel Unmixing Method for Mapping Evergreen Forest Fractions Based on Time-Series NDVI: A Case Study of Southern China. *Remote Sens.* **2021**, *13*, 4678. [CrossRef]
265. Benhalouche, F.Z.; Benabbou, O.; Kebir, L.W.; Bennia, A.; Karoui, M.S.; Deville, Y. An Informed NMF-Based Unmixing Approach for Mineral Detection and Mapping in the Algerian Central Hoggar Using PRISMA Remote Sensing Hyperspectral Data. In Proceedings of the 2021 IEEE International Geoscience and Remote Sensing Symposium IGARSS, Brussels, Belgium, 11 July 2021; pp. 1863–1866.
266. Zhao, M.; Chen, J.; Rahardja, S. Hyperspectral Shadow Removal via Nonlinear Unmixing. *IEEE Geosci. Remote Sens. Lett.* **2021**, *18*, 881–885. [CrossRef]

267. Jin, Q.; Ma, Y.; Fan, F.; Huang, J.; Mei, X.; Ma, J. Adversarial Autoencoder Network for Hyperspectral Unmixing. *IEEE Trans. Neural Netw. Learn. Syst.* **2021**, 1–15. [CrossRef]
268. Han, Z.; Hong, D.; Gao, L.; Chanussot, J.; Zhang, B. EvoNAS: Evolvable Neural Architecture Search for Hyperspectral Unmixing. In Proceedings of the 2021 IEEE International Geoscience and Remote Sensing Symposium IGARSS, Brussels, Belgium, 11 July 2021; pp. 3325–3328.
269. Xu, F.; Somers, B. Unmixing-Based Sentinel-2 Downscaling for Urban Land Cover Mapping. *ISPRS J. Photogramm. Remote Sens.* **2021**, *171*, 133–154. [CrossRef]
270. Shen, M.; Tang, M.; Li, Y. Phenology and Spectral Unmixing-Based Invasive Kudzu Mapping: A Case Study in Knox County, Tennessee. *Remote Sens.* **2021**, *13*, 4551. [CrossRef]
271. Kneib, M.; Miles, E.S.; Jola, S.; Buri, P.; Herreid, S.; Bhattacharya, A.; Watson, C.S.; Bolch, T.; Quincey, D.; Pellicciotti, F. Mapping Ice Cliffs on Debris-Covered Glaciers Using Multispectral Satellite Images. *Remote Sens. Environ.* **2021**, *253*, 112201. [CrossRef]
272. Soydan, H.; Koz, A.; Düzgün, H.Ş. Secondary Iron Mineral Detection via Hyperspectral Unmixing Analysis with Sentinel-2 Imagery. *Int. J. Appl. Earth Obs. Geoinf.* **2021**, *101*, 102343. [CrossRef]
273. Mudereri, B.T.; Abdel-Rahman, E.M.; Dube, T.; Niassy, S.; Khan, Z.; Tonnang, H.E.Z.; Landmann, T. A Two-Step Approach for Detecting Striga in a Complex Agroecological System Using Sentinel-2 Data. *Sci. Total Environ.* **2021**, *762*, 143151. [CrossRef]
274. Yuan, N.; Gong, Y.; Fang, S.; Liu, Y.; Duan, B.; Yang, K.; Wu, X.; Zhu, R. UAV Remote Sensing Estimation of Rice Yield Based on Adaptive Spectral Endmembers and Bilinear Mixing Model. *Remote Sens.* **2021**, *13*, 2190. [CrossRef]
275. Sun, X.; Wu, W.; Li, X.; Xu, X.; Li, J. Vegetation Abundance and Health Mapping Over Southwestern Antarctica Based on WorldView-2 Data and a Modified Spectral Mixture Analysis. *Remote Sens.* **2021**, *13*, 166. [CrossRef]
276. Ma, X.; Lu, L.; Ding, J.; Zhang, F.; He, B. Estimating Fractional Vegetation Cover of Row Crops from High Spatial Resolution Image. *Remote Sens.* **2021**, *13*, 3874. [CrossRef]
277. Markiet, V.; Mõttus, M. Estimation of Boreal Forest Floor Reflectance from Airborne Hyperspectral Data of Coniferous Forests. *Remote Sens. Environ.* **2020**, *249*, 112018. [CrossRef]
278. Benhalouche, F.Z.; Benabbou, O.; Karoui, M.S.; Kebir, L.W.; Deville, Y. Detecting and Mapping Kaolinite In The Algerian Central Hoggar With A Partial Linear Nmf-Based Unmixing Method. In Proceedings of the 2020 Mediterranean and Middle-East Geoscience and Remote Sensing Symposium (M2GARSS), Tunis, Tunisia, 11 March 2020; pp. 204–207.
279. Takodjou Wambo, J.D.; Pour, A.B.; Ganno, S.; Asimow, P.D.; Zoheir, B.; Salles, R.D.R.; Nzenti, J.P.; Pradhan, B.; Muslim, A.M. Identifying High Potential Zones of Gold Mineralization in a Sub-Tropical Region Using Landsat-8 and ASTER Remote Sensing Data: A Case Study of the Ngoura-Colomines Goldfield, Eastern Cameroon. *Ore. Geol. Rev.* **2020**, *122*, 103530. [CrossRef]
280. Salehi, S.; Mielke, C.; Rogass, C. Mapping Ultramafic Complexes Using Airborne Imaging Spectroscopy and Spaceborne Data in Arctic Regions with Abundant Lichen Cover, a Case Study from the Niaqornarssuit Complex in South West Greenland. *Eur. J. Remote Sens.* **2020**, *53*, 156–175. [CrossRef]
281. Bai, J.; Feng, R.; Wang, L.; Li, H.; Li, F.; Zhong, Y.; Zhang, L. Semi-Supervised Hyperspectral Unmixing with Very Deep Convolutional Neural Networks. In Proceedings of the IGARSS 2020—2020 IEEE International Geoscience and Remote Sensing Symposium, Waikoloa, HI, USA, 26 September 2020; pp. 2400–2403.
282. Borsoi, R.A.; Imbiriba, T.; Bermudez, J.C.M. A Data Dependent Multiscale Model for Hyperspectral Unmixing With Spectral Variability. *IEEE Trans. Image Process.* **2020**, *29*, 3638–3651. [CrossRef] [PubMed]
283. Borsoi, R.A.; Imbiriba, T.; Bermudez, J.C.M.; Richard, C. A Blind Multiscale Spatial Regularization Framework for Kernel-Based Spectral Unmixing. *IEEE Trans. Image Process.* **2020**, *29*, 4965–4979. [CrossRef] [PubMed]
284. Elkholy, M.M.; Mostafa, M.; Ebied, H.M.; Tolba, M.F. Hyperspectral Unmixing Using Deep Convolutional Autoencoder. *Int. J. Remote Sens.* **2020**, *41*, 4799–4819. [CrossRef]
285. Fang, B.; Bai, Y.; Li, Y. Combining Spectral Unmixing and 3D/2D Dense Networks with Early-Exiting Strategy for Hyperspectral Image Classification. *Remote Sens.* **2020**, *12*, 779. [CrossRef]
286. Fathy, G.M.; Hassan, H.A.; Rahwan, S.; Sheta, W.M. Parallel Implementation of Multiple Kernel Self-Organizing Maps for Spectral Unmixing. *J. Real-Time Image Proc.* **2020**, *17*, 1267–1284. [CrossRef]
287. Han, H.; Wang, G.; Wang, M.; Miao, J.; Guo, S.; Chen, L.; Zhang, M.; Guo, K. Hyperspectral Unmixing Via Nonconvex Sparse and Low-Rank Constraint. *IEEE J. Sel. Top. Appl. Earth Obs. Remote Sens.* **2020**, *13*, 5704–5718. [CrossRef]
288. Holland, W.; Du, Q. Adversarially Regularized Autoencoder for Hyperspectral Image Unmixing. In Proceedings of the Image and Signal Processing for Remote Sensing XXVI, SPIE, Online Only, 20 September 2020; p. 29.
289. Hua, Z.; Li, X.; Chen, S.; Zhao, L. Hyperspectral Unmixing with Scaled and Perturbed Linear Mixing Model to Address Spectral Variability. *J. Appl. Rem. Sens.* **2020**, *14*, 1. [CrossRef]
290. Karoui, M.S.; Djerriri, K.; Boukerch, I. Unsupervised Hyperspectral Band Selection by Sequentially Clustering A Mahalanobis-Based Dissimilarity Of Spectrally Variable Endmembers. In Proceedings of the 2020 Mediterranean and Middle-East Geoscience and Remote Sensing Symposium (M2GARSS), Tunis, Tunisia, 11 March 2020; pp. 33–36.
291. Zhou, Y.; Wetherley, E.B.; Gader, P.D. Unmixing Urban Hyperspectral Imagery Using Probability Distributions to Represent Endmember Variability. *Remote Sens. Environ.* **2020**, *246*, 111857. [CrossRef]
292. Vijayashekhar, S.; Bhatt, J.S.; Chattopadhyay, B. Virtual Dimensionality of Hyperspectral Data: Use of Multiple Hypothesis Testing for Controlling Type-I Error. *IEEE J. Sel. Top. Appl. Earth Obs. Remote Sens.* **2020**, *13*, 2974–2985.

293. Rathnayake, B.; Ekanayake, E.M.M.B.; Weerakoon, K.; Godaliyadda, G.M.R.I.; Ekanayake, M.P.B.; Herath, H.M.V.R. Graph-Based Blind Hyperspectral Unmixing via Nonnegative Matrix Factorization. *IEEE Trans. Geosci. Remote Sens.* **2020**, *58*, 6391–6409. [CrossRef]
294. Yang, B.; Chen, Z. An Improved Bilinear Mixture Model Considering Adjacency and Shade Effects. In Proceedings of the IGARSS 2020—2020 IEEE International Geoscience and Remote Sensing Symposium, Waikoloa, HI, USA, 26 September 2020; pp. 2161–2164.
295. Xu, M.; Zhang, Y.; Fan, Y.; Chen, Y.; Song, D. Linear Spectral Mixing Model-Guided Artificial Bee Colony Method for Endmember Generation. *IEEE Geosci. Remote Sens. Lett.* **2020**, *17*, 2145–2149. [CrossRef]
296. Xu, N.; Hu, Y.; Geng, X.; Wang, Y. A Geometric View of Fast Gram Determinant-Based Endmember Extraction Algorithm for Hyperspectral Imagery. In Proceedings of the IGARSS 2020—2020 IEEE International Geoscience and Remote Sensing Symposium, Waikoloa, HI, USA, 26 September 2020; pp. 2181–2184.
297. Peng, J.; Jiang, F.; Sun, W.; Zhou, Y. Cauchy NMF for Hyperspectral Unmixing. In Proceedings of the IGARSS 2020—2020 IEEE International Geoscience and Remote Sensing Symposium, Waikoloa, HI, USA, 26 September 2020; pp. 2384–2387.
298. Yang, J.; Jia, M.; Xu, C.; Li, S. Joint Hyperspectral Unmixing for Urban Computing. *Geoinformatica* **2020**, *24*, 247–265. [CrossRef]
299. Chen, S.; Cao, Y.; Chen, L.; Guo, X. Geometrical Constrained Independent Component Analysis for Hyperspectral Unmixing. *Int. J. Remote Sens.* **2020**, *41*, 6783–6804. [CrossRef]
300. Das, S.; Routray, A.; Deb, A.K. Efficient Tensor Decomposition Approach for Estimation of the Number of Endmembers in a Hyperspectral Image. *J. Appl. Rem. Sens.* **2020**, *14*, 1. [CrossRef]
301. Dou, Z.; Gao, K.; Zhang, X.; Wang, H.; Wang, J. Hyperspectral Unmixing Using Orthogonal Sparse Prior-Based Autoencoder With Hyper-Laplacian Loss and Data-Driven Outlier Detection. *IEEE Trans. Geosci. Remote Sens.* **2020**, *58*, 6550–6564. [CrossRef]
302. Huang, Y.; Li, J.; Qi, L.; Wang, Y.; Gao, X. Spatial-Spectral Autoencoder Networks for Hyperspectral Unmixing. In Proceedings of the IGARSS 2020—2020 IEEE International Geoscience and Remote Sensing Symposium, Waikoloa, HI, USA, 26 September 2020; pp. 2396–2399.
303. Imbiriba, T.; Borsoi, R.A.; Bermudez, J.C.M. Low-Rank Tensor Modeling for Hyperspectral Unmixing Accounting for Spectral Variability. *IEEE Trans. Geosci. Remote Sens.* **2020**, *58*, 1833–1842. [CrossRef]
304. Jiang, X.; Gong, M.; Zhan, T.; Zhang, M. Multiobjective Endmember Extraction Based on Bilinear Mixture Model. *IEEE Trans. Geosci. Remote Sens.* **2020**, *58*, 8192–8210. [CrossRef]
305. Li, H.-C.; Liu, S.; Feng, X.-R.; Zhang, S.-Q. Sparsity-Constrained Coupled Nonnegative Matrix–Tensor Factorization for Hyperspectral Unmixing. *IEEE J. Sel. Top. Appl. Earth Obs. Remote Sens.* **2020**, *13*, 5061–5073. [CrossRef]
306. Lu, X.; Dong, L.; Yuan, Y. Subspace Clustering Constrained Sparse NMF for Hyperspectral Unmixing. *IEEE Trans. Geosci. Remote Sens.* **2020**, *58*, 3007–3019. [CrossRef]
307. Mei, S.; He, M.; Zhang, Y.; Wang, Z.; Feng, D. Improving Spatial–Spectral Endmember Extraction in the Presence of Anomalous Ground Objects. *IEEE Trans. Geosci. Remote Sens.* **2011**, *49*, 4210–4222. [CrossRef]
308. Qi, L.; Li, J.; Wang, Y.; Huang, Y.; Gao, X. Spectral–Spatial-Weighted Multiview Collaborative Sparse Unmixing for Hyperspectral Images. *IEEE Trans. Geosci. Remote Sens.* **2020**, *58*, 8766–8779. [CrossRef]
309. Qian, Y.; Xiong, F.; Qian, Q.; Zhou, J. Spectral Mixture Model Inspired Network Architectures for Hyperspectral Unmixing. *IEEE Trans. Geosci. Remote Sens.* **2020**, *58*, 7418–7434. [CrossRef]
310. Zhou, L.; Zhang, X.; Wang, J.; Bai, X.; Tong, L.; Zhang, L.; Zhou, J.; Hancock, E. Subspace Structure Regularized Nonnegative Matrix Factorization for Hyperspectral Unmixing. *IEEE J. Sel. Top. Appl. Earth Obs. Remote Sens.* **2020**, *13*, 4257–4270. [CrossRef]
311. Tong, L.; Zhou, J.; Qian, B.; Yu, J.; Xiao, C. Adaptive Graph Regularized Multilayer Nonnegative Matrix Factorization for Hyperspectral Unmixing. *IEEE J. Sel. Top. Appl. Earth Obs. Remote Sens.* **2020**, *13*, 434–447. [CrossRef]
312. Qi, L.; Li, J.; Wang, Y.; Lei, M.; Gao, X. Deep Spectral Convolution Network for Hyperspectral Image Unmixing with Spectral Library. *Signal Process.* **2020**, *176*, 107672. [CrossRef]
313. Shah, D.; Zaveri, T.; Trivedi, Y.N.; Plaza, A. Entropy-Based Convex Set Optimization for Spatial–Spectral Endmember Extraction from Hyperspectral Images. *IEEE J. Sel. Top. Appl. Earth Obs. Remote Sens.* **2020**, *13*, 4200–4213. [CrossRef]
314. Yuan, Y.; Zhang, Z.; Wang, Q. Improved Collaborative Non-Negative Matrix Factorization and Total Variation for Hyperspectral Unmixing. *IEEE J. Sel. Top. Appl. Earth Obs. Remote Sens.* **2020**, *13*, 998–1010. [CrossRef]
315. Tao, X.; Cui, T.; Plaza, A.; Ren, P. Simultaneously Counting and Extracting Endmembers in a Hyperspectral Image Based on Divergent Subsets. *IEEE Trans. Geosci. Remote Sens.* **2020**, *58*, 8952–8966. [CrossRef]
316. Xu, X.; Li, J.; Li, S.; Plaza, A. Generalized Morphological Component Analysis for Hyperspectral Unmixing. *IEEE Trans. Geosci. Remote Sens.* **2020**, *58*, 2817–2832. [CrossRef]
317. Zeng; Ritz; Zhao; Lan Attention-Based Residual Network with Scattering Transform Features for Hyperspectral Unmixing with Limited Training Samples. *Remote Sens.* **2020**, *12*, 400. [CrossRef]
318. Xu, X.; Li, J.; Li, S.; Plaza, A. Curvelet Transform Domain-Based Sparse Nonnegative Matrix Factorization for Hyperspectral Unmixing. *IEEE J. Sel. Top. Appl. Earth Obs. Remote Sens.* **2020**, *13*, 4908–4924. [CrossRef]
319. Siebels, K.; Goita, K.; Germain, M. Estimation of Mineral Abundance from Hyperspectral Data Using a New Supervised Neighbor-Band Ratio Unmixing Approach. *IEEE Trans. Geosci. Remote Sens.* **2020**, *58*, 6754–6766. [CrossRef]
320. Rasti, B.; Koirala, B.; Scheunders, P.; Ghamisi, P. How Hyperspectral Image Unmixing and Denoising Can Boost Each Other. *Remote Sens.* **2020**, *12*, 1728. [CrossRef]

321. Qu, K.; Bao, W. Multiple-*Priors* Ensemble Constrained Nonnegative Matrix Factorization for Spectral Unmixing. *IEEE J. Sel. Top. Appl. Earth Obs. Remote Sens.* **2020**, *13*, 963–975. [CrossRef]
322. Wang, W.; Qian, Y.; Liu, H. Multiple Clustering Guided Nonnegative Matrix Factorization for Hyperspectral Unmixing. *IEEE J. Sel. Top. Appl. Earth Obs. Remote Sens.* **2020**, *13*, 5162–5179. [CrossRef]
323. Xiong, F.; Zhou, J.; Lu, J.; Qian, Y. Nonconvex Nonseparable Sparse Nonnegative Matrix Factorization for Hyperspectral Unmixing. *IEEE J. Sel. Top. Appl. Earth Obs. Remote Sens.* **2020**, *13*, 6088–6100. [CrossRef]
324. Zhou, X.; Zhang, Y.; Zhang, J.; Shi, S. Alternating Direction Iterative Nonnegative Matrix Factorization Unmixing for Multispectral and Hyperspectral Data Fusion. *IEEE J. Sel. Top. Appl. Earth Obs. Remote Sens.* **2020**, *13*, 5223–5232. [CrossRef]
325. Uezato, T.; Yokoya, N.; He, W. Illumination Invariant Hyperspectral Image Unmixing Based on a Digital Surface Model. *IEEE Trans. Image Process.* **2020**, *29*, 3652–3664. [CrossRef] [PubMed]
326. Zhang, J.; Zhang, X.; Tang, X.; Chen, P.; Jiao, L. Sketch-Based Region Adaptive Sparse Unmixing Applied to Hyperspectral Image. *IEEE Trans. Geosci. Remote Sens.* **2020**, *58*, 8840–8856. [CrossRef]
327. Yang, B.; Chen, Z.; Wang, B. Nonlinear Endmember Identification for Hyperspectral Imagery via Hyperpath-Based Simplex Growing and Fuzzy Assessment. *IEEE J. Sel. Top. Appl. Earth Obs. Remote Sens.* **2020**, *13*, 351–366. [CrossRef]
328. Kompella, S.S.; Kadapala, B.K.R.; Abdul Hakeem, K.; Issac, A.M.; Annamalai, L. Accuracy Assessment and Normalisation of Water Spread Area Estimate from Multi-Sensor Satellite Data. *J. Indian Soc. Remote Sens.* **2020**, *48*, 1601–1611. [CrossRef]
329. Drumetz, L.; Chanussot, J.; Jutten, C.; Ma, W.-K.; Iwasaki, A. Spectral Variability Aware Blind Hyperspectral Image Unmixing Based on Convex Geometry. *IEEE Trans. Image Process.* **2020**, *29*, 4568–4582. [CrossRef]
330. Cooper, S.; Okujeni, A.; Jänicke, C.; Clark, M.; Van Der Linden, S.; Hostert, P. Disentangling Fractional Vegetation Cover: Regression-Based Unmixing of Simulated Spaceborne Imaging Spectroscopy Data. *Remote Sens. Environ.* **2020**, *246*, 111856. [CrossRef]
331. Sun, Q.; Zhang, P.; Wei, H.; Liu, A.; You, S.; Sun, D. Improved Mapping and Understanding of Desert Vegetation-Habitat Complexes from Intraannual Series of Spectral Endmember Space Using Cross-Wavelet Transform and Logistic Regression. *Remote Sens. Environ.* **2020**, *236*, 111516. [CrossRef]
332. Liu, D.; Chen, W.; Menz, G.; Dubovyk, O. Development of Integrated Wetland Change Detection Approach: In Case of Erdos Larus Relictus National Nature Reserve, China. *Sci. Total Environ.* **2020**, *731*, 139166. [CrossRef]
333. Ji, C.; Li, X.; Wei, H.; Li, S. Comparison of Different Multispectral Sensors for Photosynthetic and Non-Photosynthetic Vegetation-Fraction Retrieval. *Remote Sens.* **2020**, *12*, 115. [CrossRef]
334. Aldeghlawi, M.; Alkhatib, M.Q.; Velez-Reyes, M. Evaluating Column Subset Selection Methods for Endmember Extraction in Hyperspectral Unmixing. In Proceedings of the Algorithms, Technologies, and Applications for Multispectral and Hyperspectral Imagery XXVI, SPIE, Online Only, 9 June 2020; p. 46.
335. Zhu, F.; Honeine, P.; Chen, J. Pixel-Wise Linear/Nonlinear Nonnegative Matrix Factorization for Unmixing of Hyperspectral Data. In Proceedings of the ICASSP 2020—2020 IEEE International Conference on Acoustics, Speech and Signal Processing (ICASSP), Barcelona, Spain, 4–8 May 2020; pp. 4737–4741.
336. Moghadam, H.J.; Oskouei, M.M.; Nouri, T. Unmixing of Hyperspectral Data for Mineral Detection Using a Hybrid Method, Sar Chah-e Shur, Iran. *Arab. J. Geosci.* **2020**, *13*, 1041. [CrossRef]
337. Zhang, G.; Cerra, D.; Müller, R. Shadow Detection and Restoration for Hyperspectral Images Based on Nonlinear Spectral Unmixing. *Remote Sens.* **2020**, *12*, 3985. [CrossRef]
338. Lyu, X.; Li, X.; Dang, D.; Dou, H.; Xuan, X.; Liu, S.; Li, M.; Gong, J. A New Method for Grassland Degradation Monitoring by Vegetation Species Composition Using Hyperspectral Remote Sensing. *Ecol. Indic.* **2020**, *114*, 106310. [CrossRef]
339. Montorio, R.; Pérez-Cabello, F.; Borini Alves, D.; García-Martín, A. Unitemporal Approach to Fire Severity Mapping Using Multispectral Synthetic Databases and Random Forests. *Remote Sens. Environ.* **2020**, *249*, 112025. [CrossRef]
340. Aalstad, K.; Westermann, S.; Bertino, L. Evaluating Satellite Retrieved Fractional Snow-Covered Area at a High-Arctic Site Using Terrestrial Photography. *Remote Sens. Environ.* **2020**, *239*, 111618. [CrossRef]
341. Binh, D.V.; Wietlisbach, B.; Kantoush, S.; Loc, H.H.; Park, E.; Cesare, G.D.; Cuong, D.H.; Tung, N.X.; Sumi, T. A Novel Method for River Bank Detection from Landsat Satellite Data: A Case Study in the Vietnamese Mekong Delta. *Remote Sens.* **2020**, *12*, 3298. [CrossRef]
342. Fernández-Guisuraga, J.M.; Calvo, L.; Suárez-Seoane, S. Comparison of Pixel Unmixing Models in the Evaluation of Post-Fire Forest Resilience Based on Temporal Series of Satellite Imagery at Moderate and Very High Spatial Resolution. *ISPRS J. Photogramm. Remote Sens.* **2020**, *164*, 217–228. [CrossRef]
343. Laamrani, A.; Joosse, P.; McNairn, H.; Berg, A.; Hagerman, J.; Powell, K.; Berry, M. Assessing Soil Cover Levels during the Non-Growing Season Using Multitemporal Satellite Imagery and Spectral Unmixing Techniques. *Remote Sens.* **2020**, *12*, 1397. [CrossRef]
344. Trinder, J.; Liu, Q. Assessing Environmental Impacts of Urban Growth Using Remote Sensing. *Geo-Spat. Inf. Sci.* **2020**, *23*, 20–39. [CrossRef]
345. Senf, C.; Laštovička, J.; Okujeni, A.; Heurich, M.; Van Der Linden, S. A Generalized Regression-Based Unmixing Model for Mapping Forest Cover Fractions throughout Three Decades of Landsat Data. *Remote Sens. Environ.* **2020**, *240*, 111691. [CrossRef]
346. Wang, Q.; Zhang, C.; Tong, X.; Atkinson, P.M. General Solution to Reduce the Point Spread Function Effect in Subpixel Mapping. *Remote Sens. Environ.* **2020**, *251*, 112054. [CrossRef]

347. Peroni Venancio, L.; Chartuni Mantovani, E.; Do Amaral, C.H.; Usher Neale, C.M.; Zution Gonçalves, I.; Filgueiras, R.; Coelho Eugenio, F. Potential of Using Spectral Vegetation Indices for Corn Green Biomass Estimation Based on Their Relationship with the Photosynthetic Vegetation Sub-Pixel Fraction. *Agric. Water Manag.* **2020**, *236*, 106155. [CrossRef]
348. Lymburner, L.; Bunting, P.; Lucas, R.; Scarth, P.; Alam, I.; Phillips, C.; Ticehurst, C.; Held, A. Mapping the Multi-Decadal Mangrove Dynamics of the Australian Coastline. *Remote Sens. Environ.* **2020**, *238*, 111185. [CrossRef]
349. Bullock, E.L.; Woodcock, C.E.; Olofsson, P. Monitoring Tropical Forest Degradation Using Spectral Unmixing and Landsat Time Series Analysis. *Remote Sens. Environ.* **2020**, *238*, 110968. [CrossRef]
350. Czekajlo, A.; Coops, N.C.; Wulder, M.A.; Hermosilla, T.; Lu, Y.; White, J.C.; Van Den Bosch, M. The Urban Greenness Score: A Satellite-Based Metric for Multi-Decadal Characterization of Urban Land Dynamics. *Int. J. Appl. Earth Obs. Geoinf.* **2020**, *93*, 102210. [CrossRef]
351. Dai, J.; Roberts, D.A.; Stow, D.A.; An, L.; Hall, S.J.; Yabiku, S.T.; Kyriakidis, P.C. Mapping Understory Invasive Plant Species with Field and Remotely Sensed Data in Chitwan, Nepal. *Remote Sens. Environ.* **2020**, *250*, 112037. [CrossRef]
352. Khan, I.A.; Khan, M.R.; Baig, M.H.A.; Hussain, Z.; Hameed, N.; Khan, J.A. Assessment of Forest Cover and Carbon Stock Changes in Sub-Tropical Pine Forest of Azad Jammu & Kashmir (AJK), Pakistan Using Multi-Temporal Landsat Satellite Data and Field Inventory. *PLoS ONE* **2020**, *15*, e0226341. [CrossRef]
353. Shimabukuro, Y.E.; Dutra, A.C.; Arai, E.; Duarte, V.; Cassol, H.L.G.; Pereira, G.; Cardozo, F.D.S. Mapping Burned Areas of Mato Grosso State Brazilian Amazon Using Multisensor Datasets. *Remote Sens.* **2020**, *12*, 3827. [CrossRef]
354. Shih, H.; Stow, D.A.; Tsai, Y.; Roberts, D.A. Estimating the Starting Time and Identifying the Type of Urbanization Based on Dense Time Series of Landsat-Derived Vegetation-Impervious-Soil (V-I-S) Maps—A Case Study of North Taiwan from 1990 to 2015. *Int. J. Appl. Earth Obs. Geoinf.* **2020**, *85*, 101987. [CrossRef]
355. Yin, C.L.; Meng, F.; Xu, Y.N.; Yang, X.Y.; Xing, H.Q.; Fu, P.J. Developing Urban Built-up Area Extraction Method Based on Land Surface Emissivity Differences. *Infrared Phys. Technol.* **2020**, *110*, 103475. [CrossRef]
356. He, Y.; Yang, J.; Guo, X. Green Vegetation Cover Dynamics in a Heterogeneous Grassland: Spectral Unmixing of Landsat Time Series from 1999 to 2014. *Remote Sens.* **2020**, *12*, 3826. [CrossRef]
357. Thayn, J.B. Monitoring Narrow Mangrove Stands in Baja California Sur, Mexico Using Linear Spectral Unmixing. *Mar. Geod.* **2020**, *43*, 493–508. [CrossRef]
358. Jarchow, C.J.; Sigafus, B.H.; Muths, E.; Hossack, B.R. Using Full and Partial Unmixing Algorithms to Estimate the Inundation Extent of Small, Isolated Stock Ponds in an Arid Landscape. *Wetlands* **2020**, *40*, 563–575. [CrossRef]
359. Lewińska, K.E.; Hostert, P.; Buchner, J.; Bleyhl, B.; Radeloff, V.C. Short-Term Vegetation Loss versus Decadal Degradation of Grasslands in the Caucasus Based on Cumulative Endmember Fractions. *Remote Sens. Environ.* **2020**, *248*, 111969. [CrossRef]
360. Li, W. Mapping Urban Impervious Surfaces by Using Spectral Mixture Analysis and Spectral Indices. *Remote Sens.* **2019**, *12*, 94. [CrossRef]
361. Cavalli, R.M. Local, Daily, and Total Bio-Optical Models of Coastal Waters of Manfredonia Gulf Applied to Simulated Data of CHRIS, Landsat TM, MIVIS, MODIS, and PRISMA Sensors for Evaluating the Error. *Remote Sens.* **2020**, *12*, 1428. [CrossRef]
362. Wright, N.C.; Polashenski, C.M. How Machine Learning and High-Resolution Imagery Can Improve Melt Pond Retrieval from MODIS Over Current Spectral Unmixing Techniques. *J. Geophys. Res. Ocean.* **2020**, *125*. [CrossRef]
363. Singh, K.K.; Gray, J. Mapping Understory Invasive Plants in Urban Forests with Spectral and Temporal Unmixing of Landsat Imagery. *Photogramm. Eng. Remote Sens.* **2020**, *86*, 509–518. [CrossRef]
364. Firozjaei, M.K.; Weng, Q.; Zhao, C.; Kiavarz, M.; Lu, L.; Alavipanah, S.K. Surface Anthropogenic Heat Islands in Six Megacities: An Assessment Based on a Triple-Source Surface Energy Balance Model. *Remote Sens. Environ.* **2020**, *242*, 111751. [CrossRef]
365. Ling, F.; Li, X.; Foody, G.M.; Boyd, D.; Ge, Y.; Li, X.; Du, Y. Monitoring Surface Water Area Variations of Reservoirs Using Daily MODIS Images by Exploring Sub-Pixel Information. *ISPRS J. Photogramm. Remote Sens.* **2020**, *168*, 141–152. [CrossRef]
366. Wang, J.; Yang, D.; Detto, M.; Nelson, B.W.; Chen, M.; Guan, K.; Wu, S.; Yan, Z.; Wu, J. Multi-Scale Integration of Satellite Remote Sensing Improves Characterization of Dry-Season Green-up in an Amazon Tropical Evergreen Forest. *Remote Sens. Environ.* **2020**, *246*, 111865. [CrossRef]
367. PROBA-V. Available online: https://earth.esa.int/eogateway/missions/proba-v (accessed on 15 May 2023).
368. Arai, E.; Eyji Sano, E.; Dutra, A.C.; Cassol, H.L.G.; Hoffmann, T.B.; Shimabukuro, Y.E. Vegetation Fraction Images Derived from PROBA-V Data for Rapid Assessment of Annual Croplands in Brazil. *Remote Sens.* **2020**, *12*, 1152. [CrossRef]
369. Godinho Cassol, H.L.; Arai, E.; Eyji Sano, E.; Dutra, A.C.; Hoffmann, T.B.; Shimabukuro, Y.E. Maximum Fraction Images Derived from Year-Based Project for On-Board Autonomy-Vegetation (PROBA-V) Data for the Rapid Assessment of Land Use and Land Cover Areas in Mato Grosso State, Brazil. *Land* **2020**, *9*, 139. [CrossRef]
370. Shimabukuro, Y.E.; Arai, E.; Duarte, V.; Dutra, A.C.; Cassol, H.L.G.; Sano, E.E.; Hoffmann, T.B. Discriminating Land Use and Land Cover Classes in Brazil Based on the Annual PROBA-V 100 m Time Series. *IEEE J. Sel. Top. Appl. Earth Obs. Remote Sens.* **2020**, *13*, 3409–3420. [CrossRef]
371. Redowan, M.; Phinn, S.; Roelfsema, C.; Aziz, A.A. CLASlite Unmixing of Landsat Images to Estimate REDD+ Activity Data for Deforestation in a Bangladesh Forest. *J. Appl. Rem. Sens.* **2020**, *14*, 1. [CrossRef]
372. Patel, J.R.; Joshi, M.V.; Bhatt, J.S. A Novel Approach for Hyperspectral Image Superresolution Using Spectral Unmixing and Transfer Learning. In Proceedings of the IGARSS 2020—2020 IEEE International Geoscience and Remote Sensing Symposium, Waikoloa, HI, USA, 26 September 2020; pp. 1512–1515.

373. Wang, K.; Wang, Y.; Zhao, X.-L.; Chan, J.C.-W.; Xu, Z.; Meng, D. Hyperspectral and Multispectral Image Fusion via Nonlocal Low-Rank Tensor Decomposition and Spectral Unmixing. *IEEE Trans. Geosci. Remote Sens.* **2020**, *58*, 7654–7671. [CrossRef]
374. Yang, L.; Peng, J.; Su, H.; Xu, L.; Wang, Y.; Yu, B. Combined Nonlocal Spatial Information and Spatial Group Sparsity in NMF for Hyperspectral Unmixing. *IEEE Geosci. Remote Sens. Lett.* **2020**, *17*, 1767–1771. [CrossRef]
375. Wang, L.; Zhu, Q.; Zeng, W.; Zhong, Y.; Guan, Q.; Zhang, L.; Li, D. Semi-Automatic Fully Sparse Semantic Modeling Framework for Hyperspectral Unmixing. In Proceedings of the IGARSS 2020—2020 IEEE International Geoscience and Remote Sensing Symposium, Waikoloa, HI, USA, 26 September 2020; pp. 2388–2391.
376. Yue, J.; Tian, Q.; Dong, X.; Xu, N. Using Broadband Crop Residue Angle Index to Estimate the Fractional Cover of Vegetation, Crop Residue, and Bare Soil in Cropland Systems. *Remote Sens. Environ.* **2020**, *237*, 111538. [CrossRef]
377. Carlson, B.Z.; Hébert, M.; Van Reeth, C.; Bison, M.; Laigle, I.; Delestrade, A. Monitoring the Seasonal Hydrology of Alpine Wetlands in Response to Snow Cover Dynamics and Summer Climate: A Novel Approach with Sentinel-2. *Remote Sens.* **2020**, *12*, 1959. [CrossRef]
378. Fraga, R.S.; Guedes, H.A.S.; Martins, V.S.; Caballero, C.B.; Mendes, K.G.P.; Monks, J.L.F.; Fassoni-Andrade, A.C. Empirical Modelling of Suspended Solids in a Subtropical Lagoon (Brazil) Using Linear Spectral Mixing Algorithm. *Remote Sens. Appl. Soc. Environ.* **2020**, *20*, 100380. [CrossRef]
379. Girolamo-Neto, C.D.; Sato, L.Y.; Sanches, I.D.; Silva, I.C.O.; Rocha, J.C.S.; Almeida, C.A. Object based image analysis and texture features for pasture classification in brazilian savannah. *ISPRS Ann. Photogramm. Remote Sens. Spat. Inf. Sci.* **2020**, *V-3–2020*, 453–460. [CrossRef]
380. Huechacona-Ruiz, A.H.; Dupuy, J.M.; Schwartz, N.B.; Powers, J.S.; Reyes-García, C.; Tun-Dzul, F.; Hernández-Stefanoni, J.L. Mapping Tree Species Deciduousness of Tropical Dry Forests Combining Reflectance, Spectral Unmixing, and Texture Data from High-Resolution Imagery. *Forests* **2020**, *11*, 1234. [CrossRef]
381. Quintano, C.; Fernández-Manso, A.; Roberts, D.A. Enhanced Burn Severity Estimation Using Fine Resolution ET and MESMA Fraction Images with Machine Learning Algorithm. *Remote Sens. Environ.* **2020**, *244*, 111815. [CrossRef]
382. Topouzelis, K.; Papageorgiou, D.; Karagaitanakis, A.; Papakonstantinou, A.; Ballesteros, M.A. Plastic Litter Project 2019: Exploring the Detection of Floating Plastic Litter Using Drones and Sentinel 2 Satellite Images. In Proceedings of the IGARSS 2020—2020 IEEE International Geoscience and Remote Sensing Symposium, Waikoloa, HI, USA, 26 September 2020; pp. 6329–6332.
383. Topouzelis, K.; Papageorgiou, D.; Karagaitanakis, A.; Papakonstantinou, A.; Arias Ballesteros, M. Remote Sensing of Sea Surface Artificial Floating Plastic Targets with Sentinel-2 and Unmanned Aerial Systems (Plastic Litter Project 2019). *Remote Sens.* **2020**, *12*, 2013. [CrossRef]
384. Zhang, Y.; Wu, L.; Ren, H.; Deng, L.; Zhang, P. Retrieval of Water Quality Parameters from Hyperspectral Images Using Hybrid Bayesian Probabilistic Neural Network. *Remote Sens.* **2020**, *12*, 1567. [CrossRef]
385. Salvatore, M.R.; Borges, S.R.; Barrett, J.E.; Sokol, E.R.; Stanish, L.F.; Power, S.N.; Morin, P. Remote Characterization of Photosynthetic Communities in the Fryxell Basin of Taylor Valley, Antarctica. *Antarct. Sci.* **2020**, *32*, 255–270. [CrossRef]
386. Bartholomeus, H.; Kooistra, L.; Stevens, A.; Van Leeuwen, M.; Van Wesemael, B.; Ben-Dor, E.; Tychon, B. Soil Organic Carbon Mapping of Partially Vegetated Agricultural Fields with Imaging Spectroscopy. *Int. J. Appl. Earth Obs. Geoinf.* **2011**, *13*, 81–88. [CrossRef]
387. Ghrefat, H.A.; Goodell, P.C. Land Cover Mapping at Alkali Flat and Lake Lucero, White Sands, New Mexico, USA Using Multi-Temporal and Multi-Spectral Remote Sensing Data. *Int. J. Appl. Earth Obs. Geoinf.* **2011**, *13*, 616–625. [CrossRef]
388. Hosseinjani, M.; Tangestani, M.H. Mapping Alteration Minerals Using Sub-Pixel Unmixing of ASTER Data in the Sarduiyeh Area, SE Kerman, Iran. *Int. J. Digit. Earth* **2011**, *4*, 487–504. [CrossRef]
389. Vicente, L.E.; De Souza Filho, C.R. Identification of Mineral Components in Tropical Soils Using Reflectance Spectroscopy and Advanced Spaceborne Thermal Emission and Reflection Radiometer (ASTER) Data. *Remote Sens. Environ.* **2011**, *115*, 1824–1836. [CrossRef]
390. Hu, X.; Weng, Q. Estimating Impervious Surfaces from Medium Spatial Resolution Imagery: A Comparison between Fuzzy Classification and LSMA. *Int. J. Remote Sens.* **2011**, *32*, 5645–5663. [CrossRef]
391. Weng, Q.; Rajasekar, U.; Hu, X. Modeling Urban Heat Islands and Their Relationship with Impervious Surface and Vegetation Abundance by Using ASTER Images. *IEEE Trans. Geosci. Remote Sens.* **2011**, *49*, 4080–4089. [CrossRef]
392. Castrodad, A.; Xing, Z.; Greer, J.B.; Bosch, E.; Carin, L.; Sapiro, G. Learning Discriminative Sparse Representations for Modeling, Source Separation, and Mapping of Hyperspectral Imagery. *IEEE Trans. Geosci. Remote Sens.* **2011**, *49*, 4263–4281. [CrossRef]
393. Dopido, I.; Zortea, M.; Villa, A.; Plaza, A.; Gamba, P. Unmixing Prior to Supervised Classification of Remotely Sensed Hyperspectral Images. *IEEE Geosci. Remote Sens. Lett.* **2011**, *8*, 760–764. [CrossRef]
394. Halimi, A.; Altmann, Y.; Dobigeon, N.; Tourneret, J.-Y. Nonlinear Unmixing of Hyperspectral Images Using a Generalized Bilinear Model. *IEEE Trans. Geosci. Remote Sens.* **2011**, *49*, 4153–4162. [CrossRef]
395. Heylen, R.; Burazerovic, D.; Scheunders, P. Fully Constrained Least Squares Spectral Unmixing by Simplex Projection. *IEEE Trans. Geosci. Remote Sens.* **2011**, *49*, 4112–4122. [CrossRef]
396. Heylen, R.; Burazerovic, D.; Scheunders, P. Non-Linear Spectral Unmixing by Geodesic Simplex Volume Maximization. *IEEE J. Sel. Top. Signal Process.* **2011**, *5*, 534–542. [CrossRef]
397. Heylen, R.; Scheunders, P. Non-Linear Fully-Constrained Spectral Unmixing. In Proceedings of the 2011 IEEE International Geoscience and Remote Sensing Symposium, Vancouver, BC, Canada, 24–29 July 2011; pp. 1295–1298.

398. Iordache, M.-D.; Bioucas-Dias, J.M.; Plaza, A. Hyperspectral Unmixingwith Sparse Group Lasso. In Proceedings of the 2011 IEEE International Geoscience and Remote Sensing Symposium, Vancouver, BC, Canada, 24–29 July 2011; pp. 3586–3589.
399. Liu, X.; Xia, W.; Wang, B.; Zhang, L. An Approach Based on Constrained Nonnegative Matrix Factorization to Unmix Hyperspectral Data. *IEEE Trans. Geosci. Remote Sens.* **2011**, *49*, 757–772. [CrossRef]
400. Mianji, F.A.; Zhou, S.; Zhang, Y. Hyperspectral Unmixing Using a Novel Conversion Model. In Proceedings of the 2011 IEEE International Geoscience and Remote Sensing Symposium, Vancouver, BC, Canada, 24–29 July 2011; pp. 2527–2530.
401. Swatantran, A.; Dubayah, R.; Roberts, D.; Hofton, M.; Blair, J.B. Mapping Biomass and Stress in the Sierra Nevada Using Lidar and Hyperspectral Data Fusion. *Remote Sens. Environ.* **2011**, *115*, 2917–2930. [CrossRef]
402. Xia, W.; Wang, B.; Zhang, L.; Lu, Q. Simplex Volume Analysis Based on Triangular Factorization: A Framework for Hyperspectral Unmixing. In Proceedings of the 2011 IEEE International Geoscience and Remote Sensing Symposium, Vancouver, BC, Canada, 24–29 July 2011; pp. 1147–1150.
403. Zare, A. Spatial-Spectral Unmixing Using Fuzzy Local Information. In Proceedings of the 2011 IEEE International Geoscience and Remote Sensing Symposium, Vancouver, BC, Canada, 24–29 July 2011; pp. 1139–1142.
404. Altmann, Y.; Dobigeon, N.; Tourneret, J.-Y.; McLaughlin, S. Nonlinear Unmixing of Hyperspectral Images Using Radial Basis Functions and Orthogonal Least Squares. In Proceedings of the 2011 IEEE International Geoscience and Remote Sensing Symposium, Vancouver, BC, Canada, 24–29 July 2011; pp. 1151–1154.
405. Ambikapathi, A.; Chan, T.-H.; Ma, W.-K.; Chi, C.-Y. Chance-Constrained Robust Minimum-Volume Enclosing Simplex Algorithm for Hyperspectral Unmixing. *IEEE Trans. Geosci. Remote Sens.* **2011**, *49*, 4194–4209. [CrossRef]
406. Canham, K.; Schlamm, A.; Ziemann, A.; Basener, B.; Messinger, D. Spatially Adaptive Hyperspectral Unmixing. *IEEE Trans. Geosci. Remote Sens.* **2011**, *49*, 4248–4262. [CrossRef]
407. Eches, O.; Dobigeon, N.; Tourneret, J.-Y. Enhancing Hyperspectral Image Unmixing With Spatial Correlations. *IEEE Trans. Geosci. Remote Sens.* **2011**, *49*, 4239–4247. [CrossRef]
408. Halimi, A.; Altmann, Y.; Dobigeon, N.; Tourneret, J.-Y. Unmixing Hyperspectral Images Using the Generalized Bilinear Model. In Proceedings of the 2011 IEEE International Geoscience and Remote Sensing Symposium, Vancouver, BC, Canada, 24–29 July 2011; pp. 1886–1889.
409. Iordache, M.-D.; Bioucas-Dias, J.M.; Plaza, A. Sparse Unmixing of Hyperspectral Data. *IEEE Trans. Geosci. Remote Sens.* **2011**, *49*, 2014–2039. [CrossRef]
410. Martin, G.; Plaza, A. Region-Based Spatial Preprocessing for Endmember Extraction and Spectral Unmixing. *IEEE Geosci. Remote Sens. Lett.* **2011**, *8*, 745–749. [CrossRef]
411. Martin, G.; Plaza, A.; Zortea, M. Noise-Robust Spatial Preprocessing Prior to Endmember Extraction from Hyperspectral Data. In Proceedings of the 2011 IEEE International Geoscience and Remote Sensing Symposium, Vancouver, BC, Canada, 24–29 July 2011; pp. 1287–1290.
412. Mei, S.; He, M. Minimum Endmember-Wise Distance Constrained Nonnegative Matrix Factorization for Spectral Mixture Analysis of Hyperspectral Images. In Proceedings of the 2011 IEEE International Geoscience and Remote Sensing Symposium, Vancouver, BC, Canada, 24–29 July 2011; pp. 1299–1302.
413. Villa, A.; Chanussot, J.; Benediktsson, J.A.; Jutten, C. Spectral Unmixing for the Classification of Hyperspectral Images at a Finer Spatial Resolution. *IEEE J. Sel. Top. Signal Process.* **2011**, *5*, 521–533. [CrossRef]
414. Xia, W.; Liu, X.; Wang, B.; Zhang, L. Independent Component Analysis for Blind Unmixing of Hyperspectral Imagery with Additional Constraints. *IEEE Trans. Geosci. Remote Sens.* **2011**, *49*, 2165–2179. [CrossRef]
415. Zuyuan Yang; Guoxu Zhou; Shengli Xie; Shuxue Ding; Jun-Mei Yang; Jun Zhang Blind Spectral Unmixing Based on Sparse Nonnegative Matrix Factorization. *IEEE Trans. Image Process.* **2011**, *20*, 1112–1125. [CrossRef]
416. Zhang, B.; Sun, X.; Gao, L.; Yang, L. Endmember Extraction of Hyperspectral Remote Sensing Images Based on the Ant Colony Optimization (ACO) Algorithm. *IEEE Trans. Geosci. Remote Sens.* **2011**, *49*, 2635–2646. [CrossRef]
417. Zhao, Y.; Yang, J.; Zhang, Q.; Song, L.; Cheng, Y.; Pan, Q. Hyperspectral Imagery Super-Resolution by Sparse Representation and Spectral Regularization. *EURASIP J. Adv. Signal Process.* **2011**, *2011*, 87. [CrossRef]
418. Kamal, M.; Phinn, S. Hyperspectral Data for Mangrove Species Mapping: A Comparison of Pixel-Based and Object-Based Approach. *Remote Sens.* **2011**, *3*, 2222–2242. [CrossRef]
419. Zurita-Milla, R.; Gomez-Chova, L.; Guanter, L.; Clevers, J.G.P.W.; Camps-Valls, G. Multitemporal Unmixing of Medium-Spatial-Resolution Satellite Images: A Case Study Using MERIS Images for Land-Cover Mapping. *IEEE Trans. Geosci. Remote Sens.* **2011**, *49*, 4308–4317. [CrossRef]
420. Bouaziz, M.; Matschullat, J.; Gloaguen, R. Improved Remote Sensing Detection of Soil Salinity from a Semi-Arid Climate in Northeast Brazil. *Comptes Rendus Geosci.* **2011**, *343*, 795–803. [CrossRef]
421. Cui, Q.; Shi, J.; Xu, Y. Estimation of Sub-Pixel Water Area on Tibet Plateau Using Multiple Endmembers Spectral Mixture Spectral Analysis from MODIS Data. In Proceedings of the MIPPR 2011: Remote Sensing Image Processing, Geographic Information Systems, and Other Applications, Guilin, China, 20 November 2011; p. 80061T.
422. Knight, J.; Voth, M. Mapping Impervious Cover Using Multi-Temporal MODIS NDVI Data. *IEEE J. Sel. Top. Appl. Earth Obs. Remote Sens.* **2011**, *4*, 303–309. [CrossRef]
423. Lu, D.; Batistella, M.; Moran, E.; Hetrick, S.; Alves, D.; Brondizio, E. Fractional Forest Cover Mapping in the Brazilian Amazon with a Combination of MODIS and TM Images. *Int. J. Remote Sens.* **2011**, *32*, 7131–7149. [CrossRef]

424. Plemmons, R.J. Dimensionality Reduction, Classification, and Spectral Mixture Analysis Using Non-Negative Underapproximation. *Opt. Eng.* **2011**, *50*, 027001. [CrossRef]
425. Qian, Y.; Jia, S.; Zhou, J.; Robles-Kelly, A. Hyperspectral Unmixing via $L_{1/2}$ Sparsity-Constrained Nonnegative Matrix Factorization. *IEEE Trans. Geosci. Remote Sens.* **2011**, *49*, 4282–4297. [CrossRef]
426. Youngentob, K.N.; Roberts, D.A.; Held, A.A.; Dennison, P.E.; Jia, X.; Lindenmayer, D.B. Mapping Two Eucalyptus Subgenera Using Multiple Endmember Spectral Mixture Analysis and Continuum-Removed Imaging Spectrometry Data. *Remote Sens. Environ.* **2011**, *115*, 1115–1128. [CrossRef]
427. De Jong, S.M.; Addink, E.A.; Van Beek, L.P.H.; Duijsings, D. Physical Characterization, Spectral Response and Remotely Sensed Mapping of Mediterranean Soil Surface Crusts. *Catena* **2011**, *86*, 24–35. [CrossRef]
428. Chudnovsky, A.; Kostinski, A.; Herrmann, L.; Koren, I.; Nutesku, G.; Ben-Dor, E. Hyperspectral Spaceborne Imaging of Dust-Laden Flows: Anatomy of Saharan Dust Storm from the Bodélé Depression. *Remote Sens. Environ.* **2011**, *115*, 1013–1024. [CrossRef]
429. Cao, C.; Chen, W.; Li, G.; Jia, H.; Ji, W.; Xu, M.; Gao, M.; Ni, X.; Zhao, J.; Zheng, S.; et al. The Retrieval of Shrub Fractional Cover Based on a Geometric-Optical Model in Combination with Linear Spectral Mixture Analysis. *Can. J. Remote Sens.* **2011**, *37*, 348–358. [CrossRef]
430. Chen, W.; Cao, C.; Zhang, H.; Jia, H.; Ji, W.; Xu, M.; Gao, M.; Ni, X.; Zhao, J.; Zheng, S.; et al. Estimation of Shrub Canopy Cover Based on a Geometric-Optical Model Using HJ-1 Data. In Proceedings of the 2011 IEEE International Geoscience and Remote Sensing Symposium, Vancouver, BC, Canada, 1–5 August 2011; pp. 1922–1925.
431. Griffin, S.; Rogan, J.; Runfola, D.M. Application of Spectral and Environmental Variables to Map the Kissimmee Prairie Ecosystem Using Classification Trees. *GIScience Remote Sens.* **2011**, *48*, 299–323. [CrossRef]
432. Lu, D.; Moran, E.; Hetrick, S. Detection of Impervious Surface Change with Multitemporal Landsat Images in an Urban–Rural Frontier. *ISPRS J. Photogramm. Remote Sens.* **2011**, *66*, 298–306. [CrossRef]
433. Negrón-Juárez, R.I.; Chambers, J.Q.; Marra, D.M.; Ribeiro, G.H.P.M.; Rifai, S.W.; Higuchi, N.; Roberts, D. Detection of Subpixel Treefall Gaps with Landsat Imagery in Central Amazon Forests. *Remote Sens. Environ.* **2011**, *115*, 3322–3328. [CrossRef]
434. Jiao, Q.; Zhang, B.; Liu, L.; Hu, Y. Estimating Fractional Vegetation Cover in the Wenchuan Earthquake Disaster Area Using High-Resolution Airborne Image and Landsat TM Image. In Proceedings of the MIPPR 2011: Remote Sensing Image Processing, Geographic Information Systems, and Other Applications, SPIE, Guilin, China, 20 November 2011; p. 80062G.
435. Lu, D.; Li, G.; Moran, E.; Batistella, M.; Freitas, C.C. Mapping Impervious Surfaces with the Integrated Use of Landsat Thematic Mapper and Radar Data: A Case Study in an Urban–Rural Landscape in the Brazilian Amazon. *ISPRS J. Photogramm. Remote Sens.* **2011**, *66*, 798–808. [CrossRef]
436. Renó, V.F.; Novo, E.M.L.M.; Suemitsu, C.; Rennó, C.D.; Silva, T.S.F. Assessment of Deforestation in the Lower Amazon Floodplain Using Historical Landsat MSS/TM Imagery. *Remote Sens. Environ.* **2011**, *115*, 3446–3456. [CrossRef]
437. Sankey, T.; Glenn, N. Landsat-5 TM and Lidar Fusion for Sub-Pixel Juniper Tree Cover Estimates in a Western Rangeland. *Photogramm. Eng. Remote Sens.* **2011**, *77*, 1241–1248. [CrossRef]
438. Sunderman, S.O.; Weisberg, P.J. Remote Sensing Approaches for Reconstructing Fire Perimeters and Burn Severity Mosaics in Desert Spring Ecosystems. *Remote Sens. Environ.* **2011**, *115*, 2384–2389. [CrossRef]
439. Gilichinsky, M.; Sandström, P.; Reese, H.; Kivinen, S.; Moen, J.; Nilsson, M. Mapping Ground Lichens Using Forest Inventory and Optical Satellite Data. *Int. J. Remote Sens.* **2011**, *32*, 455–472. [CrossRef]
440. QuickBird. Available online: https://earth.esa.int/eogateway/missions/quickbird-2 (accessed on 15 May 2023).
441. Hamada, Y.; Stow, D.A.; Roberts, D.A. Estimating Life-Form Cover Fractions in California Sage Scrub Communities Using Multispectral Remote Sensing. *Remote Sens. Environ.* **2011**, *115*, 3056–3068. [CrossRef]
442. Ji, M.; Feng, J. Subpixel Measurement of Mangrove Canopy Closure via Spectral Mixture Analysis. *Front. Earth Sci.* **2011**, *5*, 130–137. [CrossRef]
443. Yang, C.; Everitt, J.H. Mapping Three Invasive Weeds Using Airborne Hyperspectral Imagery. *Ecol. Inform.* **2010**, *5*, 429–439. [CrossRef]
444. Mücher, C.; Kooistra, L.; Vermeulen, M.; Haest, B.; Spanhove, T.; Delalieux, S.; Borre, J.V.; Schmidt, A. Object Identification and Characterization with Hyperspectral Imagery to Identify Structure and Function of Natura 2000 Habitats. In Proceedings of the Proceedings Third GEOgraphic Object-Based Image Analysis Conference 2010, Ghent, Belgium, 29 June–2 July 2010; p. 5.
445. Hu, X.; Weng, Q. Estimation of Impervious Surfaces of Beijing, China, with Spectral Normalized Images Using Linear Spectral Mixture Analysis and Artificial Neural Network. *Geocarto Int.* **2010**, *25*, 231–253. [CrossRef]
446. Mezned, N.; Abdeljaoued, S.; Boussema, M.R. A Comparative Study for Unmixing Based Landsat ETM+ and ASTER Image Fusion. *Int. J. Appl. Earth Obs. Geoinf.* **2010**, *12*, S131–S137. [CrossRef]
447. Estes, L.D.; Reillo, P.R.; Mwangi, A.G.; Okin, G.S.; Shugart, H.H. Remote Sensing of Structural Complexity Indices for Habitat and Species Distribution Modeling. *Remote Sens. Environ.* **2010**, *114*, 792–804. [CrossRef]
448. Ruescas, A.B.; Sobrino, J.A.; Julien, Y.; Jiménez-Muñoz, J.C.; Sòria, G.; Hidalgo, V.; Atitar, M.; Franch, B.; Cuenca, J.; Mattar, C. Mapping Sub-Pixel Burnt Percentage Using AVHRR Data. Application to the Alcalaten Area in Spain. *Int. J. Remote Sens.* **2010**, *31*, 5315–5330. [CrossRef]
449. Huang, Y.; Zhang, L.; Li, P.; Zhong, Y. High-Resolution Hyper-Spectral Image Classification with Parts-Based Feature and Morphology Profile in Urban Area. *Geo-Spat. Inf. Sci.* **2010**, *13*, 111–122. [CrossRef]

450. Jin, J.; Wang, B.; Zhang, L. A Novel Approach Based on Fisher Discriminant Null Space for Decomposition of Mixed Pixels in Hyperspectral Imagery. *IEEE Geosci. Remote Sens. Lett.* **2010**, *7*, 699–703. [CrossRef]
451. Wen-Fei, L.; Liang, Z.; Bing, Z.; Lian-Ru, G. Null space spectral projection algorithm for hyperspectral image endmember extraction. *J. Infrared Millim. Waves* **2010**, *29*, 307.
452. Luo, W.-F.; Zhong, L.; Zhang, B.; Gao, L.-R. Independent Component Analysis for Spectral Unmixing in Hyperspectral Remote Sensing Image. *Spectrosc. Spectr. Anal.* **2010**, *30*, 1628–1633.
453. Mei, S.; He, M.; Dai, Y. Virtual Dimensionality Estimation by Double Subspace Projection for Hyperspectral Images. In Proceedings of the 2010 Second IITA International Conference on Geoscience and Remote Sensing, Qingdao, China, 28–31 August 2010; Volume 2, pp. 234–237.
454. Mei, S.; He, M.; Wang, Z.; Feng, D. Spatial Purity Based Endmember Extraction for Spectral Mixture Analysis. *IEEE Trans. Geosci. Remote Sens.* **2010**, *48*, 3434–3445. [CrossRef]
455. Villa, A.; Chanussot, J.; Benediktsson, J.A.; Jutten, C. Supervised Super-Resolution to Improve the Resolution of Hyperspectral Images Classification Maps. In Proceedings of the Image and Signal Processing for Remote Sensing XVI, SPIE, Toulouse, France, 20–22 September 2010; Volume 7830, pp. 168–175.
456. Golubiewski, N.E.; Wessman, C.A. Discriminating Urban Vegetation from a Metropolitan Matrix through Partial Unmixing with Hyperspectral AVIRIS Data. *Can. J. Remote Sens.* **2010**, *36*, 261–275. [CrossRef]
457. Eches, O.; Dobigeon, N.; Tourneret, J.-Y. Estimating the Number of Endmembers in Hyperspectral Images Using the Normal Compositional Model and a Hierarchical Bayesian Algorithm. *IEEE J. Sel. Top. Signal Process.* **2010**, *4*, 582–591. [CrossRef]
458. Chang, C.-I.; Xiong, W.; Liu, W.; Chang, M.-L.; Wu, C.-C.; Chen, C.C.-C. Linear Spectral Mixture Analysis Based Approaches to Estimation of Virtual Dimensionality in Hyperspectral Imagery. *IEEE Trans. Geosci. Remote Sens.* **2010**, 5595092. [CrossRef]
459. Huck, A.; Guillaume, M.; Blanc-Talon, J. Minimum Dispersion Constrained Nonnegative Matrix Factorization to Unmix Hyperspectral Data. *IEEE Trans. Geosci. Remote Sens.* **2010**, *48*, 2590–2602. [CrossRef]
460. Iordache, M.-D.; Plaza, A.; Bioucas-Dias, J. Recent Developments in Sparse Hyperspectral Unmixing. In Proceedings of the 2010 IEEE International Geoscience and Remote Sensing Symposium, Honolulu, HI, USA, 25–30 July 2010; pp. 1281–1284.
461. Martin, G.; Ruiz, V.G.; Plaza, A.J.; Ortiz, J.P.; Fernández, I.G. Impact of JPEG2000 Compression on Endmember Extraction and Unmixing of Remotely Sensed Hyperspectral Data. *J. Appl. Remote Sens.* **2010**, *4*, 041796.
462. Martin, G.; Plaza, A. Spatial Preprocessing for Endmember Extraction Using Unsupervised Clustering and Orthogonal Subspace Projection Concepts. In Proceedings of the 2010 IEEE International Geoscience and Remote Sensing Symposium, Honolulu, HI, USA, 25–30 July 2010; pp. 959–962.
463. Raksuntorn, N.; Du, Q. Nonlinear Spectral Mixture Analysis for Hyperspectral Imagery in an Unknown Environment. *IEEE Geosci. Remote Sens. Lett.* **2010**, *7*, 836–840. [CrossRef]
464. Hendrix, E.M.T.; Garcia, I.; Plaza, J.; Plaza, A. Minimum Volume Simplicial Enclosure for Spectral Unmixing of Remotely Sensed Hyperspectral Data. In Proceedings of the 2010 IEEE International Geoscience and Remote Sensing Symposium, Honolulu, HI, USA, 25–30 July 2010; pp. 193–196.
465. Plaza, J.; Plaza, A. Spectral Mixture Analysis of Hyperspectral Scenes Using Intelligently Selected Training Samples. *IEEE Geosci. Remote Sens. Lett.* **2010**, *7*, 371–375. [CrossRef]
466. Barnsley, M.J.; Settle, J.J.; Cutter, M.A.; Lobb, D.R.; Teston, F. The PROBA/CHRIS Mission: A Low-Cost Smallsat for Hyperspectral Multiangle Observations of the Earth Surface and Atmosphere. *IEEE Trans. Geosci. Remote Sens.* **2004**, *42*, 1512–1520. [CrossRef]
467. Verrelst, J.; Clevers, J.G.P.W.; Schaepman, M.E. Merging the Minnaert-k Parameter with Spectral Unmixing to Map Forest Heterogeneity With CHRIS/PROBA Data. *IEEE Trans. Geosci. Remote Sens.* **2010**, 5466035. [CrossRef]
468. Matabishi, J.G.; Braun, A.; Warth, G. Multiple endmember spectral mixture analysis of desis image to identify rooftops in kigali. *Int. Arch. Photogramm. Remote Sens. Spat. Inf. Sci.* **2022**, *XLVI-1/W1-2021*, 39–47. [CrossRef]
469. Paul, A.; Dutta, D.; Jha, C.S. Target detection using dlr earth sensing imaging spectrometer (desis) data. *Int. Arch. Photogramm. Remote Sens. Spat. Inf. Sci.* **2022**, *XLVI-1/W1-2021*, 57–64. [CrossRef]
470. Xiong, W.; Chang, C.-I.; Tsai, C.-T. Estimation of Virtual Dimensionality in Hyperspectral Imagery by Linear Spectral Mixture Analysis. In Proceedings of the 2010 IEEE International Geoscience and Remote Sensing Symposium, Honolulu, HI, USA, 25–30 July 2010; pp. 979–982.
471. Castrodad, A.; Xing, Z.; Greer, J.; Bosch, E.; Carin, L.; Sapiro, G. Discriminative Sparse Representations in Hyperspectral Imagery. In Proceedings of the 2010 IEEE International Conference on Image Processing, Hong Kong, 26–29 September 2010; pp. 1313–1316.
472. Somers, B.; Verbesselt, J.; Ampe, E.M.; Sims, N.; Verstraeten, W.W.; Coppin, P. Spectral Mixture Analysis to Monitor Defoliation in Mixed-Aged Eucalyptus Globulus Labill Plantations in Southern Australia Using Landsat 5-TM and EO-1 Hyperion Data. *Int. J. Appl. Earth Obs. Geoinf.* **2010**, *12*, 270–277. [CrossRef]
473. Elatawneh, A.; Manakos, I.; Kalaitzidis, C.; Schneider, T. Land-Cover Classification and Unmixing of Hyperion Image in Area of Anopoli. In *Imagin [e, g] Europe*; IOS Press: Amsterdam, The Netherlands, 2010; pp. 111–121.
474. Cavalli, R.M. Comparison of Split Window Algorithms for Retrieving Measurements of Sea Surface Temperature from MODIS Data in Near-Land Coastal Waters. *ISPRS Int. J. Geo-Inf.* **2018**, *7*, 30. [CrossRef]
475. Chen, W.; Cao, C.; He, Q.; Guo, H.; Zhang, H.; Li, R.; Zheng, S.; Xu, M.; Gao, M.; Zhao, J.; et al. Quantitative Estimation of the Shrub Canopy LAI from Atmosphere-Corrected HJ-1 CCD Data in Mu Us Sandland. *Sci. China Earth Sci.* **2010**, *53*, 26–33. [CrossRef]

476. Meng, D.; Gong, H.; Li, X.; Zhao, W.; Li, Y. Impervious Surface Coverage and Their Impact on Other Components of the Urban Ecosystem in Beijing. In Proceedings of the 2010 IEEE International Geoscience and Remote Sensing Symposium, Honolulu, HI, USA, 20–24 July 2010; pp. 2731–2734.
477. Biggs, T.W.; Atkinson, E.; Powell, R.; Ojeda-Revah, L. Land Cover Following Rapid Urbanization on the US–Mexico Border: Implications for Conceptual Models of Urban Watershed Processes. *Landsc. Urban Plan.* **2010**, *96*, 78–87. [CrossRef]
478. Bohlman, S.A. Landscape Patterns and Environmental Controls of Deciduousness in Forests of Central Panama: Patterns/Controls of Tropical Deciduousness. *Glob. Ecol. Biogeogr.* **2010**, *19*, 376–385. [CrossRef]
479. Huang, C.; Asner, G.P.; Barger, N.N.; Neff, J.C.; Floyd, M.L. Regional Aboveground Live Carbon Losses Due to Drought-Induced Tree Dieback in Piñon–Juniper Ecosystems. *Remote Sens. Environ.* **2010**, *114*, 1471–1479. [CrossRef]
480. Pacheco, A.; McNairn, H. Evaluating Multispectral Remote Sensing and Spectral Unmixing Analysis for Crop Residue Mapping. *Remote Sens. Environ.* **2010**, *114*, 2219–2228. [CrossRef]
481. Solans Vila, J.P.; Barbosa, P. Post-Fire Vegetation Regrowth Detection in the Deiva Marina Region (Liguria-Italy) Using Landsat TM and ETM+ Data. *Ecol. Model.* **2010**, *221*, 75–84. [CrossRef]
482. Li, C.; Du, J.; Su, Y.; Li, Q.; Chen, L. Extraction of Impervious Surface Based on Multi-Source Satellite Data of Qinhuai River Basin from 1979–2009. In Proceedings of the 2010 18th International Conference on Geoinformatics, Beijing, China, 18–20 June 2010; pp. 1–6.
483. Powell, R.L.; Roberts, D.A. Characterizing Urban Land-Cover Change in Rondônia, Brazil: 1985 to 2000. *J. Lat. Am. Geogr.* **2010**, *9*, 183–211. [CrossRef]
484. Elmore, A.J.; Guinn, S.M. Synergistic Use of Landsat Multispectral Scanner with GIRAS Land-Cover Data to Retrieve Impervious Surface Area for the Potomac River Basin in 1975. *Remote Sens. Environ.* **2010**, *114*, 2384–2391. [CrossRef]
485. He, M.; Zhao, B.; Ouyang, Z.; Yan, Y.; Li, B. Linear Spectral Mixture Analysis of Landsat TM Data for Monitoring Invasive Exotic Plants in Estuarine Wetlands. *Int. J. Remote Sens.* **2010**, *31*, 4319–4333. [CrossRef]
486. Liu, Y.; Yue, W. Estimation of Urban Vegetation Fraction by Image Fusion and Spectral Unmixing. *Acta Ecol. Sin.* **2010**, *30*, 93–99.
487. Tømmervik, H.; Dunfjeld, S.; Olsson, G.A.; Nilsen, M.Ø. Detection of Ancient Reindeer Pens, Cultural Remains and Anthropogenic Influenced Vegetation in Byrkije (Børgefjell) Mountains, Fennoscandia. *Landsc. Urban Plan.* **2010**, *98*, 56–71. [CrossRef]
488. Yang, F.; Matsushita, B.; Fukushima, T. A Pre-Screened and Normalized Multiple Endmember Spectral Mixture Analysis for Mapping Impervious Surface Area in Lake Kasumigaura Basin, Japan. *ISPRS J. Photogramm. Remote Sens.* **2010**, *65*, 479–490. [CrossRef]
489. Borfecchia, F.; De Cecco, L.; Pollino, M.; La Porta, L.; Lugari, A.; Martini, S.; Ristoratore, E.; Pascale, C. Active and Passive Remote Sensing for Supporting the Evaluation of the Urban Seismic Vulnerability. *Ital. J. Remote Sens.* **2010**, *42*, 129–141. [CrossRef]
490. Silván-Cárdenas, J.L.; Wang, L. Retrieval of Subpixel Tamarix Canopy Cover from Landsat Data along the Forgotten River Using Linear and Nonlinear Spectral Mixture Models. *Remote Sens. Environ.* **2010**, *114*, 1777–1790. [CrossRef]
491. Liu, X.; Li, X.; Zhang, X. Determining Class Proportions within a Pixel Using a New Mixed-Label Analysis Method. *IEEE Trans. Geosci. Remote Sens.* **2009**, *48*, 1882–1891.
492. Gilichinskya, M.; Sandströma, P.; Reesea, H.; Kivinenb, S.; Moenb, J.; Nilsona, M. *Application of National Forest Inventory for Remote Sensing Classification of Ground Lichen in Nothern Sweden*; International Archives of the Photogrammetry, Remote Sensing and Spatial Information Sciences-ISPRS Archives: Haifa, Israel, 2010; pp. 146–152.
493. Sarapirome, S.; Kulrat, C. Comparison on urban classifications using landsattm and linear spectral mixture analysis extracted images: Nakhon Ratchasima municipal area, Thailand. *Suranaree J. Sci. Technol.* **2010**, *17*, 401–411.
494. Cavalli, R.M.; Pascucci, S.; Pignatti, S. Optimal Spectral Domain Selection for Maximizing Archaeological Signatures: Italy Case Studies. *Sensors* **2009**, *9*, 1754–1767. [CrossRef] [PubMed]
495. Alves Aguiar, D.; Adami, M.; Fernando Silva, W.; Friedrich Theodor Rudorff, B.; Pupin Mello, M.; dos Santos Vila da Silva, J. Modis Time Series to Assess Pasture Land. In Proceedings of the 2010 IEEE International Geoscience and Remote Sensing Symposium, Honolulu, HI, USA, 20–24 July 2010; pp. 2123–2126.
496. Eckmann, T.C.; Still, C.J.; Roberts, D.A.; Michaelsen, J.C. Variations in Subpixel Fire Properties with Season and Land Cover in Southern Africa. *Earth Interact.* **2010**, *14*, 1–29. [CrossRef]
497. Meusburger, K.; Bänninger, D.; Alewell, C. Estimating Vegetation Parameter for Soil Erosion Assessment in an Alpine Catchment by Means of QuickBird Imagery. *Int. J. Appl. Earth Obs. Geoinf.* **2010**, *12*, 201–207. [CrossRef]
498. Meusburger, K.; Konz, N.; Schaub, M.; Alewell, C. Soil Erosion Modelled with USLE and PESERA Using QuickBird Derived Vegetation Parameters in an Alpine Catchment. *Int. J. Appl. Earth Obs. Geoinf.* **2010**, *12*, 208–215. [CrossRef]
499. Schmidt, M. Monitoring Aquatic Weeds in a River System Using SPOT 5 Satellite Imagery. *J. Appl. Remote Sens* **2010**, *4*, 043528. [CrossRef]
500. Soenen, S.A.; Peddle, D.R.; Hall, R.J.; Coburn, C.A.; Hall, F.G. Estimating Aboveground Forest Biomass from Canopy Reflectance Model Inversion in Mountainous Terrain. *Remote Sens. Environ.* **2010**, *114*, 1325–1337. [CrossRef]
501. Ustin, S.L.; Hart, Q.J.; Duan, L.; Scheer, G. Vegetation Mapping on Hardwood Rangelands in California. *Int. J. Remote Sens.* **1996**, *17*, 3015–3036. [CrossRef]
502. Hunt, E.R., Jr.; Barlow, M.M.; Mahelona, C.L.; Laycock, W.A.; Heising, S.J.; Smith, R.P.; Foreman, J. Progress of the Wyoming Hyperspectral Imagery Pilot Project: Analysis of AVIRIS Data for Rangeland Assessment. In *Hyperspectral Remote Sensing and Applications*; Shen, S.S., Ed.; SPIE: Denver, CO, USA, 1996; pp. 291–297.

503. Bowers, T.L.; Rowan, L.C. Remote Mineralogic and Lithologic Mapping of the Ice River Alkaline Complex, British Columbia, Canada, Using AVIRIS Data. *Photogramm. Eng. Remote Sens.* **1996**, *62*, 1379–1386.
504. Meer, F.V.D. Metamorphic Facies Zonation in the Ronda Peridotites: Spectroscopic Results from Field and GER Imaging Spectrometer Data. *Int. J. Remote Sens.* **1996**, *17*, 1633–1657. [CrossRef]
505. Rosenthal, W. Estimating Alpine Snow Cover with Unsupervised Spectral Unmixing. In Proceedings of the IGARSS'96. 1996 International Geoscience and Remote Sensing Symposium, Lincoln, NE, USA, 31 May 1996; Volume 4, pp. 2252–2254.
506. Van Der Meer, F. Spectral Mixture Modelling and Spectral Stratigraphy in Carbonate Lithofacies Mapping. *ISPRS J. Photogramm. Remote Sens.* **1996**, *51*, 150–162. [CrossRef]
507. Ben-Dor, E.; Kruse, F.A.; Dietz, J.B.; Braun, A.W.; Banin, A. Spatial Distortion and Quantitative Geological Mapping of Makhtesh Ramon, NEGEV, ISRAEL, by Using the GER 63 Channel Scanner Data. *Can. J. Remote Sens.* **1996**, *22*, 258–268. [CrossRef]
508. Kerdiles, H.; Grondona, M.O. NOAA-AVHRR NDVI Decomposition and Subpixel Classification Using Linear Mixing in the Argentinean Pampa. *Int. J. Remote Sens.* **1995**, *16*, 1303–1325. [CrossRef]
509. Dwyer, J.L.; Kruse, F.A.; Lefkoff, A.B. Effects of Empirical versus Model-Based Reflectance Calibration on Automated Analysis of Imaging Spectrometer Data: A Case Study from the Drum Mountains, Utah. *Photogramm. Eng. Remote Sens.* **1995**, *61*, 1247–1254.
510. Lacaze, B.; Hill, J.; Mehl, W. Evaluation of Green Vegetation Fractional Cover in Mediterranean Ecosystems from Spectral Unmixing of Landsat TM and AVIRIS Data. In *Multispectral and Microwave Sensing of Forestry, Hydrology, and Natural Resources*; Mougin, E., Ranson, K.J., Smith, J.A., Eds.; SPIE: Rome, Italy, 1995; pp. 339–346.
511. Rowan, L.C.; Bowers, T.L.; Crowley, J.K.; Anton-Pacheco, C.; Gumiel, P.; Kingston, M.J. Analysis of Airborne Visible-Infrared Imaging Spectrometer (AVIRIS) Data of the Iron Hill, Colorado, Carbonatite-Alkalic Igneous Complex. *Econ. Geol.* **1995**, *90*, 1966–1982. [CrossRef]
512. Lavreau, J. Models of Spectral Unmixing: Simplex versus Least Squares Method of Resolution. In Proceedings of the Multispectral and Microwave Sensing of Forestry, Hydrology, and Natural Resources, SPIE, Rome, Italy, 30 September 1995; Volume 2314, pp. 397–407.
513. Van Der Meer, F. Spectral Unmixing of Landsat Thematic Mapper Data. *Int. J. Remote Sens.* **1995**, *16*, 3189–3194. [CrossRef]
514. Bianchi, R.; Cavalli, R.M.; Marino, C.M.; Pignatti, S.; Poscolieri, M. Use of Airborne Hyperspectral Images to Assess the Spatial Distribution of Oil Spilled during the Trecate Blow-out (Northern Italy). In Proceedings of the Remote Sensing for Agriculture, Forestry, and Natural Resources; International Society for Optics and Photonics, Paris, France, 26–28 September 1995; Volume 2585, pp. 352–362.
515. Hall, F.G.; Peddle, D.R.; LeDrew, E.F. Remote Sensing of Biophysical Variables in Boreal Stands of Picea Mariana. In Proceedings of the 1995 International Geoscience and Remote Sensing Symposium, IGARSS'95—Quantitative Remote Sensing for Science and Applications, Firenze, Italy, 10–14 July 1995; Volume 2, pp. 976–977.
516. Cracknell, A.P. Review Article Synergy in Remote Sensing-What's in a Pixel? *Int. J. Remote Sens.* **1998**, *19*, 2025–2047. [CrossRef]
517. Shahid, K.T.; Schizas, I.D. Spatial-Aware Hyperspectral Nonlinear Unmixing Autoencoder with Endmember Number Estimation. *IEEE J. Sel. Top. Appl. Earth Obs. Remote Sens.* **2022**, *15*, 20–41. [CrossRef]
518. Foody, G.M. Status of Land Cover Classification Accuracy Assessment. *Remote Sens. Environ.* **2002**, *80*, 185–201. [CrossRef]
519. Stehman, S.V.; Foody, G.M. Key Issues in Rigorous Accuracy Assessment of Land Cover Products. *Remote Sens. Environ.* **2019**, *231*, 111199. [CrossRef]
520. Milella, M. *Saperi Della Cultura e Agire Formativo*; Morlacchi Editore: Perugia, Italy, 2003.
521. Congalton, R.G.; Green, K. *Assessing the Accuracy of Remotely Sensed Data: Principles and Practices*; CRC Press: Boca Raton, FL, USA, 2019.
522. Cavalli, R. Retrieval of Sea Surface Temperature from MODIS Data in Coastal Waters. *Sustainability* **2017**, *9*, 2032. [CrossRef]
523. Gupta, H.V.; Kling, H.; Yilmaz, K.K.; Martinez, G.F. Decomposition of the Mean Squared Error and NSE Performance Criteria: Implications for Improving Hydrological Modelling. *J. Hydrol.* **2009**, *377*, 80–91. [CrossRef]
524. Cavalli, R.; Betti, M.; Campanelli, A.; Cicco, A.; Guglietta, D.; Penna, P.; Piermattei, V. A Methodology to Assess the Accuracy with Which Remote Data Characterize a Specific Surface, as a Function of Full Width at Half Maximum (FWHM): Application to Three Italian Coastal Waters. *Sensors* **2014**, *14*, 1155–1183. [CrossRef] [PubMed]
525. Bradley, A.P. The Use of the Area under the ROC Curve in the Evaluation of Machine Learning Algorithms. *Pattern Recognit.* **1997**, *30*, 1145–1159. [CrossRef]
526. Cavalli, R.M.; Colosi, F.; Palombo, A.; Pignatti, S.; Poscolieri, M. Remote Hyperspectral Imagery as a Support to Archaeological Prospection. *J. Cult. Herit.* **2007**, *8*, 272–283. [CrossRef]
527. Jia, S.; Qian, Y. Spectral and Spatial Complexity-Based Hyperspectral Unmixing. *IEEE Trans. Geosci. Remote Sens.* **2007**, *45*, 3867–3879.
528. Comber, A.; Fisher, P.; Brunsdon, C.; Khmag, A. Spatial Analysis of Remote Sensing Image Classification Accuracy. *Remote Sens. Environ.* **2012**, *127*, 237–246. [CrossRef]
529. Roberts, D.A.; Gardner, M.; Church, R.; Ustin, S.; Scheer, G.; Green, R.O. Mapping Chaparral in the Santa Monica Mountains Using Multiple Endmember Spectral Mixture Models. *Remote Sens. Environ.* **1998**, *65*, 267–279. [CrossRef]
530. Morales-Barquero, L.; Lyons, M.B.; Phinn, S.R.; Roelfsema, C.M. Trends in Remote Sensing Accuracy Assessment Approaches in the Context of Natural Resources. *Remote Sens.* **2019**, *11*, 2305. [CrossRef]

531. Cerra, D.; Agapiou, A.; Cavalli, R.; Sarris, A. An Objective Assessment of Hyperspectral Indicators for the Detection of Buried Archaeological Relics. *Remote Sens.* **2018**, *10*, 500. [CrossRef]
532. AVIRIS—JPL-NASA. Available online: https://aviris.jpl.nasa.gov/data/free_data.html (accessed on 31 January 2023).
533. Grupo de Inteligencia Computacional. Available online: https://www.ehu.eus/ccwintco/index.php/Hyperspectral_Remote_Sensing_Scenes (accessed on 31 January 2023).
534. MultiSpec. Available online: https://engineering.purdue.edu/~biehl/MultiSpec/hyperspectral.html (accessed on 31 January 2023).
535. Remote Sensing Laboratory. Available online: https://rslab.ut.ac.ir/data (accessed on 31 January 2023).
536. Cuprite Reference Map. Available online: https://www.usgs.gov/media/images/aviris-scene-flown-over-cuprite-nevada (accessed on 20 May 2023).
537. Cavalli, R.M. Capability of Remote Sensing Images to Distinguish the Urban Surface Materials: A Case Study of Venice City. *Remote Sens.* **2021**, *13*, 3959. [CrossRef]
538. Justice, C.; Belward, A.; Morisette, J.; Lewis, P.; Privette, J.; Baret, F. Developments in the'validation'of Satellite Sensor Products for the Study of the Land Surface. *Int. J. Remote Sens.* **2000**, *21*, 3383–3390. [CrossRef]
539. Congalton, R.G.; Gu, J.; Yadav, K.; Thenkabail, P.; Ozdogan, M. Global Land Cover Mapping: A Review and Uncertainty Analysis. *Remote Sens.* **2014**, *6*, 12070–12093. [CrossRef]
540. Baret, F.; Weiss, M.; Allard, D.; Garrigue, S.; Leroy, M.; Jeanjean, H.; Fernandes, R.; Myneni, R.; Privette, J.; Morisette, J.; et al. VALERI: A Network of Sites and a Methodology for the Validation of Medium Spatial Resolution Land Satellite Products; 2021; hal-03221068. Available online: https://hal.inrae.fr/hal-03221068 (accessed on 10 May 2023).
541. PRODES. Available online: http://www.obt.inpe.br/OBT/assuntos/programas/amazonia/prodes (accessed on 22 March 2023).
542. Toutin, T. Review Article: Geometric Processing of Remote Sensing Images: Models, Algorithms and Methods. *Int. J. Remote Sens.* **2004**, *25*, 1893–1924. [CrossRef]
543. Cheng, X.; Wang, Y.; Jia, J.; Wen, M.; Shu, R.; Wang, J. The Effects of Misregistration between Hyperspectral and Panchromatic Images on Linear Spectral Unmixing. *Int. J. Remote Sens.* **2020**, *41*, 8862–8889. [CrossRef]
544. Strahler, A.H.; Boschetti, L.; Foody, G.M.; Friedl, M.A.; Hansen, M.C.; Herold, M.; Mayaux, P.; Morisette, J.T.; Stehman, S.V.; Woodcock, C.E. Global Land Cover Validation: Recommendations for Evaluation and Accuracy Assessment of Global Land Cover Maps. *Eur. Communities Luxemb.* **2006**, *51*, 1–60.
545. Gharbi, W.; Chaari, L.; Benazza-Benyahia, A. Joint Bayesian Hyperspectral Unmixing for Change Detection. In Proceedings of the 2020 Mediterranean and Middle-East Geoscience and Remote Sensing Symposium (M2GARSS), Tunis, Tunisia, 9–11 March 2020; pp. 37–40.
546. Park, J.-J.; Oh, S.; Park, K.-A.; Kim, T.-S.; Lee, M. Applying Hyperspectral Remote Sensing Methods to Ship Detection Based on Airborne and Ground Experiments. *Int. J. Remote Sens.* **2020**, *41*, 5928–5952. [CrossRef]